UPC
UNIVERSITAT POLITÈCNICA
DE CATALUNYA

E.T.S.E.I.B.

Departament
d'Enginyeria
Química

SIMULACIÓN DE ESTRUCTURAS Y PROPIEDADES DE POLIAMIDAS HELICOIDALES

Memoria presentada por David Zanuy Gómara para optar al grado de Doctor en Ciencias Químicas.

Trabajo realizado en el Departament D'Enginyeria Química de la UPC, bajo la dirección del Dr. Carlos Alemán Llansó.

Barcelona, Marzo de 2001

VII.5. "On the structure of phase A of comblike poly(α-alkyl-β-L-aspartate)s: a molecular modelling study"

Zanuy, D.; Namba, A.; León S.; Alemán C.; Muñoz-Guerra, S. *Polymer* **2001**, *42*, 281-287

ELSEVIER

Polymer 42 (2001) 281–287

polymer

www.elsevier.nl/locate/polymer

On the structure of the phase A of comb-like poly(α-alkyl-β,L-aspartate)s: a molecular modelling study

D. Zanuy, A.M. Namba[1], S. León, C. Alemán*, S. Muñoz-Guerra

Departament d'Enginyeria Química, E.T.S. d'Enginyers Industrials de Barcelona, Universitat Politècnica de Catalunya, Diagonal 647, Barcelona E-08028, Spain

Received 14 January 2000; received in revised form 29 February 2000; accepted 12 April 2000

Abstract

The phase A of the comb-like poly(α-*n*-octadecyl-β,L-aspartate) has been investigated using atomistically detailed computer simulations. Four independent polymer chains of 13 residues were constructed and packed in an orthogonal simulation box with periodic continuation conditions. A set of microstructures was obtained by Configurational Bias Monte Carlo generation. Some torsional angles of the alkyl side chains were constrained in order to facilitate the crystallization of paraffinic chains. The resulting microstructures have provided a detailed description of the structural behaviour of this phase allowing to characterize some related properties. The most relevant results have been compared with those recently obtained for the phase B and with the available experimental data.

Keywords: Poly(α-alkyl-β,L-aspartate); Molecular modelling; Comb-like polymers

1. Introduction

Some years ago a great effort was devoted to study comb-like poly(γ-alkyl-α,L-glutamate)s, [1–5] i.e. poly(α,L-glutamate)s bearing long alkyl side chains, abbreviated PALG-*n*, *n* being the number of carbon atoms contained in the alkyl group. These polypeptides form biphasic structures when the alkyl side chain is long enough, [2] i.e. $n > 10$. In these structures, the polypeptide α-helix main chains are arranged in layers with side chains crystallized in a separated phase, which is located between the layers. They present two transition temperatures T_1 and T_2 ($T_1 < T_2$) which correspond to the melting of the side chains and to the interconversion between two liquid-crystal-like structures, respectively [1,2,5].

More recently, a new family of comb-like polypeptides constituted by β-amino acids has emerged [6–9]. These are the poly(α-alkyl-β,L-aspartate)s, abbreviated PAALA-*n*, which can be considered as stereoregular nylon 3 derivatives bearing an alkoxy-carbonyl group attached to the backbone β-carbon of the repeating unit.

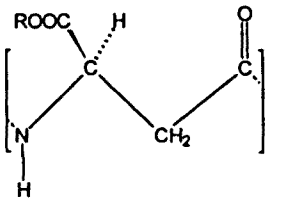

Compounds with $n = 12$, 14, 16, 18 and 22 were synthesized and their structure in the solid state examined by i.r. dichroism, NMR and X-ray diffraction [6,7]. All of them adopt a 13/4 helical conformation stabilized by intramolecular hydrogen bonds, which is the conformation usually observed for the poly(β,L-aspartate)s bearing short alkyl side chains [10,11]. These comb-like PAALA-*n* present biphasic structures similar to those previously described for PALG-*n* with $n > 10$. Thus, three different phases, namely A, B and C (Fig. 1), can be observed for these compounds upon increasing temperature, the 13/4 helical conformation being retained through the whole sequence of transitions.

At temperatures below T_1 a smectic-like phase, denoted phase A, is observed. This is conceived as a structure with the helices aligned in layers separated by the crystallized side-chains [6]. X-ray and electron diffraction, and DSC

* Corresponding author. Tel.: +34-93401-6680/6681; fax: +34-93401-6600/7150.

E-mail address: aleman@eq.upc.es (C. Alemán).

[1] Present Address: Departamento de Química da Faculdade de Filosofia, Ciências e Letras de Ribeirão Preto, Universidade de São Paulo, Avenida Bandeirantes No. 3900, 14049-901, Ribeirão Preto, SP, Brazil.

0032-3861/01/$ - see front matter
PII: S0032-3861(00)00313-X

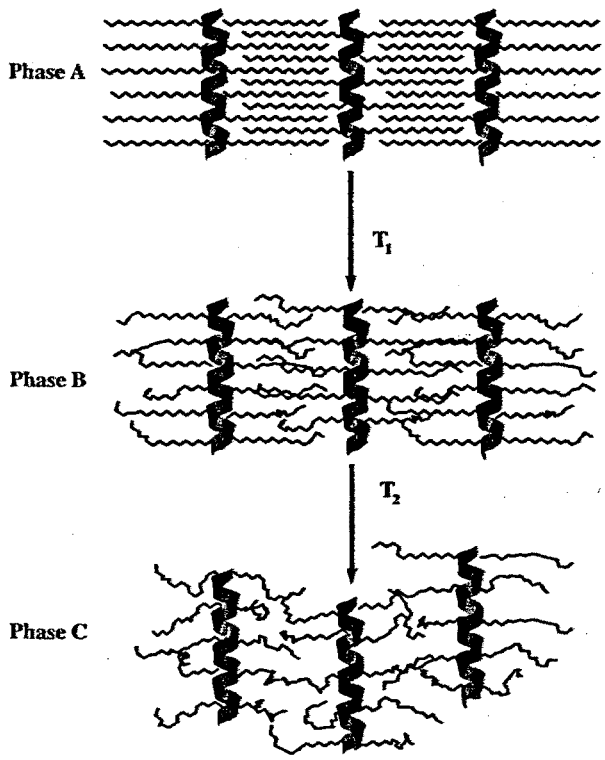

Fig. 1. Schematic model illustrating the structural changes that take place in PAALA-*n* with $n \geq 12$ by the effect of temperature.

measurements indicate a hexagonal arrangement of the side chains similar to the hexagonal crystal phase exhibited by *n*-alkanes at temperatures near their melting points [12]. It should be emphasized that this situation differs from that observed in PALG-*n* with $n > 10$, in which the side chains crystal lattices resemble the triclinic unit cell displayed by low molecular weight *n*-alkanes or polyethylene [2]. The phase B of PAALA-*n* with $n \geq 12$ is obtained upon heating above T_1 and converts into phase C upon heating above T_2. In phase B, the helices retain the layered arrangement but the alkyl side chains are in a disordered state due to the melting of the paraffin crystallites [6,7]. Finally, phase C has been interpreted to consist of an uniaxial arrangement of independent helices embedded in a matrix made up of side chains in a nearly coiled state.

The phase B of PAALA-*n* with *n* ranging from 12 to 18 was recently investigated using Monte Carlo (MC) simulations of an atomistically explicit model [9]. The results provided a detailed description of the structural behaviour of the poly(β-L-aspartate)s in this cholesteric phase. Furthermore, the ability of phase B of PAALA-*n* to mimic barrier synthetic composites and biological structures related with the permeation processes was also investigated by studying both the distribution of the unoccupied space and the solubility of small gaseous penetrants [7]. Whereas the phase B has been characterized in detail, the structure of phase A has not been examined at the atomistic level. This is a serious shortcoming since a detailed understanding of the structure is a crucial point to have a complete view of the transition that takes place when phase A changes to phase B [6].

In this work, we present a molecular modelling study on the phase A of PAALA-*n* with $n \geq 12$ using MC simulations. Thus, the goal of this work is to describe the most important structural properties of the phase A and to compare them with those of the phase B. We have concentrated our efforts on PAALA-18 which is the most representative member of the comb-like PAALA-*n* series and that has been studied in detail by experimental methods.

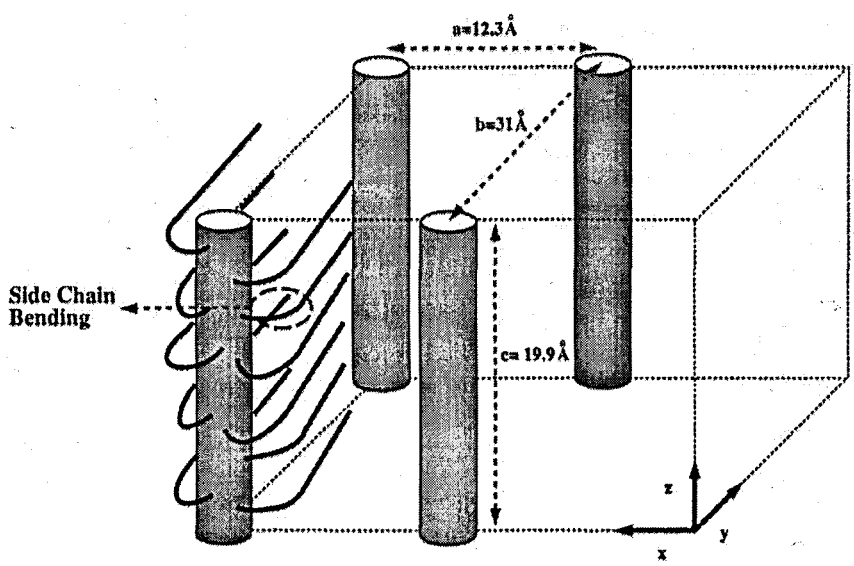

Fig. 2. Schematic representation of the simulated model. The lattice dimensions are indicated and only the four parent helices are represented.

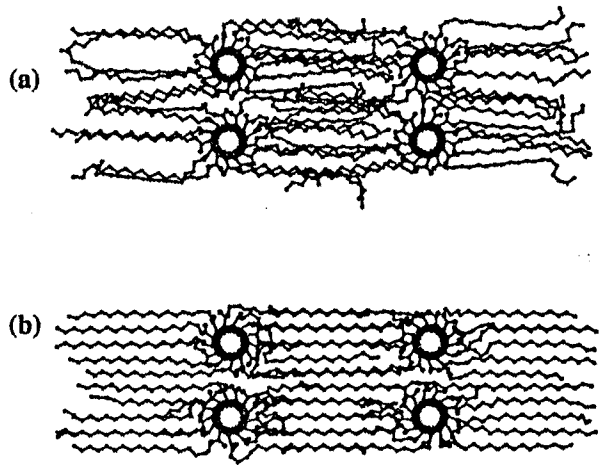

Fig. 3. Representative structure of the PAALA-18 obtained after NVT equilibration considering: (a) all the dihedral angles of the alkyl side chains as degrees of freedom; and (b) three central torsional angles of the alkyl side chains fixed at *trans* conformation and the remainders left free.

2. Methods

2.1. Construction of the simulated model.

The starting geometry for the layered structure of PAALA-18 was built using the available experimental information [6]. The helical conformation used for the polymer under study was generated using the conformational parameters obtained for other poly(α-alkyl-β,L-aspartate)s bearing small alkyl side chains [10,11]. The conformation is a right-handed 13/4 helix with 3.25 residues per turn and an axial repeat length of c_o = 19.9 Å. The torsional angles of the helix backbone were kept constant at the values reported in Ref. [10]. Four independent helices were packed in an orthogonal simulation box with the helix axes oriented parallel to the *z*-axis (Fig. 2). Helices were arranged antiparallel with respect to each other as was previously observed for PAALA-*n* with $n \leq 8$ [8,10,11]. The torsional angles associated to the methylene units of the alkyl side chains were initially considered in *trans* conformation with the exception of those located between two helices within a layer, i.e. the torsional angles involved in the side chain bending (Fig. 2), which were taken from our previous simulations for the phase B of PAALA-18 [7,9].

The distance between the helices within a layer, i.e. the box edge *a* along the *x*-axis, was fixed at 12.3 Å, which is the value determined from X-ray diffraction [6], and was kept constant along the simulations. The distance between the layers, i.e. the box edge *b* along the *y*-axis, was initially fixed at 36 Å and was progressively reduced to 31 Å (see below), which is the observed value. Therefore, the degrees of freedom in the simulations were the torsional angles of the alkyl side groups and the setting angle of each chain, i.e. the rotation angle around the *z*-axis.

2.2. Computational procedure

The phase A of PAALA-18 was simulated using an advanced MC sampling technique (Continuum Configurational Bias, CCB-MC) [13,14]. The CCB method consists of the following three steps: (i) a chain is selected at random; (ii) the chain is cut at a random position; (iii) the chain is sequentially regrown. The chain is regrown bond-by-bond by examining a number of possible position, which are chosen randomly. In order to ensure the condition of microscopic reversibility an appropriate transition probability is chosen [13,14]. This method was initially developed to be efficient in the study of dense systems and has been successfully used in the simulations of the crystal structure of PAALA-4 [15] and the phase B of PAALA-n with $n \geq 12$ [7,9]. It should be emphasized that the aim of this work is to obtain an atomistic model for the phase A of PAALA-18. Accordingly, the available experimental information [6] has been used to restrict the simulations to the desired phase, as will be discussed below.

Since the box used in the simulations consists of four independent chains of 13 residues, a typical simulation deals with 1404 atoms. All the simulations were of NVT type (T = 298 K) considering both periodic continuation conditions and the minimum-image convention. Initially, the box edge *b* along the *y*-axis was slowly driven from 36 to 31 Å in order to avoid strong steric clashes between the side chains belonging to different layers. This was done by using six MC simulations of 5×10^4 steps while such distance is decreased in 1 Å decrements. After this, an equilibration of 5×10^4 steps was performed in order to sample the setting angles. Finally, a MC simulation was run for a total of 2×10^5 steps and co-ordinates were saved every 2000 steps.

The Amber force-field [16] was used to represent the electrostatic, van der Waals and torsional energies of the system. Both methyl and methylene groups were described considering a model of united atoms and their van der Waals energy was computed in the usual pairwise additive way using a Lennard-Jones 6-12 potential. Electrostatic charges were determined by fitting the molecular electrostatic potential derived from quantum mechanical calculations to the classical one. Electrostatic interactions were evaluated using a standard Coulombic potential. Nonbonding interactions were truncated at 8 Å.

3. Results and discussion

In a first step, MC simulations were performed following the computational procedure described in Section 2, i.e. considering all the dihedral angles of the alkyl side chains as degrees of freedom. Inspection to the resulting microstructures revealed a predominantly disordered state of the inter-layer region (Fig. 3a). Such disorder is in opposition with what should be expected for the crystalline phase A,

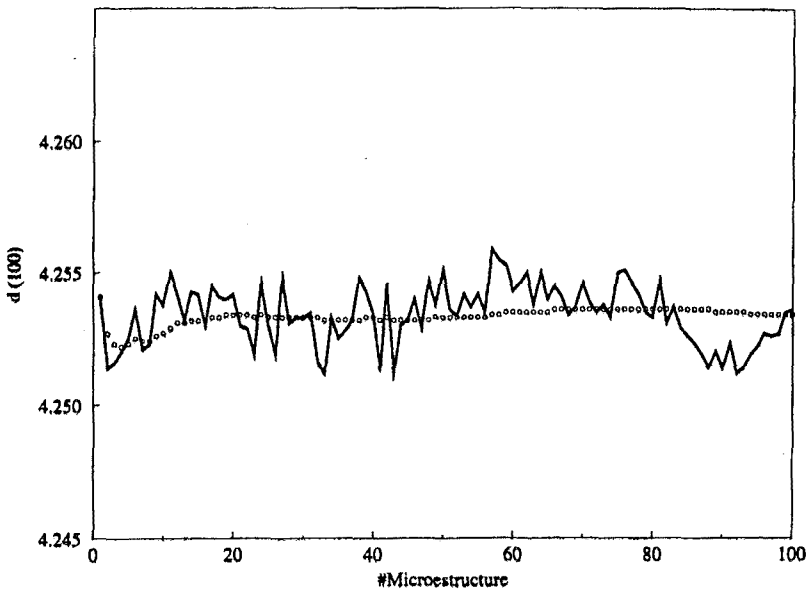

Fig. 4. Simulated spacing of the (100) reflection for each microstructure of PAALA-18 (solid line) as well as the running average along the simulation (dots).

which is conceived as an ordered state with a majority of the C–C bonds in the alkyl side chain adopting a *trans* conformation. This model is experimentally supported by both DSC and wide-angle X-ray scattering, which reflect crystallization of the paraffinic side chains. However, the side chains of the microstructures provided by MC simulations present a considerable number of C–C bonds in *gauche* conformation, which causes the side chains to be in a partially disordered state. Indeed, the results obtained from these simulations are essentially the same than those obtained when the phase B of PAALA-*n* with $n \geq 12$ was explicitly simulated [9].[2] Thus, the only order detected in Fig. 3a is the tendency of the side chains to align along the *b*-axis.

The failure to reproduce the crystallization of the paraffinic chains is due to the MC method by itself. It is known that MC simulations of alkanes below the experimental melting point lead to supercooled liquids rather than to crystals [17]. Since the goal of this work is to obtain a molecular model of the crystallized phase, we have constrained the conformation of some torsional angles of the alkyl side chains in order to facilitate the crystallization. Thus, the three central torsional angles included in the aliphatic segment that is not involved in the side chain bending were kept fixed at *trans*. CCB-MC simulations were run again using the computational procedure described in Section 2 but introducing the new constraints. It should be noted that these constraints should help in the crystallization process performing as a nucleus of the paraffin crystal lattice. In this case, simulations led to a highly ordered structure. Thus, the presence of order in the three axes allows to identify the phase A. Fig. 3b shows one of the microstructures generated from the latter simulations.

3.1. Structure and conformation of the alkyl side chains

The hexagonal arrangement of the alkyl side chains in PAALA-18 was evidenced in the electron diffraction diagrams obtained from casted thin films of this polymer [6]. In these diagrams as well as in the wide-angle region of the fibre X-ray diagrams, the (100) reflection with a spacing of 4.2 Å was observed. Accordingly, it was concluded that the side chains are separated within the hexagonal lattice by a distance of 4.2 Å/sin 60° = 4.9 Å. Fig. 4 shows the simulated spacing of the (100) reflection for each microstructure as well as the running average over the points. This spacing have been obtained from the distance between each side chain and its closest neighbours. For all the microstructures, the distances between one side chain and its six closest neighbours were very similar, the standard deviation associated to each dot represented in Fig. 4 being lower than 0.005 Å. As it can be seen, the spacing ranges from 4.251 and 4.255 Å along the simulation, this small variation being also consistent with a hexagonal pattern in which all the distances have the same value. On the other hand, the spacing obtained along the MC simulations is about 0.05 Å overestimated with respect to the experimental value. However, the average value of this spacing allows to estimate a distance between the side chains of 4.253 Å/sin 60° = 4.91 Å, which is in excellent agreement with the value derived using the experimental spacing.

Overall the results indicates that the hexagonal packing

[2] The phase B of PAALA-18 was investigated using MC simulations of the NPT type at 358 K. In those simulations the degrees of freedom were the torsional angles of the side chains and the length of the *b* edge of the cell.

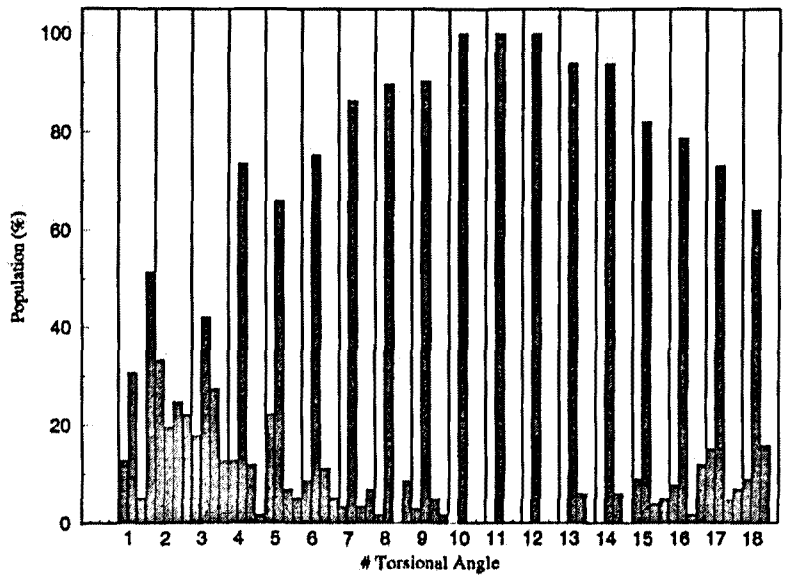

Fig. 5. Torsional angles distribution for the 13 residues contained in the helix repeat of PAALA-18. The population analysis of the torsional angle associated to each of the 18 bonds in the alkyl side chain is specified. The four categories considered for each bond, in the order displayed in the figure from left to right, are: *gauche*$^+$; *trans*; *gauche*$^-$; and the remaining conformers.

predicted by MC simulations for the side chains of PAALA-18 is in remarkable agreement with the available experimental information. According to this, it can be concluded that the structure displayed in Fig. 3b provides a very suitable description of the phase A of PAALA-18.

In order to get a deeper insight in the side chain structure, the corresponding torsional angles for the alkyl side chains of the 13 residues contained in the helix repeat of PAALA-18 were analyzed. Fig. 5 shows a population analysis for each torsional angle, the conformations being grouped in four categories: *gauche*$^-$; *trans*; *gauche*$^+$; and the remaining conformers. As it can be seen, the population of the folded states, i.e. those different from *trans*, is considerable for the first five torsional angles, even although the *trans* is, in general, the predominant conformation. This is not a surprising result since these torsional angles are involved

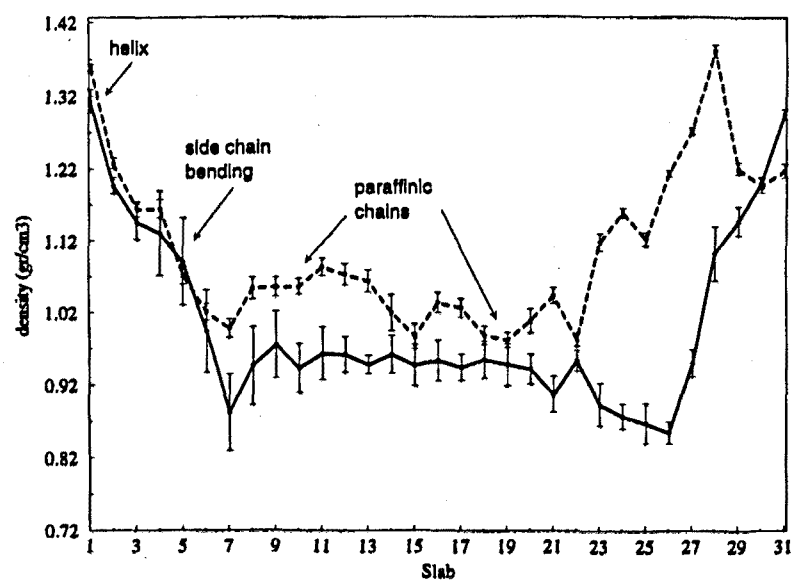

Fig. 6. Local density profiles of the phases A (solid line) and B (dashed line) of PAALA-18 along the *y*-axis.

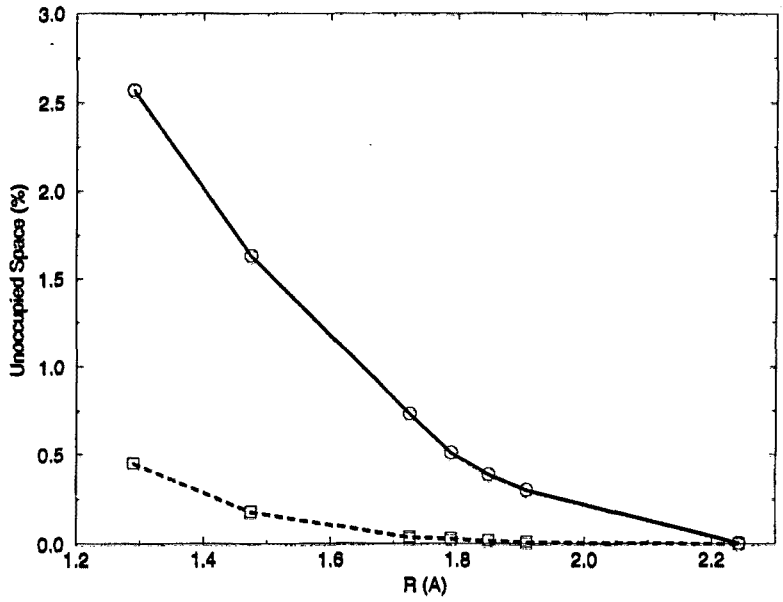

Fig. 7. Variation of the unoccupied space (in %) versus the radii of the prove particle (in Å) for the phases A (solid line) and B (dashed line) of PAALA-18.

in the side chain bending region, where the presence of folded conformations is required to orient the side chain perpendicular to the helix axis. On the other hand, for the 7th to the 15th torsional angles the population of the *trans* conformation is larger than 80% while that of the folded conformations is considerably small. As it was discussed above, the torsional angles 10th, 11th and 12th (Fig. 5) the conformation was kept fixed at *trans* along the simulations. However, it should be emphasized that although the remaining torsional angles were allowed to vary without any restriction, the *trans* conformation was finally adopted in all of them. These results indicate that once the nucleus of the crystal is built by fixing three torsional angles, the contiguous methylene units tend to crystallize spontaneously. Finally, the *trans* is clearly the predominant conformer for the 16th, 17th and 18th torsional angles. However, the populations of folded conformations increase with respect to those of the central segment of the alkyl side chain revealing a partial flexibility.

The experimental evidences available for the phase A of PAALA-18 reveal that the approximate number of crystallized methylenes is around 8 [6]. Starting from 3 torsional angles in *trans* conformation, the simulations evolved spontaneously to 9 torsional angles with such conformation. This feature points out the remarkable agreement between theoretical and experimental results. Thus, the method is perfectly capable of reproducing the phase A of PAALA's if the tendency to evolve towards a supercooled liquid is overcome by imposing the appropriate restrictions.

3.2. Density profile

The local density profile of phase A of PAALA-18 was calculated by adding the mass of all the atoms located in a given slab of the structure and dividing it by the volume of the slab. A total of 31 slabs with a thickness of 3 Å were built along the *y*-axis. The computed density profile is displayed in Fig. 6. The local density in the helix region was found to be clearly greater than in the paraffinic region. Thus, the density decreases from 1.31 to about 0.85–0.90 g/cm^3 along the *y*-axis. It is worth noting that the local density is quite homogeneous along all the interlayer paraffinic region indicating a similar mass distribution in both the side bending and the crystallized regions. The mass density of the paraffinic region is between that of a fully disordered liquid alkane, i.e. 0.76 g/cm^3 for liquid C_{18} at the same temperature, and a highly ordered alkane, i.e. 1.00 g/cm^3 for the orthorhombic crystal form of polyethylene.

The local density profile of the phase B of PAALA-18 has been computed using the microstructures obtained in previous MC simulations [7,9]. Results are included in Fig. 6 for comparison. As it can be seen the local density in the paraffinic pool of the phase B is about 0.15 g/cm^3 larger than that computed for the paraffinic region of the phase A. This result is in excellent agreement with the experimental observation. Thus, PAALA-*n* with $n \geq 12$ get denser as the transition temperature T_1 is raised. Accordingly, the observed densities for the phases A and B of PAALA-18 are 1.03 and 1.14 g/cm^3, respectively.

3.3. Measurement of the unoccupied space

The unoccupied space refers to the volume not occupied by the atoms of the system. The measurement of the unoccupied space is highly desirable since it allows to predict the behaviour of the system against small penetrants [7,15].

Unoccupied space estimations of the phases A and B of PAALA-18 were done by dividing the simulation box of every microstructure into a three-dimensional uniformly spaced grid. These grids consisted of 81,180 and 74,460 nodes for phases A and B, respectively. Then an spherical probe particle with a radius R was centred in each node and the distance to the nearest atom of the polymeric matrix was measured. If this distance was larger than the sum of the van der Waals radii of the probe particle and the polymer atom, the node was identified as unoccupied. Seven different radii R were chosen for the probe particle, which correspond to small gas penetrants: 1.29 (He); 1.475 (H_2); 1.725 (Ar); 1.79 (O_2); 1.849 (N_2); 1.909 (CH_4); and 2.243 Å (CO_2). The van der Waals radii of the polymer atoms were taken from Amber libraries [16].

The results derived from the analysis of the unoccupied space in all the generated microstructures are summarized in Fig. 7, which displays the amount of unoccupied space averaged over the 100 microstructures recorded for the phases A and B of PAALA-18. It can be seen that the amount of unoccupied space decreases when the phase A changes to phase B. This is a very reasonable result since the former has a lower density than the latter. Thus, even although the phase B is less ordered than the phase A the space is more filled in the former. An inspection to the microstructures of phases A and B of PAALA-18 has revealed that the phase A presents a considerable amount of unoccupied space around the region of side chain bending. The densification that accompanies the phase change lead to a drastic reduction of the unoccupied space in such region.

On the other hand, the results indicate that the unoccupied space decreases with the increase of the size of the probe particle, the space available being almost negligible for the larger ones. Moreover, the ratio between the unoccupied spaces estimated for the phases A and B increases with the size of the probe particle. Accordingly, the ratio change from 6 to 19 when the radius increases from 1.29 to 1.725 Å. This trend confirms that the space is more uniformly filled when the alkyl side chains are melt than when they are crystallized. Thus, in order that the quantity of unoccupied space reached a negligible value, i.e. lower than 0.25%, particles with a radius of approximately 1.975 and 1.45 Å are needed for the phases A and B of PAALA-18, respectively.

4. Conclusions

The structural behaviour of the phase A of PAALA-18 has been investigated using MC simulations. The results together with those obtained for the phase B of the same polymer provide a complete picture of the structural changes involved in the first thermal transition of PAALA-n with $n \geq 12$. The position of the alkyl side chains in the interhelical region predicts the crystallization of about 8–10 methylene groups. Furthermore, this paraffinic lattice adopts a hexagonal arrangement with the side chain separated by 4.9 Å and extended normal to the helix axis, in excellent agreement with the experimental data. The density profile obtained from our simulations indicates that the local density is quite homogeneous along all the interlayer region and much lower than that of the space occupied by the main chain helices. The side bending and the crystallized regions present a similar mass distribution in the phase A of PAALA-18. On the other hand, the phase B is denser than the phase A, the former offering a lower amount of unoccupied space than the latter.

Acknowledgements

This work was supported by DGICYT (PB96-0490). DZ and SL acknowledge the support of the Ministry of Education of Spain. AMN thanks financial support to FAPESP when in Spain. Authors thank to CESCA and CEPBA for computational facilities.

References

[1] Daly WH, Poché D, Negulescu II. Prog Polym Sci 1994;19:79.
[2] Watanabe J, Ono H, Uematsu I, Abe A. Macromolecules 1985;18:2141.
[3] Sakamoto R, Osawa A. Mol Cryst Liq Cryst 1987;153:385.
[4] Watanabe J, Nagase T. Macromolecules 1988;21:171.
[5] Romero Colomer FJ, Gómez Ribelles JL, Lloveras Macía J, Muñoz-Guerra S. Polymer 1991;32:1642.
[6] López-Carrasquero F, Montserrat S, Martínez de Ilarduya A, Muñoz-Guerra S. Macromolecules 1995;28:5535.
[7] Zanuy D, Alemán C, López-Carrasquero F, Báez ME, García-Alvarez M, Laso M, Muñoz-Guerra S. Macromol Chem Phys (in press).
[8] Navas JJ, Alemán C, López-Carrasquero F, Muñoz-Guerra S. Polymer 1997;38:3477.
[9] León S, Alemán C, Muñoz-Guerra S, Laso M. J Theor Comput Polym Sci 2000;10:177.
[10] Navas JJ, Alemán C, López-Carrasquero F. Macromolecules 1995;28:4487.
[11] López-Carrasquero F, García-Alvarez M, Navas JJ, Alemán C, Muñoz-Guerra S. Macromolecules 1996;29:8449.
[12] Broadhurst MG. J Res Natl Bur Stand 1962;66A:241.
[13] de Pablo JJ, Laso M, Suter UW. J Chem Phys 1992;96:6157.
[14] de Pablo JJ, Laso M, Suter UW. Macromolecules 1993;26:6180.
[15] Zanuy D, León S, Alemán C, Muñoz-Guerra S. Polymer 2000;41:4169.
[16] Weiner SJ, Kollman PA, Case DA, Singh UC, Ghio C, Alagona G, Profeta S, Weiner P. J Am Chem Soc 1984;106:765.
[17] Widmann AH, Laso M, Suter UW. J Chem Phys 1995;102:5761.

VII.6. Estudio de los cambios estructurales implicados en la transición entre la fase B y la fase C

Una vez caracterizadas las fases A (apartado VII.5) y B (León et al., 2000b) de los PAALA-*n*, se procedió a estudiar la transición entre las fases B y C. La investigación de este proceso es especialmente compleja, puesto que la fase C de los PAALA-*n* se caracteriza por presentar un alto grado de desorden estructural. Desde un punto de vista metodológico el punto más crítico del estudio es la pérdida del empaquetamiento de las cadenas de polímero en todas las direcciones del espacio (López-Carrasquero et al., 1995). La aproximación empleada en las simulaciones de las fases A y B, referente al pequeño número de cadenas explícitas usadas, muy probablemente no resultará válida para la fase C. Para las otras dos fases, en las que existía una ordenación tridimesional de las hélices de polímero, fue posible emplear únicamente cuatro cadenas explícitas, en la caja de simulación, de forma que el resto del sistema se describía mediante la aplicación de condiciones periódicas de contorno. Sin embargo, el desorden de las cadenas de polímero característico de la fase C hizo necesario cambiar el modelo de simulación. Las interacciones entre cadenas cercanas en esta fase ya no podían considerarse equivalentes a lo largo de las tres direcciones en que se estructuraban las fases A y B. En este caso se construyó una caja de simulación mucho mayor, con más cadenas explícitas, para poder tener una visión más amplia de los cambios estructurales que se pretendían estudiar. De este modo se pudo contabilizar una mayor cantidad de interacciones entre las cadenas poliméricas que, a la postre, determinarían su estructuración final.

Un aspecto interesante a tener en cuenta es la conformación de las cadenas laterales puesto que, a partir de las observaciones experimentales, se dedujo que debían sufrir un cambio considerable con respecto a las fases A y B. Esta conclusión se sustentaba en la interpretación de los resultados de difracción de rayos X a bajo ángulo. En el PAALA-18 se observó que a altas temperatura (superiores a T_2), la reflexión ecuatorial característica de estos polímeros aparecía entre 23-24 Å, lo cual implicaba que las cadenas de polímero de láminas diferentes se acercasen aproximadamente 4 Å con respecto a la fase B. Este hecho, a priori, solo puede entenderse si se considera que las cadenas de la fase parafínica se compactan. Es decir, pierden por completo su

tendencia a adoptar conformaciones extendidas. A su vez, esta interpretación permitiría entender las propiedades de cristal líquido observadas en la fase C. Una disminución en la distancia extremo - extremo de las cadenas laterales favorecería el desplazamiento de las cadenas del polímero a lo largo del eje *z*.

VII.6.1 Métodos

VII.6.1.1 *Modelo molecular*

Como consecuencia de lo expuesto anteriormente, se debió construir un modelo de simulación mucho mayor que el empleado en el estudio de las fases A y B. En estas simulaciones se empleó un sistema con 16 cadenas de polímero explícitas (figura **VII.7**). Cada cadena estaba constituida por 13 residuos, en conformación helicoidal de simetría 13/4. El sistema, en consecuencia, presentaba en total 5616 átomos. Haciendo una analogía con la fase B, puede decirse que el sistema empleado equivalía a 4 láminas de cadenas polipeptídicas. Por coherencia con el modelo aceptado para la estructura de las fases más ordenadas, la disposición entre cadenas adyacentes se consideró antiparalela.

El modelo descrito se construyó en una caja de simulación ortogonal de dimensiones a = 112.0 Å, b = 49.8 Å y c = 21.998 Å. Teniendo en cuenta el tamaño de dicha caja, las láminas del polímero estarían separadas por 28.0 Å y la distancia entre cadenas de una misma lámina sería de 12.3 Å. Esto equivale a decir que se partió de una estructura molecular análoga a la de la fase B.

Por cuestiones de eficiencia computacional se empleó un modelo de *United Atom* para describir los grupos metileno y metilo. Mediante este modelo los hidrógenos de dichos grupos no se representan explícitamente, sino que el efecto de los mismos queda incluido en los parámetros de van der Waals de los carbonos de dichos grupos.

Por la misma razón, y teniendo en cuenta los datos experimentales, en los que se demostraba que en todo el rango de temperaturas estudiado se mantenía la conformación helicoidal, se mantuvo la geometría de la cadena principal fija. El movimiento de las cadenas laterales se simuló manteniéndose las distancias y ángulos

de enlace en sus valores de equilibrio. Es decir únicamente se exploró el espacio conformacional de las cadenas laterales en términos de ángulos de torsión.

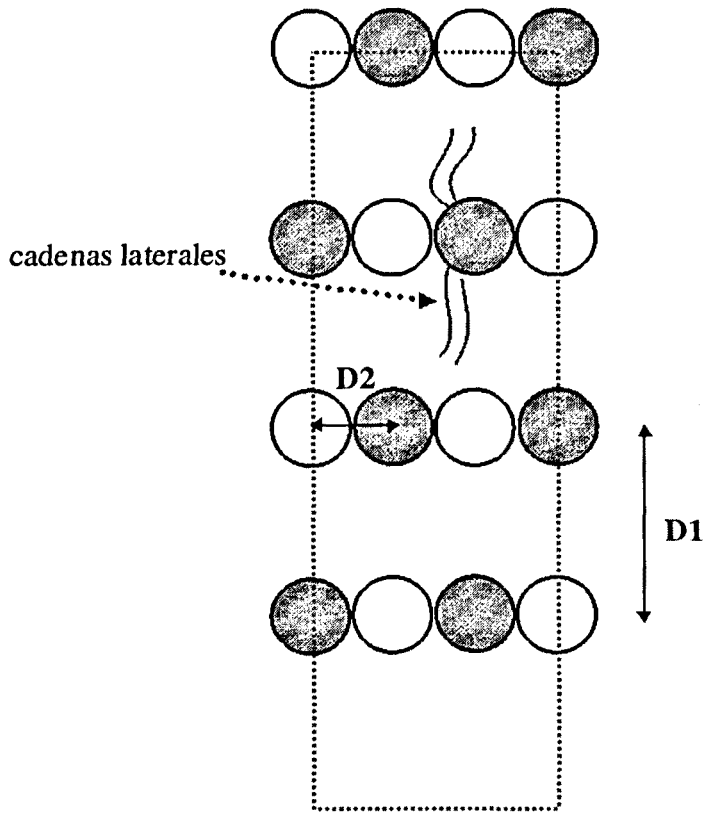

Figura VII.7. Representación esquemática de la caja de simulación. Las esferas oscuras corresponden a las cadenas antiparalelas. Las distancias D1 y D2 corresponden a la distancia entre cadenas de distintas láminas y de una misma lámina, respectivamente.

VII.6.1.2 *Detalles computacionales*

El estudio de la fase C se llevó a cabo de forma similar al de las fases A y B, mediante el uso de la metodología MC-CB, empleándose la versión paralelizada del programa MCDP (León et al., 2001) en una estación de trabajo *Origin* de 128 procesadores del Centro Europeo de Paralelismo de Barcelona (*CEPBA*).

Como geometría de partida se empleó una de las microestructuras resultantes de las simulaciones *NPT* de la fase B (León, 2000d), la cual se equilibró a 377 K durante ($8 \cdot 10^4$ pasos de simulación) manteniendo las distancias entre cadenas fijas a 28 Å. Así, durante esta simulación únicamente se optimizó la conformación de las cadenas parafínicas, manteniéndose constante el tamaño de la caja de simulación (condiciones

NVT). A partir de este punto se empezaron las simulaciones de la transición entre las fases B y C, las cuales se realizaron a presión constante (1 atm) dejando variar el volumen de la caja de simulación (*NPT*).

Para el cálculo de la energía se empleó el campo de fuerzas de AMBER (Cornell et al., 1995), usándose sus parámetros para todas las componentes de la energía a excepción de las cargas atómicas. El término electrostático se calculó empleando las cargas atómicas calculadas por Navas et al. (1997) para toda la familia de los PAALA-*n*, con $n \geq 8$. El *cutoff* usado fue de 12.0Å.

En dos simulaciones de $7.5 \cdot 10^4$ pasos se aumentó la temperatura de 377 a 397 K y de 397k a 417 K, guardándose una estructura cada 2000 pasos para su posterior análisis. A estas dos simulaciones en las que la temperatura se incrementó 40 K les siguió una tercera de $5 \cdot 10^5$ pasos a 417 K, durante la cual se guardó una microestructura cada 2000 pasos para su posterior análisis.

El tipo de movimientos realizados en cada simulación y la frecuencia relativa de cada uno se resumen en la tabla **VII.2.**

Tabla VII.2. Resumen de las condiciones empleadas en las 4 simulaciones del PAALA-18. Para cada una de ellas se detalla el número de pasos, la frecuencia relativa en que se daba un tipo determinado de movimiento (en cursiva) y el incremento máximo permitido para cada parámetro del sistema (Δ). La suma de todas las frecuencias relativas es 100.

Ciclo		**Tipo de movimiento**							
	Pasos	**CB**[a]	**Metropolis**[a]	**NPT**					
				[b] **a/b**	**Δ(a/b)**	**θ**[c]	**Δθ**	**Ind.**[d]	**Δ**
1[e]	$8 \cdot 10^4$	*80*	*20*	-----	-----	-----	-----	-----	-----
2	$7.5 \cdot 10^4$	*40*	*10*	*20*	0.2	*20*	0.5	*10*	0.2
3	$7.5 \cdot 10^4$	*40*	*10*	*20*	0.2	*20*	0.5	*10*	0.2
4	$5 \cdot 10^5$	*32*	*8*	*20*	0.2	*20*	0.5	*20*	0.5

[a] Movimiento de las torsiones de las cadenas laterales
[b] Cambio en los parámetros *a* o *b* de la caja. El incremento (Δ(a/b)) se da en Å
[c] Movimiento del *setting angle* de todas las cadenas. El incremento (Δθ) se da en grados.
[d] Cualquier tipo movimiento como cadenas independientes (desplazamiento a lo largo de *a*, *b*, *c* o cambios de su *setting angle* con respecto la posición de referencia, que es la cadena que presenta su eje helicoidal en el centro de coordenadas). Los incrementos son los mismos para los ángulos y los desplazamientos y se dan grados y Å, respectivamente.
[e] Simulación NVT.

VII.6.2. Resultados

VII.6.2.1. Estructura y empaquetamiento de las cadenas de polímero

El proceso simulado fue estudiado mediante el seguimiento de diferentes parámetros estructurales. La figura **VII.8** muestra la evolución de los parámetros *a* y *b* a lo largo de las tres simulaciones de tipo *NPT*.

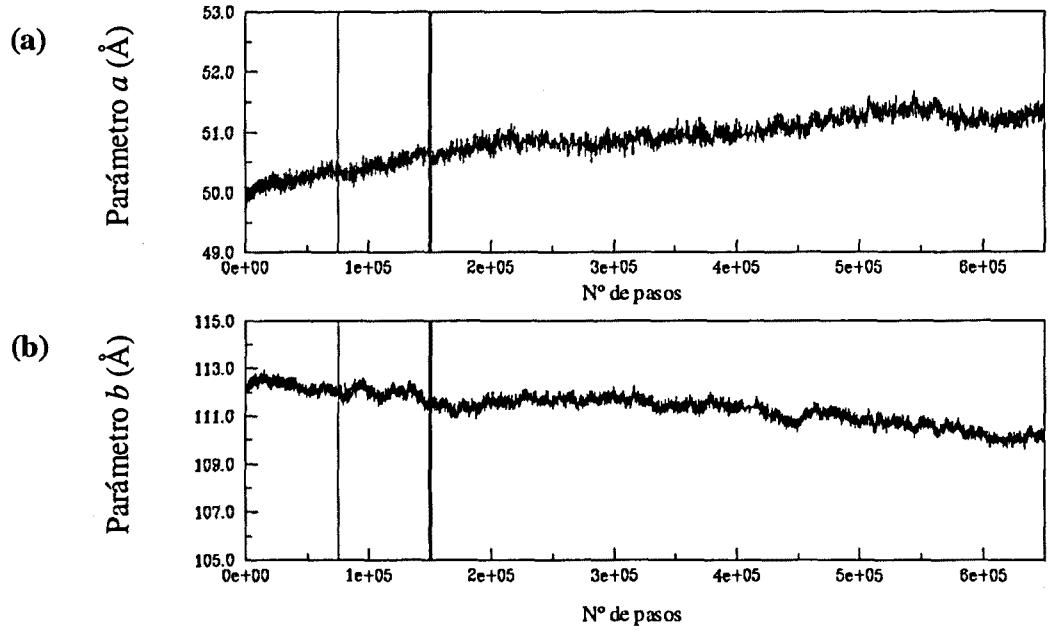

Figura VII.8. Representación de la evolución de los parámetros correspondientes al tamaño de la caja de simulación *a* **(a)** y *b* **(b)** del PAALA-18 a lo largo de la trayectoria. Las líneas verticales corresponden al aumento de temperatura de 377 K → 397 K y 397 K → 417 K, respectivamente.

Tal como puede verse, los cambios en el volumen del sistema no resultan muy grandes. El sistema tiende a mantener su densidad, puesto que el valor del parámetro *a* disminuye al mismo tiempo que el de *b* aumenta. Es decir, aparentemente las cadenas de polímero que se encuentran en diferentes láminas tienden a acercarse mientras que las cadenas de polímero que están en una misma lámina tienden a alejarse.

Una de las características más destacables de la fase C es el aumento de la movilidad entre las cadenas de polímero, que permite la pérdida de la estructuración

laminar. Este fenómeno fue estudiado siguiendo los desplazamientos de las 16 cadenas de polímero respecto a su posición inicial.

Tal como queda reflejado en las figuras **VII.9a** y **VII.9b**, la tendencia a perder el empaquetamiento al aumentar la temperatura es parecida a la descrita para el comportamiento de los parámetros de la caja de simulación. Las cadenas de polímero que en la fase B se encontraban en la misma lámina tienden a alejarse, llegándose a desplazamientos de hasta 2 Å respecto su posición inicial. Por contra la distancia entre cadenas de distintas láminas tiende a disminuir al aumentar la temperatura presentando desplazamientos del mismo orden pero en sentido opuesto.

Debe destacarse que también se pudo reproducir el movimiento de las cadenas de polímero a lo largo del eje *c*. Sin embargo, los valores de estos desplazamientos fueron muy inferiores a los observados en las dos otras direcciones del espacio. No obstante, los resultados mostrados en la figura **VII.9c** reflejan claramente la tendencia de las cadenas de polímero a moverse a lo largo de dicho eje. Este movimiento es característico de la estructura de cristal líquido observada experimentalmente.

Sin embargo, un análisis detallado de las posiciones relativas entre cadenas revela que después de los $6.5 \cdot 10^5$ pasos de simulación, la ubicación de las cadenas en la caja de simulación es menos desordenada de lo que se puede esperar a partir de los anteriores resultados. En la figura **VII.10** se muestran las evoluciones de las distancias entre cadenas separadas por la fase alifática (denominadas D1 en la figura **VII.7**) y de las distancias entre cadenas vecinas dentro de una misma lámina (denominadas D2 en la figura **VII.7**). En este caso se midió directamente la distancia entre los centros de las hélices en lugar de evaluar el recorrido que cada hélice había realizado. La diferencia entre las distancias iniciales (28.0 y 12.3 Å, respectivamente) y la de cada paso, corresponde al desplazamiento relativo entre cadenas cercanas en el espacio.

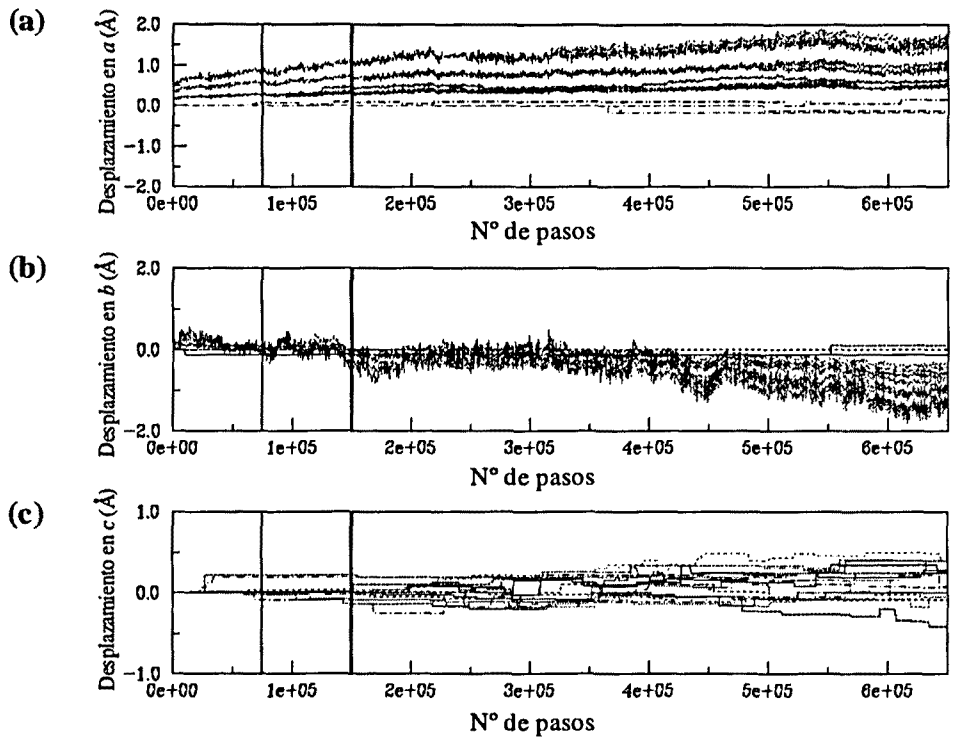

Figura VII.9. Evolución del desplazamiento de cada cadena de polímero a lo largo de los ejes *a* **(a)**, *b* **(b)** y *c* **(c)** durante la simulación de Monte Carlo. Las líneas verticales corresponden al aumento de temperatura de 377 K → 397 K y 397 K → 417 K, respectivamente.

Tal como puede verse las preferencias estructurales del sistema son parejas a las que se deducían mediante el seguimiento del desplazamiento absoluto de las cadenas, pero los movimientos relativos entre cadenas resultan ser mucho menores (entre 0.5 Å y 0.8 Å). Aunque no se haya observado un gran incremento en los parámetros medidos, los cambios estructurales descritos en estas simulaciones indican que se tiende a perder la estructuración laminar.

El análisis realizado de los cambios en la estructuración de las cadenas revela que se reprodujo parcialmente la transición estudiada. Sin embargo, en nuestra simulación no se pudo completar el proceso de fusión. Es importante destacar que el número de pasos realizados no parece ser suficiente, especialmente si se tienen en cuenta los estudios precedentes realizados para el PAALA-18. Tanto para la fase A como para la fase B, se necesitaron del orden $2.5 \cdot 10^5$ pasos para obtener una descripción representativa del sistema estudiado, empleando un modelo molecular con 4 cadenas de

polímero (1404 átomos). Atendiendo a dichos estudios, parece razonable suponer que si se pudiera alargar nuestra simulación, se obtendría una estructura final totalmente desorganizada. Sin embargo, el tamaño del sistema empleado implica un gasto de recursos computacionales que no está a nuestro alcance.

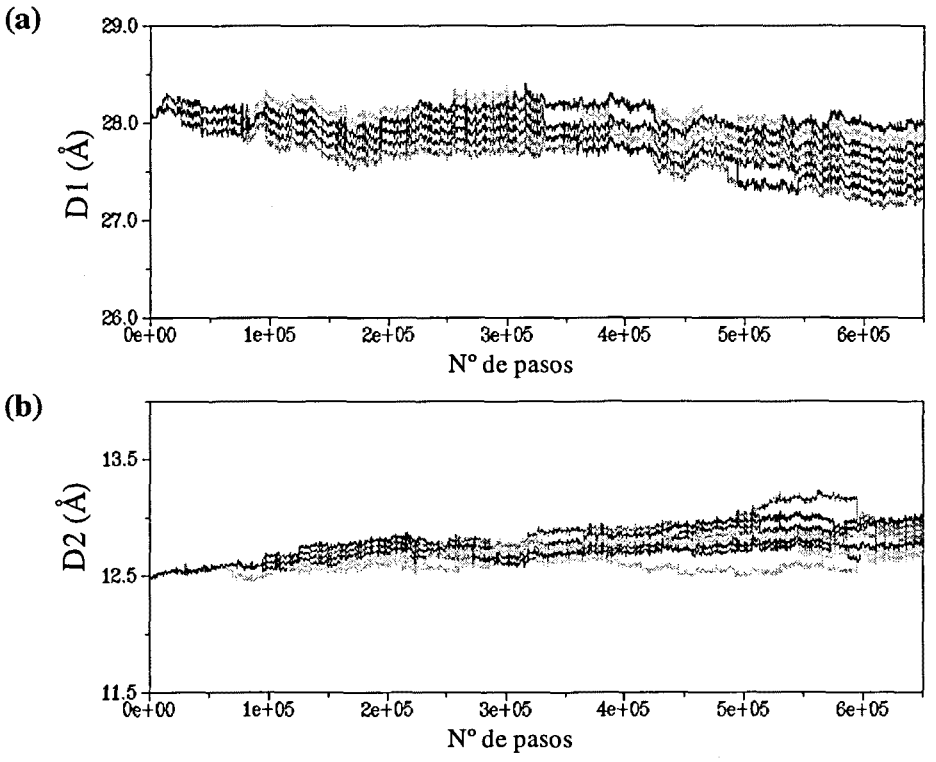

Figura VII.10. Representación de la evolución de las distancias más cortas entre cadenas de polímero de diferentes láminas, D1 **(a)** y de las distancias más cortas entre cadenas de polímero de la misma lámina, D2 **(b)**.

VII.2.2. Estructuración de las cadenas alquílicas:

Uno de los puntos que se supone clave para que se dé la transición entre las fases B y C es la manera en que se organizan las cadenas laterales del polímero. Tal como ya se ha dicho, el acortamiento en la distancia entre cadenas de polímero debería ser consecuencia de importantes cambios en la conformación de las cadenas laterales. Concretamente, debería perderse la marcada tendencia que presentan las cadenas alquílicas a estructurarse en conformaciones extendidas.

Este cambio se investigó siguiendo el cambio en la distancia extremo - extremo de todas cadenas laterales. En la figura **VII.11** se muestra la evolución de dicha distancia para las trece cadenas laterales de dos de las hélices ubicadas en el centro del sistema estudiado. Teniendo en cuenta que la distancia extremo - extremo para una cadena de octadecilo en conformación todo *trans* es aproximadamente 21.2 Å, puede observase como las cadenas laterales estudiadas tienden a perder la conformación extendida.

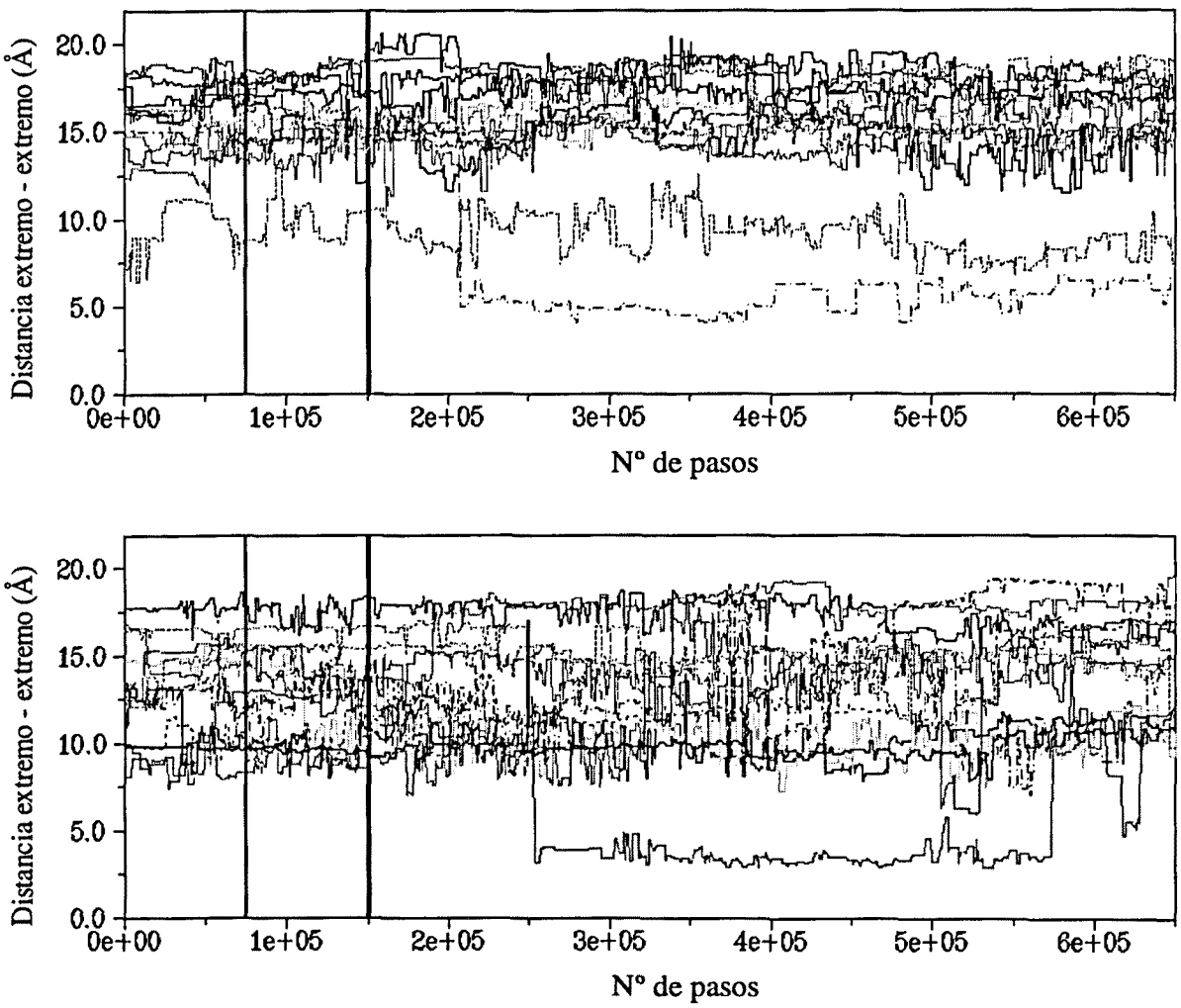

Figura VII.11. Evolución de la distancia extremo - extremo de las 13 cadenas laterales de dos hélices diferentes ubicadas en el centro del sistema simulado. Cada gráfica corresponde a una hélice. Las líneas verticales corresponden al aumento de temperatura de 377 K → 397 K y 397 K → 417 K, respectivamente

Sin embargo, si se hace una análisis más generalizado se puede constatar que la tendencia general del sistema es la anteriormente observada. En la figura **VII.12** se muestra un análisis de poblaciones de las distancias extremo - extremo. Cada $5 \cdot 10^4$ pasos se promediaron el número de cadenas laterales que presentaban una distancia extremo - extremo determinada (el criterio de selección se muestra en la figura). Puede apreciarse una pequeña tendencia a aumentar la presencia de cadenas laterales en conformaciones parcialmente extendidas. Es destacable el incremento de la población de cadenas alquílicas con una distancia extremo - extremo entre 17 Å y 13 Å, desde un 40% al principio de la simulación a un 55% al final de la misma. A su vez, puede verse como disminuye la población de cadenas laterales plegadas, especialmente en el segmento de población con distancias extremo - extremo entre 9 Å y 13 Å. Estos resultados sugieren que las cadenas plegadas en la zona de *bending* tienden a desestructurarse.

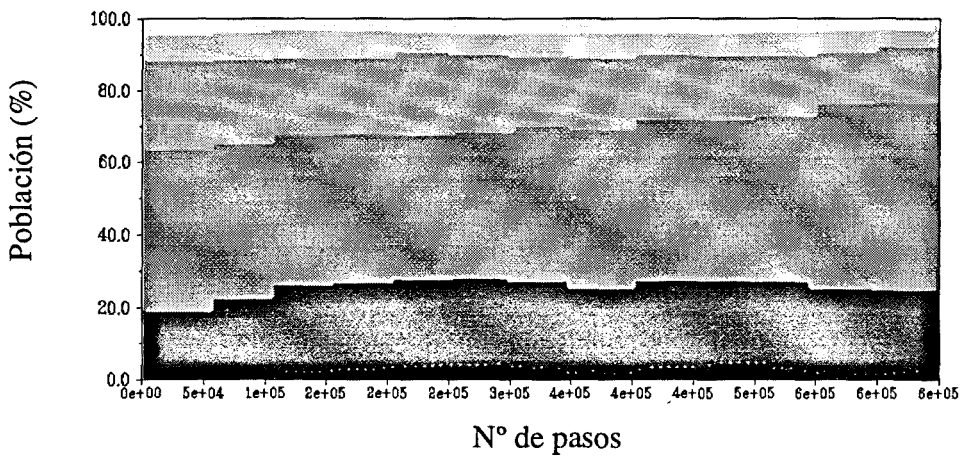

Figura VII.12. Representación de las poblaciones de cadenas alquílicas con una distancia extremo - extremo determinada. De abajo arriba, en una escala de grises decreciente se muestran las poblaciones correspondientes a unas distancias de entre 21.2 y 17 Å, entre 17 y 13 Å, entre 13 y 9 Å, entre 9 y 5 Å, y finalmente, < 5 Å.

Para poder comprender mejor este comportamiento, se estudiaron sus preferencias conformaciones en función de la posición de sus ángulos diedros de libre rotación. En la figura **VII.13** se representa el análisis de poblaciones del tipo de conformación presente en cada ángulo de torsión. Una primera inspección permite constatar que, en consonancia con los valores descritos de las distancias extremo -

extremo, la conformación *trans* sigue siendo la más favorecida. Este dato parece confirmar que realmente no se ha podido reproducir completamente la transición de fase. No obstante, debe destacarse que en todas las posiciones se aprecia una importante presencia de las conformaciones plegadas que posibilita el acortamiento parcial observado en las distancias extremo - extremo. A pesar de ello, la proporción de éstas en la fase C es muy similar a la descrita en la fase B, tal como queda ilustrado en la tabla **VII.3**. Sin embargo, es posible observar un comportamiento ligeramente diferente entre ambas fases: en la fase C la conformación plegada predominante es de tipo *gauche* mientras que en la fase B es la de tipo *skew* la que se encuentra en mayor proporción.

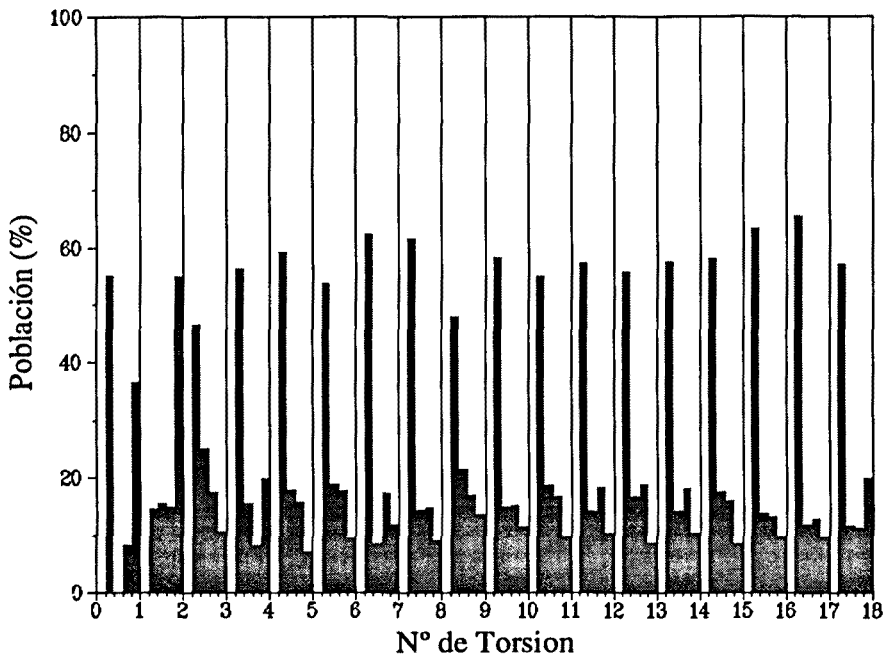

Figura VII.13. Representación del análisis de poblaciones de las conformaciones para los 18 enlaces con libre rotación de la cadena lateral alquílica. Se consideraron 4 categorías diferentes para cada torsión, y en orden de aparición en la figura corresponden a las conformaciones *trans*, *gauche* +, *gauche* - y *skew*. Los resultados corresponden al promedio de todas las estructuras generadas para los últimos $5 \cdot 10^5$ pasos de simulación.

Tabla VII.3. Comparación de las preferencias conformacionales de la cadena del PAALA-18 en las fases A, B y C. Todos los resultados se dan en tanto por ciento. Los valores correspondientes a la fase A son los expuestos previamente en el apartado VII.5, los de la fase B se obtuvieron del trabajo de León et al. (2000b) y los de la fase C son los representados en la figura **VII.13**.

Torsión	trans			gauche			skew		
	A	B	**C**	*A*	B	**C**	*A*	B	**C**
1	*31*	47	**55**	*18*	53	**8**	*51*	0	**37**
2	*20*	25	**15**	*58*	25	**31**	*22*	50	**55**
3	*42*	32	**46**	*45*	10	**43**	*13*	58	**11**
4	*74*	47	**56**	*25*	24	**24**	*2*	29	**20**
5	*66*	28	**59**	*29*	46	**34**	*5*	26	**7**
6	*75*	47	**54**	*20*	24	**37**	*5*	29	**10**
7	*86*	56	**62**	*7*	24	**26**	*7*	20	**12**
8	*90*	41	**61**	*2*	43	**29**	*9*	16	**9**
9	*90*	52	**48**	*8*	27	**38**	*2*	21	**14**
10	*100*	62	**58**	*0*	16	**30**	*0*	22	**12**
11	*100*	41	**55**	*0*	40	**35**	*0*	19	**10**
12	*100*	58	**57**	*0*	22	**32**	*0*	20	**10**
13	*94*	52	**56**	*6*	27	**36**	*0*	21	**9**
14	*94*	53	**57**	*6*	24	**32**	*0*	23	**10**
15	*82*	51	**58**	*13*	25	**33**	*5*	24	**9**
16	*79*	49	**63**	*9*	25	**27**	*12*	26	**10**
17	*73*	50	**65**	*20*	26	**25**	*7*	24	**10**
18	*64*	50	**57**	*25*	24	**23**	*11*	26	**20**

Una inspección más detallada de los datos expuestos en la tabla **VII.3** nos permite constatar nuevas y más marcadas diferencias entre las características conformacionales de las cadenas alquílicas en las fases ordenadas y en la fase C. Mientras que en las fases A y B existía una proporción diferente de conformaciones en función de la posición del ángulo diedro, en la fase C la distribución de conformaciones tiende a hacerse independiente de dicha posición. En las dos fases más ordenadas la preferencia hacia la conformación extendida era muy marcada en los ángulos diedros centrales de la cadena lateral, mientras que en los extremos existía una mayor población de conformaciones plegadas. Sin embargo, en la fase C no parece existir una gran

diversidad conformacional a lo largo de la cadena lateral. Esta tendencia es especialmente marcada en las zonas de *bending* más cercanas a las hélices de polímero (primeras cinco torsiones), las cuales juegan un papel crucial en la ordenación de las cadenas parafínicas. En la fase C, en contraste con las dos otras fases, puede observarse un marcado aumento de las conformaciones *skew* en las dos primeras torsiones y, a su vez, una pérdida parcial del plegamiento en las torsiones siguientes, lo cual parece inducir importantes cambios en la estructuración de la fase alifática. Así mismo, este resultado permite comprender los valores obtenidos en el análisis de poblaciones realizado para las distancias extremo - extremo. El aumento de cadenas laterales con conformaciones parcialmente extendidas es consecuencia de la perdida parcial del plegamiento en las zonas de *bending*.

Estos resultados no son sorprendentes. La característica principal de la fase C es el desorden, especialmente manifiesto en la fase parafínica. El hecho que se pierda la dependencia entre la conformación de la cadena lateral y la posición del enlace, es una muestra más que, a pesar de las limitaciones observadas, el sistema tiende a perder su entidad estructural.

VII.7. Conclusiones parciales

1) La estructuración de las cadenas alquílicas del PAALA-18 en la fase A ha sido estudiada mediante la metodología MC-CB. La posición de las cadenas laterales en la fase parafínica indica que existen entre 8 y 10 grupos metileno cristalizados en excelente concordancia con los datos obtenidos por DSC. Este cristal parafínico adopta una disposición hexagonal donde las cadenas laterales están separadas a 4.9 Å y extendidas perpendicularmente al eje de la hélice. La distribución densidades en la fase A es marcadamente diferente a la fase B. Así, la densidad de la primera es inferior a la de la segunda. Por otro lado, la distribución de densidades en la fase parafínica de la fase A es mucho más homogénea que la de la fase B.

2) Se han caracterizado los cambios estructurales que caracterizan la transición entre las fases B y C mediante simulaciones de MC-CB. Uno de los aspectos más relevantes observados es la pérdida de la diferente distribución conformacional a lo largo de las cadenas alifáticas característica de las fases A y B. Por otro lado, los resultados de la simulación indican que la distancia entre las cadenas de diferentes láminas tiende a disminuir, mientras que la distancia entre cadenas adyacentes de una misma lámina aumenta.

VIII. RESULTADOS:

SOLUBILIDAD DE GASES EN MATRICES POLIMÉRICAS

VIII. SOLUBILIDAD DE GASES EN MATRICES POLIMÉRICAS

Uno de los objetivos finales de la simulación computacional de sistemas químicos es poder explicar e interpretar los fenómenos físicos observables a nivel macroscópico en función de la microestructura del sistema y, en último término, poder predecir las propiedades de un determinado sistema en función de su estructura química. En el campo de la química de los polímeros una de las aplicaciones que ha despertado más expectativas en los últimos 15 años ha sido la simulación de la difusión de gases en matrices constituidas por materiales poliméricos. El uso de algoritmos matemáticos más eficientes junto al incremento de la potencia computacional ha permitido simular con éxito los procesos que rigen el movimiento de gases ligeros en el interior de polímeros (Gusev et al., 1994).

VIII.1. El movimiento de un gas dentro una matriz polimérica

La permeabilidad de gases en matrices de polímeros depende de dos factores: la solubilidad del gas en el polímero, es decir, la cantidad de moléculas de gas que puede ser absorbida y del movimiento de las moléculas de gas dentro del polímero, es decir, la difusión de dichas moléculas.

Está establecido que el movimiento de las moléculas de gas sigue un esquema de "brincos" (*hopping*). Las partículas de soluto se mueven elásticamente y de forma no concertada con el movimiento de la matriz polimérica, dentro de las cavidades que dejan libres las moléculas de polímero. Dependiendo de los cambios conformacionales que el polímero sufre por efecto de las vibraciones térmicas y de la energía cinética del soluto, éste puede "saltar" a una nueva cavidad disponible (Sonnenburg et al., 1990; Müller-Plathe, 1991; Sok et al., 1992).

Este mecanismo nos lleva a uno de los conceptos más importantes en el estudio de los procesos de absorción de gases en sistemas poliméricos, el concepto de *espacio no ocupado* (Ver Figura **VIII.1**). Para que un soluto pueda disolverse en el interior de un polímero es necesario que exista espacio para que éste pueda penetrar en su interior. Se necesita una fracción de volumen que no esté ocupado por los átomos de las cadenas de

polímero. Así, se define la fracción de volumen no ocupado como la cantidad de espacio que dejan libre los átomos del polímero (Cohen et al., 1959; Van Krevelen, 1990).

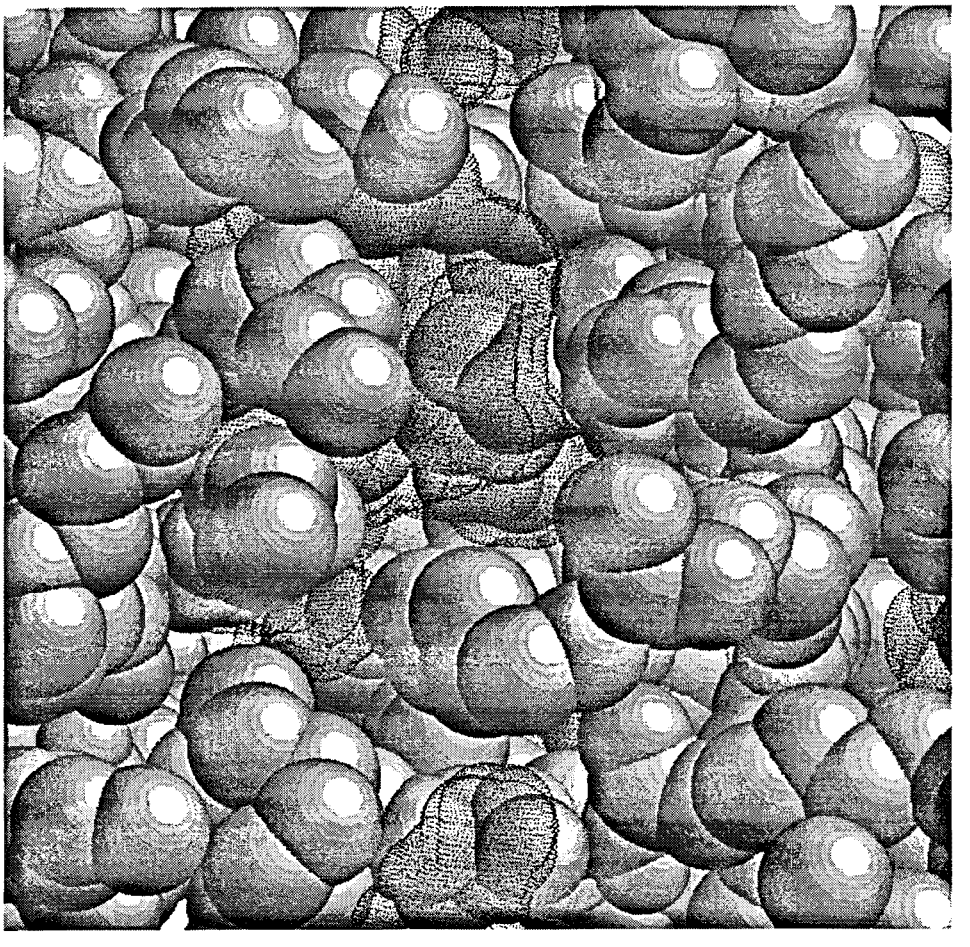

Figura VIII.1. Representación del volumen no ocupado en el seno de una matriz polimérica. Con esferas grises se representan los átomos del polímero y en punteado azul el contorno de las cavidades libres dónde se pueden introducir las moléculas de gas.

Durante mucho tiempo se partió de la base de que la permeabilidad de los gases a través de matrices poliméricas era únicamente debida a la movilidad de las partículas de soluto dentro de la fase amorfa. Este postulado se sustentaba en la posibilidad de que existiera volumen no ocupado en la matriz del polímero. Cuánto más orden hay en un sistema, la densidad del sistema aumenta, existiendo menos posibilidades de que aparezca espacio suficiente para albergar gases en su seno. A su vez, cuanto más denso sea un sistema menos probabilidades hay de que las fluctuaciones conformacionales permitan la aparición de nuevos espacios libres. De aquí que, a pesar de que la mayoría de los polímeros de interés industrial presentan una estructura semicristalina, la mayor parte de los estudios realizados se hayan centrado en estructuras desordenadas.

VIII.1.1. Modelo de absorción dual

La solubilidad de gases en polímeros puede ser explicada en base al modelo de absorción dual (*dual-mode sorption model*). En dicho modelo la solubilidad depende básicamente de dos factores: la disolución comportándose como un sistema fluido (parecido a lo que sucede cuando un gas se disuelve en líquidos) y el efecto que tiene la estructura de la matriz polímerica. Este último factor puede ser interpretado a nivel microscópico como el efecto que produce la existencia de huecos en el seno del polímero antes de que penetren las partículas de gas, combinado con la posibilidad de que aparezcan nuevos espacios accesibles debido al movimiento de las cadenas.

Este comportamiento característico puede ser expresado mediante la siguiente relación (Veith et al., 1966):

$$C_i = kP_i + \frac{C_H b P_i}{1 + bP_i} \qquad (1)$$

Dónde C_i es la concentración molar de gas en el polímero, P_i es la presión parcial de gas en la fase vapor, *k* está relacionada con la constante de Henry en el contexto de éste modelo y C_H y b son constantes empíricas.

Esta ecuación nos permite ver, en función del peso que tenga el término $\frac{C_H b P_i}{1 + bP_i}$, cuanto se aleja la solubilidad de un gas en un polímero del comportamiento de una disolución ideal (Gusev et al., 1994).

VIII.1.2. Aproximación a una disolución ideal. Ley de Henry

Cuando la concentración de gas disuelto en el polímero y la presión de la fase vapor son muy pequeñas puede aproximarse su solubilidad al comportamiento de las disoluciones ideales de gases según la Ley de Henry (ecuación 2): La solubilidad (S_i) de un gas únicamente depende de la presión parcial de dicho gas en la fase vapor.

$$S_i = K_H P_i \qquad (2)$$

Dónde K_H es la constante de Henry.

Poder usar condiciones que aproximen el sistema estudiado a un comportamiento de disolución ideal es muy apropiado ya que la constante de Henry es proporcional al exceso de potencial químico (μ^{ex}) de un soluto en un disolvente a dilución infinita:

$$\mu^{ex}_{x_i \to 0} = -k_b T \ln \frac{1}{K_H k_b T} \qquad (3)$$

Dónde k_b es la constante de Boltzman y T la temperatura (Cuthbert et al., 1997).

De la ecuación 3 se puede aislar K_H, y combinándola con la ecuación 2, a una presión de 1 atmósfera, se llega la siguiente expresión, que nos da el valor de la solubilidad un gas en una matriz polimérica a dilución infinita:

$$S = \frac{1}{RT} \exp\left(\frac{\mu^{ex}}{RT}\right) \qquad (4)$$

Debe notarse que la solubilidad calculada mediante la ecuación 4 se refiere en realidad a un coeficiente de partición, que expresa la solubilidad del gas en el polímero relativa a la presión parcial de dicho gas en la fase vapor (asumiendo un comportamiento ideal del gas)

VIII.1.3. Cálculo del exceso de potencial químico

La estimación del potencial químico en exceso puede hacerse de forma rigurosa mediante el método de inserción de la partícula de prueba propuesto por Widom (*Widom test-particle method*, Widom, 1963; 1982).

El potencial químico en exceso de una especie *i* en un sistema de *N* partículas sin energía cinética depende de la energía potencial de una partícula de la especie *i*

insertada en el interior del sistema de N partículas, en posiciones escogidas al azar (ecuación 5).

$$\beta\mu_i^{ex}(\rho,T) = -\ln\langle\exp(-\beta\phi_t)\rangle_N \qquad (5)$$

Dónde $\beta = 1/k_bT$, ϕ_t es la energía de interacción entre la partícula i y las N partículas del sistema, ρ es la densidad específica del sistema y los corchetes denotan que se trata de un colectivo canónico de N partículas (volumen, masa y temperatura constantes).

VIII.2. Limitaciones de las simulaciones a nivel atómico para el cálculo de la solubilidad

VIII.2.1. Cálculo de la energía de interacción entre un gas y la matriz del polímero

Para poder simular procesos de solubilidad es necesaria una descripción atomística del polímero estudiado. Por su naturaleza macromolecular se debe emplear un sistema con una gran cantidad de átomos. Por otro lado, para poder describir de forma rigurosa las interacciones entre las moléculas de gas y el polímero deberían realizarse cálculos de mecánica cuántica. Actualmente realizar este tipo de cálculos para los sistemas que se quieren estudiar resulta absolutamente inviable, ni tan siquiera mediante métodos en los que se usen expresiones con parámetros ajustados (ya sean semiempíricos o DFT). La limitación básica es el tamaño del sistema que permite ser simulado y que, de forma indirecta, se relaciona con la capacidad de computación asequible actualmente. Por este motivo, las interacciones energéticas que determinan el proceso de solubilidad de gases en polímeros deben calcularse usando campos de fuerza clásicos.

Éste punto es importante porque se requieren parámetros apropiados que describan correctamente las interacciones no enlazantes entre el soluto y los átomos del polímero, para cada unos de los gases que se quiera estudiar.

El potencial de Lennard-Jones ha sido el más usado para calcular estas interacciones (ver ecuación 19 del capítulo de Métodos). Con este potencial se ha

estudiado tanto el efecto del tamaño de la partícula como de la dureza química de la misma, viéndose que el factor que determina la bondad de los cálculos es el radio de van der Waals que se usa para describir la partícula de soluto (Müller-Plate et al., 1992).

VIII.2.2 Implicaciones de la constitución del sistema. La fase amorfa

Como ya se ha comentado anteriormente la simulación de la solubilidad de gases en polímeros se ha realizado históricamente en sistemas amorfos. Esta aproximación parece ser correcta siempre que la densidad de la fase amorfa sea significativamente inferior a la de la fase cristalina. Se asume entonces que la solubilidad y la movilidad de los gases se dan básicamente en la primera.

La naturaleza macromolecular de los polímeros plantea ciertos problemas de tipo estadístico. Conseguir una representación conformacional que permita asumir que el sistema simulado está en equilibrio (para el cálculo de solubilidad) o para que ha llegado al estado estacionario (para la difusión) es técnicamente complicado. Las principales limitaciones que presentan estos tipos de estudios son:

-*Tamaño del sistema y representación del entorno*: Es imposible representar de forma explícita todas las cadenas necesarias y con una longitud suficientemente larga, para poder obtener una constitución química similar a la real. El recurso más utilizado es la generación de *condiciones periódicas de contorno.* Se delimita un poliedro de volumen conocido dónde se disponen los átomos que constituyen el sistema estudiado (*caja de simulación*). El entorno del sistema queda definido como un conjunto de imágenes de la caja de simulación, de tal manera que las moléculas de una caja no pueden interaccionar con las de las cajas imagen.

-*Construcción del sistema de partida*: La generación de una estructura amorfa es conceptualmente difícil. Se debe simular un sistema que presenta una distribución irregular de conformaciones estadísticas.
El procedimiento más habitual es utilizar una sola cadena finita de polímero, con muchas unidades repetitivas, y ubicarla en el interior de una caja de simulación. Mediante cálculos estadísticos se conforma el polímero para

que, inicialmente, todos los átomos del sistema estén dentro de la caja, respetando las geometrías de enlace y minimizando los solapamientos entre átomos.

-*Exploración del espacio conformacional*: La solubilidad de un gas se asocia al promedio del comportamiento del gas en el conjunto de microestruturas que describen estadísticamente al material polimérico. Eso implica, de entrada, que el sistema usado para la simulación debe poder representar adecuadamente dicho conjunto. Es decir, es preciso realizar una simulación suficientemente extensa como para que se puedan alcanzar la mayor cantidad posible de microestructuras representativas.

Esta premisa no es una cuestión trivial. La naturaleza de un polímero amorfo, con gran cantidad de restricciones de tipo topológico, hace que la mayoría de los métodos de simulación habituales fallen en la eficiencia de la exploración conformacional requerida (tanto MD como MC-Metrópolis). Una consecuencia de este hecho es que las simulaciones de polímeros amorfos son muy dependientes de la conformación usada como punto de partida. Por este motivo es necesario realizar simulaciones empezando con diferentes conformaciones iniciales, las cuales a su vez deben ser muy largas.

La manera más eficaz de superar este obstáculo metodológico es usar algoritmos de simulación conformacional especialmente adaptados para sistemas densos. En métodos de Monte Carlo el algoritmo más usado para la exploración conformacional en este tipo de sistemas es el método CB.

VIII.2.3. Cálculo del potencial químico mediante el método de inserción de la partícula de prueba

De forma similar a lo comentado anteriormente, este método presenta problemas de eficiencia cuando se afronta el estudio de sistemas densos. Debido a su formulación, insertar partículas de prueba al azar implica una gran dependencia con respecto a la microestructura del disolvente. Cuando éste está constituido por moléculas muy grandes la probabilidad de encontrar puntos del espacio dónde no se solapen las partículas de soluto y los átomos del disolvente se reduce mucho. La mayoría de las inserciones darán energías de interacción muy elevadas con lo que, si no se hace un rastreo muy extenso, el potencial químico en exceso calculado no será representativo. Así, dicho método implicaría un gasto en tiempo de cálculo poco recomendable para sistemas de gran tamaño, como son los polímeros.

Existe una manera de solventar este inconveniente, usando como punto de partida la exploración sistemática del volumen no ocupado existente en el polímero (figura **VIII.2**). Para ello, se analiza el sistema estudiado mediante una división uniforme del espacio. En cada nodo de dicha división se determina si existe espacio suficiente para insertar una partícula de soluto de un tamaño determinado, evaluándose el potencial químico en exceso únicamente en las posiciones libres.

Para poder dar sentido estadístico a este truncamiento del cálculo, se debe promediar el potencial calculado en las posiciones libres por el número de nodos totales en que se divide el espacio analizado.

El formalismo necesario para poder seguir esta estrategia fue desarrollado por Cuthbert et al. (1997), quienes redefinieron el término del colectivo canónico de la ecuación (5) de la siguiente manera:

$$\langle -\exp(\beta\phi_t) \rangle = \sum_{j=1}^{N_e} \left(\frac{1}{N_{Tj}} \right) \sum_{i=1}^{N_{vj}} \exp(\beta\phi_{t,i}) \qquad (6)$$

Definiendo N_e como el número total de microestructuras de polímero que se analizan para el cómputo del potencial químico, N_{vj} como el número de posiciones de inserción dónde no existen solapamientos con los átomos del sistema polimérico para la microestructura j, y N_{Tj} es el número total de posibles puntos de inserción (el número total de nodos en que se divide el espacio estudiado).

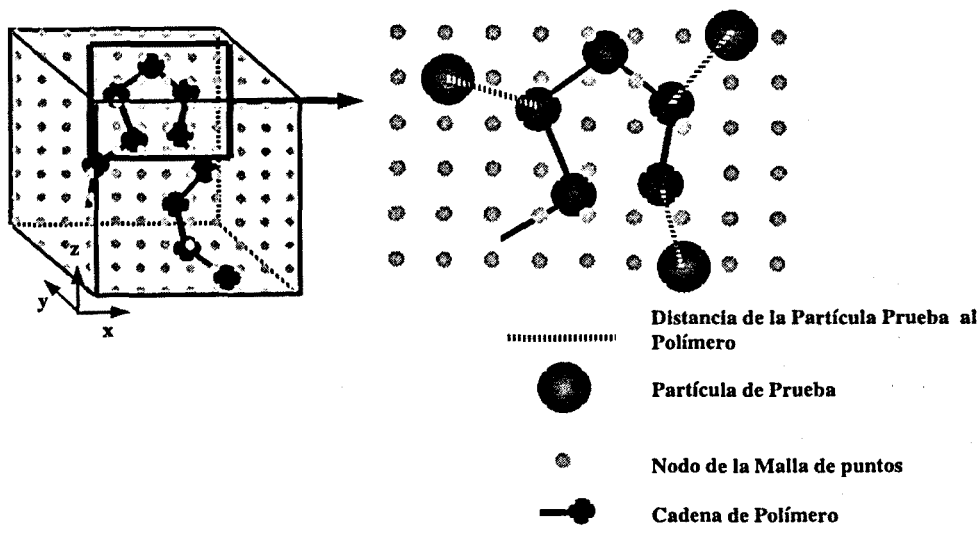

Figura VIII.2. Esquema del protocolo para el análisis del volumen no ocupado. Una vez se divide la caja de simulación en una malla de nodos (puntos amarillos) se inserta una partícula de prueba (bola roja). Si la distancia del centro la partícula a algún átomo de polímero es inferior a la suma de los radios de van der Waals ese nodo se considera ocupado. En aquellos nodos donde todas las posibles distancias sean superiores a dicha suma se evaluara el potencial químico en exceso.

VIII.3. Solubilidad de gases en polímeros cristalinos. La fase cristalina

Hasta el momento la solubilidad de gases en la fase cristalina solo se ha estudiado en el poli(4-metilo-1-penteno) (*PMP*) debido a sus características constitucionales: el PMP presenta una densidad muy parecida para las fases amorfas y cristalinas (Tabla **VIII.1**). Esto se debe a la conformación que adopta dicho polímero en el cristal. Se trata de hélices 7/2 que se empaquetan en una celda tetragonal. Esta estructuración hace que el cristal no sea excesivamente compacto. A su vez, permite cierta libertad de

ordenamiento tanto en el sentido de giro de las hélices como en la orientación relativa de las mismas (Kusanagi et al., 1978).

Tabla VIII.1. Comparación de la densidad de muestras semicristalinas de PMP con la de su fase cristalina (Datos obtenidos por diversos autores). Se observa como la fase cristalina presenta una densidad igual o menor a la de la muestra.

	Densidad (gr cm^{-3})	
Autores	**Muestra**	**Cristal**
Frank et al., 1959	0.847	0.813
Griffith y Ranby, 1960	0.838	0.828
Zoller, 1977	0.835	0.827
Kunsanagi et al., 1978	0.830	0.828

Mediante dos técnicas diferentes Puleo et al. (1989) estudiaron el comportamiento de diferentes gases en la fase cristalina del PMP. Para ello, determinaron la critalinidad de diferentes filmes de polímero mediante DSC y difracción de rayos X. A continuación, estudiaron la solubilidad de dos gases diferentes (dióxido de carbono y metano) en función del tanto por ciento de cristalinidad determinada. La solubilidad de cada uno de los gases presentaba una relación lineal con la cantidad de fase cristalina de las muestras analizadas. Extrapolando el valor que se tendría a cristalinidad 100% se obtuvo el valor de la solubilidad de ambos gases en la fase cristalina (Tabla **VIII.2**).

Tabla VIII.2. Valores extrapolados de la constante de solubilidad del CO_2 y el CH_4 para las fases amorfas y cristalinas del PMP (Puleo et al., 1989).

Solubilidad (cm^3(STP) / cm^3 atm)				
Determinación de la cristalinidad	Fase Amorfa (100%)		Fase Cristralina	
	CO_2	CH_4	CO_2	CH_4
ΔH_f[a]	0.93	0.351	0.28	0.095
Rayos X	0.99	0.378	0.20	0.060

[a] Entalpía de fusión.

De esta forma se pudo ver que en la fase cristalina del PMP podían disolverse gases y que la cantidad de gas disuelto no era proporcional a la densidad del sistema. Es

decir, a pesar de tener ambas fases una densidad muy parecida, la solubilidad de los gases es mucho menor en la fase cristalina que en la amorfa, viéndose que el orden característico de la fase cristalina desfavorecía la absorción de gases pero no la impedía.

Estos resultados nos muestran la influencia de la fase cristalina en la difusión de gases de la mayoría de los polímeros semicristalinos. Así mismo, abren el camino para el estudio de la solubilidad de gases en materiales que presenten diferentes grados de estructuración, en función de su constitución y de las condiciones en que se obtengan.

Además, el estudio de la solubilidad de gases en polímeros cristalinos constituye un reto desde un punto de vista metodológico. Así, simular una estructura cristalina es más complejo que una estructura amorfa, puesto que no existen algoritmos adecuados para realizar una exploración eficiente del espacio conformacional, si bien hay que tener en cuenta que el número de grados de libertad es inferior al de un sistema amorfo.

VIII.4. Objetivos:

El objetivo general de este capítulo es estudiar la solubilidad de gases ligeros en diferentes matrices poliméricas constituidas por cadenas ordenadas. Para poder alcanzar este objetivo nos planteamos resolver los siguientes aspectos:

1) Obtención de una metodología eficiente para el cálculo de la solubilidad de gases en polímeros cristalinos basada en simulaciones de MC.

2) Evaluación de la capacidad de predicción de dicha metodología mediante la comparación con datos experimentales de la solubilidad de gases en polímeros cristalinos.

3) Cálculo de la solubilidad de gases en sistemas poliméricos con diferente tipo de estructuración. Efecto del tipo de estructura cristalina: estructuras ordenadas tridimensionalmente y estructuras bifásicas.

VIII.5. "Crystalline Poly(4-methyl-1-pentene): Structure and Solubility of Gas Molecules"

Zanuy D.; Alemán C.; Muñoz-Guerra, S. *J. Polym. Science Physics Ed.*

(Enviado, noviembre 2000)

Crystalline Poly(4-methyl-1-pentene): Structure and Solubility of Gas Molecules

David Zanuy, Carlos Alemán* and Sebastián Muñoz-Guerra

Departament d'Enginyeria Química, E.T.S. d'Enginyers Industrials de Barcelona, Universitat Politècnica de Catalunya, Diagonal 647, Barcelona E-08028, Spain

* Corresponding author: aleman@eq.upc.es

ABSTRACT

Monte Carlo (MC) simulations have been used to study the crystal structure of isotactic poly(4-methyl-1-pentene). Four different tetragonal packing modes, each one containing two right-handed and two left-handed 7/2 helices, have been considered in order to investigate the up-and-down chain statistical disorder proposed on the basis of X-ray data. Simulations have been performed using the isotropic united atom parametrization of the Amber force-field. The influence on the more stable packing modes of the force-field parametrization has been investigated by considering both the anisotropic united atom and all atom models. Results reveal that packing constituted by two upward and two downward helices arranged at random is more stable than those with three or four helices with the same sense. Furthermore, the fiber period length for the 7/2 helix is predicted to be 0.56 Å larger than that experimentally determined. The microstructures generated from MC simulations have been employed to study the solubility of gas molecules (He, H_2, Ar, O_2, CH_4 and CO_2) using the Widom's test-particle insertion method. A special attention has been given to the solubility of CH_4 and CO_2 since experimental data are available for these penetrants, the latter being described by both spherical and explicit models. Results are in good agreement with experimental measures only when a suitable model is used for the penetrant. The solubility of gas molecules in crystalline poly(4-methyl-1-pentene) has been correlated with that measured for the crystal phase of other helical polymers.

INTRODUCTION

Solubility of gas molecules (so-called penetrants) in polymeric matrices is an important topic in the field of polymer science and technology [1]. The application of atomistic simulations to study the solubility of penetrants in dense polymers has become computationally tractable in recent years due to the availability of more powerful computers and more efficient simulation algorithms. These simulations are able to provide information about the polymer and the penetrant that is not accessible from experimental data.

Computational studies usually involve the solubility of gas molecules in amorphous host polymers. This is because the mobility of the penetrant is much higher in the amorphous phase than in the crystalline phase since the packing of the chains is much less efficient in the former state. Accordingly, it has been traditionally accepted that the transport of gases in a semicrystalline polymer takes place mainly through the amorphous phase, a fact that has been recently confirmed [2]. However, recent theoretical and experimental studies have revealed that some polymers present an exceptional behavior since high solubilities have been measured for both the ordered and disordered phases [3,4]. In a very recent study we found that the solubility of small penetrants in the phase A of comblike poly(α-alkyl-β,L-aspartate)s, *i.e.* a family of polyamides bearing long alkyl side chains crystallized in a separated paraffinic phase, is more favorable than in the phase B [4]. This is because the former phase has a lower density than the latter [5]. Even although phase B is less ordered than phase A, the unoccupied space is larger in the latter allowing a more favorable interaction between the penetrant and the polymeric matrix. Conversely, poor gas solubilities were obtained for crystalline poly(α-alkyl-β,L-aspartate)s with short alkyl side chains due to the efficient packing of the chains [6].

Another polymer with exceptional properties is isotactic poly(4-methyl-1-pentene), abbreviated PMP, since it presents similar solubilities and permeabilities for the amorphous and crystalline regions [3]. This finding is supported by the fact that the crystalline and amorphous densities in PMP are very similar and, therefore, the two phases should have a nearly equal amount of unoccupied space. The crystal structure of PMP was determined by Tadokoro and coworkers [7]. It consists of four 7/2 helices, two right-handed and two left-handed, packed in a tetragonal unit cell (Figure 1). Although there is some ambiguity regarding the sense of the helices, the authors proposed a statistical disorder of upward and downward helices as the most probable.

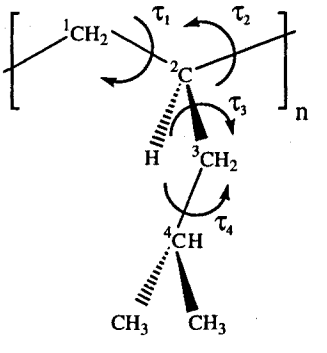

PMP

The diffusion of CO_2 and CH_4 in crystalline PMP was investigated by Müller-Plathe using atomistic molecular dynamics simulations [8]. In such study the author considered a parallel packing of right- and left-handed helices rather than a statistical structure of upward and downward helices, like that proposed by Tadokoro and coworkers [7]. However, the results nicely provided a good explanation of the behavior of the penetrants in

crystalline PMP and the unusually low barrier to gas diffusion displayed by this polymer.

In the present work we have used Monte Carlo (MC) simulations to re-examine the solubility of a number of gas penetrants in the crystal phase of PMP. In order to provide an appropriate description of the statistical structure of isotactic PMP, calculations have been performed considering the four different packings of 7/2 helices. These packings have been used to measure the volume not occupied by the atoms of the polymer, *i.e.* the unoccupied space, which allows to predict the behavior of the system against small penetrants. The solubility has been explicitly computed using the Widom's test particle insertion method [9]. A special attention has been given to the solubility of CO_2 and CH_4 penetrants since experimental data are available. The influence in the prediction of solubilities and permeabilities of the force-field used to describe the system has been a topic of controversy during the last years [10-15]. In order to evaluate this influence in crystalline PMP, unoccupied space and solubilities were estimated using isotropic united-atom (IUA), anisotropic united-atom (AUA) and all-atom (AA) force-fields, and results were compared with experimental data [3].

METHODS

Structure. The structure of crystalline PMP was investigated using an advanced Monte Carlo sampling technique called Configurational Bias, and denoted CB-MC. This method was initially implemented for the off-lattice treatment of dense polymers at the beginning of the last decade [16-18]. The CB-MC algorithm consists of the three steps: *i)* a chain is selected at

random; *ii)* the chain is cut at a random position; and *iii)* the chain is sequentially re-grown. The chain is re-grown bond-by-bond by examining a number of possible positions (N_S) which can be chosen either randomly, or in a biased-way depending on the torsional potentials associated to the bond. The weight of the re-grown part of the chain corresponds to the product of the weights of the re-grown bonds, which in turn are proportional to its normalized Boltzmann factor. In order to ensure the condition of microscopic reversibility an appropriate transition probability is chosen [16-18].

In a very recent work, a strategy to simulate polymeric systems with ordered structures was developed and implemented in the MCDP (Monte Carlo for Dense Polymers) computer program [19]. This strategy combines simple and advanced MC methods like Metropolis [20] and CB, respectively. Thus, CB-MC was adapted for studying systems with flexible alkyl side chains attached to a core with a shape defined by the main chain conformation [19]. The reliability of this strategy was recently proved by studying the structure of different ordered polymers with flexible side groups [19,21]. In the present study all the MC simulations were performed with the MCDP program. The Metropolis algorithm was used to vary the conformation of the main chain, the cell parameters and the relative orientation between the helices, *i.e.* the setting angle, whereas the configurational space of the alkyl side groups was explored using the CB-MC algorithm.

The boxes used in the simulations of PMP consist of four explicit chains of 7 residues. Periodic boundary conditions and the minimum image convention were applied in all the calculations. MC simulations of $2 \cdot 10^6$ steps of both *NVT* and *NPT* type, *i.e.* with and without varying the size of the box, respectively, were performed at T = 298 K. In addition to CB

moves, a small fraction (20%) of Metropolis moves were also used for the side chains. CB moves were done considering N_S=6. For each simulation 100 microstructures were recorded and analyzed at $2 \cdot 10^4$ steps.

The model used in MCDP calculations assumed fixed bond lengths and angles. Accordingly, the torsional angles were the only geometric parameters of the chain to be moved. The torsional energy was computed using the classical 3-term Fourier expression, the torsional parameters being listed in Table 1. The van der Waals energy was computed in the usual additive way using a Lennard-Jones 6-12 potential. The IUA parametrization of the AMBER force-field [22,23] (Table 1), denoted AMBER/IUA, has been used to evaluate the van der Waals energy. It should be mentioned that the AMBER/IUA force-field has been successfully used to predict the crystal structure of polymers bearing alkyl side chains [6,21]. Lennard-Jones potentials were truncated at 10 Å.

The starting geometry for the crystal structure of PMP was built using the information previously reported by Tadokoro and coworkers [7]. Thus, the 7/2 helix was constructed using the conformational parameters: τ_1= 165.1°, τ_2= -72.8°, τ_3= 180.0° and τ_4= 48°. The helices were placed in a tetragonal box with parameters a = 18.70 Å and c (helix axis)= 13.68 Å, which correspond to the cell parameters obtained from X-ray diffraction, at the positions indicated in Figure 1. All the possible packing modes that can be generated by varying the sense of the helices were built and examined through MC simulations to simulate the statistical structure. The more favored packing modes resulting from these calculations were used to investigate the effects of the force-field on the structural parameters of PMP. Thus, additional MC simulations of *NPT* type were performed using more

sophisticated parametrizations of the AMBER force-field: the AMBER/AUA [22,23] and the AMBER/AA [23] (Table 1).

Measurement of the Unoccupied Space. Unoccupied space estimation was done by dividing the simulation box of every microstructure into a three-dimensional uniformly spaced grid. Then, a penetrant was centered in each node and the distance to the nearest atom of the polymeric matrix was measured. If this distance was larger than the sum of the van der Waals radii of the penetrant and the polymer atom, the node was identified as unoccupied. Calculations were performed considering spacings between consecutive nodes of 0.75, 0.50 and 0.25 Å. A set of six penetrants was chosen: He, H_2, Ar, O_2, CH_4 and CO_2. The van der Waals radii used for the penetrants, which were initially described as simple spheres, are displayed in Table 2.

Solubility. The solubility (S) of a given penetrant in a polymeric matrix is related with the excess chemical potential (μ^{ex}) by Equation 1:

$$S = \exp(\mu^{ex}/RT) \qquad (1)$$

The infinite-dilution μ^{ex} of a penetrant sorbed in crystalline PMP was estimated using the Widom's test particle insertion method [9]. In this method the chemical potential of species *i* in a frozen N-particle system relative to an ideal gas mixture is related to the potential energy of inserting a test-particle into the system at randomly chosen positions. The expression of μ^{ex} is:

$$\beta \mu^{ex}(\rho,T) = -\ln \langle \exp(-\beta\phi_t) \rangle_N \qquad (2)$$

where $\beta=1/k_BT$, ϕ_t is the interaction energy between the test particle and the N particles of the system, and $\mu^{ex}(\rho,T)$ is the excess of chemical potential of species *i* at temperature T and number density $\rho=N/V$. The brackets $<...>_N$ denote the canonical ensemble average over the original N-particle system at the T and ρ of interest.

In order to evaluate μ^{ex} (equation 2), we have divided the simulation box of each microstructure into uniformly spaced grids. A penetrant was centered in each node if it was identified as unoccupied. Calculations were performed considering different spacings between consecutive nodes: 0.75, 0.50 and 0.25 Å. Interactions between the penetrants and the polymer were computed using the Lennard-Jones 6-12 potential and applying the Lorenz-Bethelot mixing rules. Such interactions were truncated at 10 Å. The force-field parameters for the different penetrants considered in this study are displayed in Table 2.

All the calculations were performed on a Silicon Graphics Indigo (SGI-R10000) at our laboratory and at the IBM-SP2 at the Centre de Supercomputació de Catalunya (CESCA).

RESULTS AND DISCUSSION

Structural Search. The arrangement of the molecular chains in the crystal structure of PMP has been investigated using MC simulations. For this purpose, the tetragonal unit cell displayed in Figure 1 was filled with left-handed (L) helices at positions 1 and 4, and right-handed (R) helices at

positions 2 and 3. For this crystal arrangement, all the possible combinations of upward (u) and downward (d) helices were considered. A total of 4 different packing models, which are listed in Table 3, were generated. It should be noted that due to both the isotactic nature of the polymer and the tetragonal symmetry of the cell, the remaining packing modes are equivalent and isoenergetic to those given in Table 3.

Two MC simulations using the AMBER/IUA force-field were performed for each packing mode. In the first simulation (MC-1), which was of *NVT* type, the degrees of freedom were the setting angle of the chains and both the backbone and side chain dihedral angles. In the second one (MC-2), the length of the fiber period was also allowed to vary throughout the simulation but retaining the 7/2 helix symmetry. The relative energies obtained from the two simulations for all the packing modes are displayed in Table 3. In all cases, the energy of the system was equilibrated rapidly, *i.e.* in less than $2 \cdot 10^4$ steps. Additionally, block analyses indicate that the structures generated are almost completely decorrelated after a few cycles of moves.

As can be seen, the results provided by MC-1 and MC-2 are very consistent. Thus, in both cases the most stable packing corresponds to pairs of upward and downward helices with different handedness (model **a**). The model **b**, which corresponds to a packing of pairs of upward and downward helices with the same handedness, is destabilized by only 0.8 kcal/mol·residue with respect to model **a**. On the other hand, the models containing either three or four helices with the same sense, *i.e.* models **c** and **d** respectively, are clearly unfavored with respect to the packings constituted by pairs of upward and downward helices. Figure 2 shows a typical configuration for the model **a** of PMP at the end of the MC-2 simulation.

Analysis of the packing modes resulting from MC-2 simulation reveals the same variation of the fiber period length for all of them. Thus, this parameter systematically evolves from 13.68 Å (experimental value) to 14.24 Å, the calculated density varying from 0.82 g/cm^3 to 0.79 g/cm^3. It is worth noting that the latter value is also consistent with the experimental value observed for semicrystalline PMP (0.83 g/cm^3) [7].

The results provided from MC-1 and MC-2 simulations are in good agreement with the structure proposed by Tadokoro and co-workers from X-ray diffraction data [7]. These authors found that the crystal structure of PMP has a statistical disorder with respect to the upward and downward senses of the helices. This molecular disorder is clearly reproduced by the low energy differences obtained for models **a** and **b** from MC simulations. According to these results, a disordered structure constituted by upward and downward helices with a ratio 1:1 is proposed as the most probable for the crystal structure of isotactic PMP.

Effect of the Force-Field on the Structure of PMP. Additional MC simulations of models **a** and **b** were performed using the AMBER/AUA and AMBER/AA force-fields. The setting angle of the chains, the backbone and side chain dihedral angles and the axial repeat length were considered as degrees of freedom. Results have been compared with those obtained using the AMBER/IUA force-field.

As a first step of MC data evaluation, we examined the conformational parameters τ_1, τ_2, τ_3 and τ_4. The results obtained from the different simulations of model **a** are summarized in Table 4, which displays the torsional angles averaged over 100 microstructures as well as the values

obtained by Tadokoro and co-workers [7] from X-ray data refinement. It is worth noting that the backbone dihedral angles τ_1 and τ_2 provided by the three force-fields are almost identical, the largest difference being 0.5°. Furthermore, the standard deviations of the averages are very small, *i.e.* less than 3.3°, pointing out the stiffness of the 7/2 helix. Almost identical values and standard deviations have been obtained from the simulations of model **b**. The values of τ_1 and τ_2 predicted by MC simulations differ from those reported by Tadokoro and co-workers [8] in about 5° and 15°, respectively. This small discrepancy is due to the difference between theoretical and experimental fiber period lengths. Thus, the value reached from MC simulations is 14.24 Å for the three force-fields, which is the 0.56 Å larger than that determined from the X-ray diagram.

On the other hand, the three force-fields also predict a similar side chain conformation, the differences in τ_3 and τ_4 being lower than 4°. Another interesting point concerns to the standard deviations of τ_3 and τ_4 which are related with the degree of mobility of the side group. The standard deviations of the side chain dihedral angles, in particular those of τ_4, indicate a considerable conformational flexibility. This is due to the fact that the side chain conformations of the four helices have been averaged in Table 4 since we are trying to provide a plain picture of the structure. Obviously, this is physically unreasonable for a packing constituted by pairs of upward and downward helices with a 7/2 symmetry and different handedness. Thus, the packing environment fluctuates within the cell, and in consequence the side chain conformation should change according to its position within the cell. It should be mentioned that the most populated conformations are the *gauche*$^+$ (right-handed helices) and *trans* (left-handed helices) ones.

The variation of the setting angle through the three MC simulations of model **a** is displayed in Figure 3. It is worth noting that in all cases the setting angle is equilibrated after a few steps of simulation. The values provided by the AMBER/IUA and AMBER/AUA force-fields are very similar, being around 60°. On the other hand, the setting angle predicted by the AMBER/AA force-field is about 75°. Similar values and variations were found model **b** (data not shown). In summary, the influence of the force-field in the structure of PMP is not significant as can be concluded from the small differences observed in both conformational and setting angles.

Measurement of th e Unoccupied Space. Before to estimate the solubility of CH_4 and CO_2 penetrants in crystalline PMP, we examined the unoccupied space of penetrants with different sizes for all the generated microstructures. The results are summarized for each penetrant in Table 5, which displays the amount of unoccupied space averaged over the 100 microstructures recorded from the AMBER/IUA simulations of models **a-d**. In all cases the unoccupied space was estimated considering three different grid spacings: 0.75, 0.50 and 0.25 Å.

The small standard deviations of the averages displayed in Table 5 (data not shown) indicate that all the microstructures generated for a given model present a similar unoccupied space. This trend suggests that the number of microstructures generated is suitable for the present study. Furthermore, results reveal that for a given penetrant, grid spacings finer than 0.75 Å displayed no significant changes in the resulting unoccupied space. On the other hand, the amount of unoccupied space depends on the packing mode. Thus, for all the penetrants considered in this study the measured unoccupied spaced for the models increases according to **a** < **b** < **c** < **d**. Thus, there is a clear correlation between the stability of the models and the

amount of unoccupied space. The models mainly constituted by helices of the same sense are the least stable and present the lowest packing efficiency.

An analysis of the results obtained for the different penetrants reveals some important features. As can be seen the unoccupied space decreases when the size of the penetrant increases. These results further indicate that a considerable number of He atoms are able to fit within crystalline PMP, whereas the space available for penetrants like CH_4 is very small. The small amount of volume accessible to the CH_4 is consistent with the low solubility coefficient determined for this penetrant in crystalline PMP [3]. The most striking result is that the unoccupied space predicted for the CO_2 penetrant is zero in clear disagreement with experimental data [3].

The poor results obtained for the CO_2 penetrant should be attributed to a bad choice of the model used to describe this gas molecule. Thus, CO_2 was modeled using a Lennard-Jones sphere as proposed Cuthbert *et al.* [24] for studying the solubility of such penetrant in amorphous polystyrene. These authors chose such model on the basis of experimental solubility data, which shows a linear correlation of the logarithm of the Henry´s law constant with the Lennard-Jones well depth [25]. However, crystalline and glassy polymers display a different structural behavior suggesting that models suitable for the latters can lead to erroneous results when applied to the formers.

In order to improve our results with the CO_2 penetrant, the spherical description discussed above was changed by a more accurate model with explicit C and O atoms. The parameters for explicit CO_2 are given in Table 6. A re-examination of the unoccupied space was performed using this new model, the results being included in Table 5. As can be seen, in this case

the results strongly depend on the grid spacing. Thus, the amount of unoccupied space increases each time that the grid spacing decreases 0.25 Å. It is worth noting that the unoccupied space predicted for explicit CO_2 is about 3 times larger than that obtained for CH_4 when a grid spacing of 0.25 Å. This is in excellent agreement with experimental data since the solubility of CO_2 in crystalline PMP was observed to be about 3 times larger than that of CH_4.

Table 7 compares the amount of unoccupied space averaged for the 100 microstructures recorded from the AMBER/IUA, AMBER/AUA and AMBER/AA simulations of model **a**. It is worth noting that the unoccupied space varies for a given penetrant when the force-field used to describe crystalline PMP changes. Thus, it decreases when all the atoms are explicitly included in the force-field. The unoccupied space predicted for He penetrant by the AUA and AA force-fields is about 10 % and 93%, respectively, smaller than that provided by the IUA force-field. A detailed comparison of the unoccupied spaces provided for models **a** and **b** (data not shown) indicates that the differences between the AMBER/IUA and AMBER/AUA simulations are quite small. However, such differences are dramatic when the results provided by the AMBER/IUA and AMBER/AA simulations are compared. Moreover, the unoccupied space predicted by the AMBER/AA force-field is zero for penetrants bigger than H_2. Thus, no cavity of sufficient size to accommodate such penetrants is formed when all the atoms are explicitly included in the force-field.

The deficiency of the AA force-field is probably due to the parametrization of AMBER, which was initially designed to simulate the structure and dynamics of proteins [22,23]. For the last years it has been shown that the AMBER/AA force-field is able to describe the structure of synthetic

polymers containing both backbone amide groups and paraffin side chains [26,27]. However, the van der Waals parameters (radius and depth) are too large to provide reliable results when a complex process like the solubility of small penetrants in an ordered polymeric matrix is simulated.

Solubilities. The simulated solubilities derived for the four models of PMP by applying equations 1 and 2 to the microstructures generated from AMBER/IUA simulation are displayed in Table 8. Calculations for CO_2 were performed with the explicit model discussed above. The effect of the grid spacing in the solubility of spherical penetrants is very small. Thus, the largest variation between the solubilities predicted by the different grid spacings is about 4% and 13% for He and O_2 penetrants, respectively. Conversely, the grid spacing drastically affects the solubility of CO_2, the values predicted for a grid spacing of 0.25 Å being even several times larger than those obtained considering a spacing of 0.75 Å. On the other hand, the solubilities predicted for the four models are very different. These trends are fully consistent with the variations observed for the unoccupied space in the previous sections.

The most remarkable result of this section concerns to the solubility of CH_4 and CO_2 in crystalline PMP. The experimental solubility coefficients [CH_4: 0.095-0.060 cm^3 (SPT)/cm^3 atm; CO_2: 0.28-0.20 cm^3 (STP)/cm^3 atm] indicate that CO_2 is about three times more soluble than CH_4. In order to estimate the solubility of CH_4 and CO_2 in a statistical lattice of crystalline PMP, the μ^{ex} values obtained for the four models considered in this work were averaged according to a Boltzmann distribution. Thus, they were weighted with respect to the most stable model (Table 3). The resulting chemical potentials were employed to estimated the solubilities of the statistical lattice applying equation 1. Results are displayed in Table 9.

Calculations predict that CO_2 is about 5 times more soluble than CH_4 when a grid spacing of 0.25 Å is considered. However, such difference decreases to about 3 when the grid spacing increases from 0.25 to 0.50 Å, and the solubilities of the two penetrants become almost identical for 0.75 Å.

The unoccupied space concept has been widely invoked in interpreting the solubility of spherical penetrants. From previous simulation results on helical poly(α-alkyl-β-L-aspartate)s, denoted PAALA-*n* (where *n* is the number of carbon atoms involved in the alkyl side chain), it was found that the solubility of spherical penetrants correlates well with the measured unoccupied space. It is of interest if such a correlation extends to the polymer studied here. The fractional unoccupied space accessible to a penetrant of radius, *R*, inserted in the polymer is represented in Figure 4 for crystalline PMP and compared to those obtained for PAALA-1, PAALA-4, PAALA-12, PAALA-14 and PAALA-16. The intercept at *R=0* of a curve in Figure 4, is the total unoccupied space in that polymer. The latter quantity has been used for correlation with the predicted solubilities. Figure 5 displays the correlation of the total unoccupied space with the solubility for He, Ar and CH_4 penetrants, which were those investigated for poly(α-alkyl-β-L-aspartate)s.

It is worth noting that PMP appears to fall on the same correlation line than PAALA-1 and PAALA-4. These polymers adopt right-handed 17/4 and 13/4-helices, respectively, that pack in a hexagonal lattice, whereas PMP consists of a tetragonal packing of 7/2 helices. However, poly(α-alkyl-β-L-aspartate)s bearing short alkyl side groups and PMP follow a similar behavior that seems to be common to crystalline polymers with three-dimensional order. It is very apparent, however, that PAALA-n with *n*= 12,

14 and 16 fall far off such correlation. These polymers organize in lamellar structures lacking three-dimensional order. Thus, these are comb-like polymers with the helices arranged side-by-side in layers and the side chains, which are in a molten state, located in a separated phase. According to the present results, it can be concluded that solubility of crystalline polymers mainly depends on the degree of ordering achieved in the crystal rather than on the helix conformation and the packing mode.

CONCLUSIONS

We have performed a systematic CB-MC study of the crystal structure of isotactic PMP. Four packings modes, which differ among them in the number and distribution of upward and downward helices, have been considered in order to investigate the statistical arrangements proposed by Tadokoro and co-workers on the basis of X-ray diffraction data [7]. Our results indicate that the structure of PMP contains upward and downward helices with a ratio of 1:1 since the packings with a higher ratio of upward helices are considerably less stable. Furthermore, simulations indicated that the fiber period length is about 4% larger than that experimentally measured.

The amount of unoccupied space and the solubility of gas penetrants (He, H_2, Ar, O_2, CH_4 and CO_2) were estimated considering the microstructures generated by MC simulations. Results indicate that the unoccupied space decreases when the size of the penetrant increases. Moreover, calculations reveal that the Lennard-Jones sphere model provide good results for all the penetrants except for CO_2. This model, which is commonly used to simulate the solubility of CO_2 in amorphous polymers, fails when it is applied to

crystal polymers. However, a good agreement with experimental data is obtained when an explicit model is used to describe CO_2. Thus, our calculations predict that the solubility of CO_2 in crystal PMP is several times larger than that of CH_4.

On the other hand, simulations for the more stable models have been performed using the AMBER/IUA, AMBER/AUA and AMBER/AA force-fields. Results indicate that the two force-fields with an united atom approximation are able to capture the most important trends of this polymeric system. These are: the rigidity of the backbone conformation, the mobility of the alkyl side groups and the presence of unoccupied space compatible with measured solubilities. Conversely, the unoccupied space predicted by the AMBER/AA is zero, which is in contradiction with the experimental data.

ACKNOWLEDGEMENTS

This work was supported by DGICYT with grant No. PB96-0490. D.Z. acknowledges the support of the Ministry of Education of Spain for the award of a scholarship. We are indebted to CESCA for computational facilities.

REFERENCES

1. Gusev A.A.; Müller-Plathe F.; van Gunsteren W.F.; Suter U.W. Adv. Polym. Sci. 1994, 116, 207.

2. Müller-Plathe F. Acta Polym. 1994, 45, 259.

3. Puleo A.C.; Paul D.R.; Wong P.K. Polymer 1989, 30, 1357.

4. Zanuy D.; Namba, A.M.; León S.; Alemán C.; Muñoz-Guerra S. Polymer 2001, 42, 281.

5. López-Carrasquero F.; Montserrat S.; Martínez de Ilarduya A.; Muñoz-Guerra S. Macromolecules 1995, 28, 5535.

6. Zanuy D.; León S.; Alemán C.; Muñoz-Guerra S. Polymer 2000, 41, 4169.

7. Kusanagi H.; Takase M.; Chatani Y.; Tadokoro H. J. Polym. Sci.: Polym. Phys. Ed.
1979, 16, 131.

8. Müller-Plathe F. J. Chem. Phys. 1995, 103, 4346.

9. Widom B. J. Phys. Chem. 1982, 86, 869.

10. Müller-Plate F.; Rogers S.C.; van Gunsteren W.F. Macromolecules 1992, 25, 6722.

11. Kant P.V.F; Boyd R.H. Macromolecules 1992, 25, 494.

12. Müller-Plate F.; Rogers S.C.; van Gunsteren W.F. Macromolecules 1993, 98, 9895.

13. Bharadwaj R.K.; Boyd R.H. Polymer 1999, 40, 4229.

14. Greenfield M.L.; Theodorou D.N. Macromolecules 1998, 31, 7068.

15. Hedenqvist, M.S.; Bharadwaj, R.; Boyd, R.H. Macromolecules 1998, 31, 1556.

16. Leontidis E.; Forrest B.; Widmann A.H.; Suter U.W. J. Chem. Soc. Faraday Trans. 1995, 91, 2355.

17. de Pablo J.J.; Laso M.; Suter U.W. J. Chem. Phys. 1992, 96, 2395.

18. Siepmann J.I.; Frenkel D. Mol. Phys. 1992, 75, 59.

19. León S.; Alemán C.; Escalé F.; Laso M. J. Comput. Chem. 2000, in press.

20. Metropolis N.; Rosenbluth A.W.; Rosenbluth M.N.; Teller A.H. J. Chem. Phys. 1953, 21, 1087.

21. León S.; Alemán C.; Laso M.; Muñoz-Guerra S. *Comput. Theor. Polym. Sci.* **2000**, *10*, 177.

22. Weiner S.J.; Kollman P.A.; Case D.A.; Singh U.C.; Ghio C.; Alagona G.; Profeta S.; Weiner P. J. Am. Chem. Soc. 1984, 106, 765.

23. Cornell W.D.; Cieplak P.; Bayly C.I.; Gould I.R.; Merz K.M.; Ferguson D.M.; Spellmeyer D.C.; Fox T.; Caldwell J.W.; Kollman P.A. J. Am. Chem. Soc. 1995, 117, 5179.

24. Cuthbert, T. R.; Wagner; N. J.; Paulaitis M. E. Macromolecules 1997, 30, 3058.

25. Veith, W.R.; Tam, P. M.; Michael, A. S. J. Colloid Interface Sci. 1966, 22, 360.

26. Navas, J.J.; Alemán, C.; López-Carrasquero, F.; Muñoz-Guerra, S. Macromolecules 1995, 28, 4487.

27. Navas, J.J.; Alemán, C.; López-Carrasquero, F.; Muñoz-Guerra, Polymer 1997,38, 3477.

28. Zanuy, D.; Alemán, C.; López-Carrasquero, F.; Báez, M.E.; García-Alvarez, M.; Laso, M.; Muñoz-Guerra, S. Macromol. Chem. Phys. 2000, in press.

Table 1. Force-field parameters for PMP

Torsional parameters

Torsional angle	$V_n/2$ (kcal/mol)	n	γ
-C^1-C^2-	1.3	3	0
-C^2-C^3-	1.3	3	0
-C^3-C^4-	2.0	3	0

Lennard-Jones parameters

Force-Field	Atom	R (Å)	ε (kcal/mol)
IUA[a]	United CH	1.85	0.090
	United CH_2	1.92	0.120
	United CH_3	2.00	0.150
AUA[b]	Carbon	1.80	0.060
	Hydrogen	1.54	0.010
	United CH_2	1.92	0.120
	United CH_3	2.00	0.150
AA[c]	Carbon	1.908	0.1094
	Hydrogen	1.487	0.0157

[a] Isotropic United Atom parametrization.

[b] Anisotropic United Atom parametrization.

[c] All Atom parametrization

Table 2. Lennard-Jones potential parameters for the penetrants.

Penetrant	R (Å)	ε (kcal/mol)
He	1.290	0.0203
H_2	1.475	0.0734
Ar	1.725	0.2379
O_2	1.790	0.2333
CH_4	1.909	0.2943
CO_2 (spherical model)	2.243	0.3754

Table 3. Relative energies[a] obtained from Monte Carlo simulations[b] for the packing modes[c] of PMP.

#	1	2	3	4	ΔE (MC-1)	ΔE(MC-2)
a	Lu	Rd	Ru	Ld	0.0	0.0
b	Lu	Rd	Rd	Lu	0.6	0.8
c	Lu	Ru	Ru	Ld	1.8	1.5
d	Lu	Ru	Ru	Lu	1.9	1.7

[a] In units of kcal/mol·residue.

[b] MC-1 refers to Monte Carlo simulations with the IUA parametrization varying the setting angle, the backbone dihedral angles and the side chain dihedral angles. MC-2 refers to Monte Carlo simulations with the IUA parametrization varying the setting angle, the backbone dihedral angles, the side chain dihedral angles and the fiber period.

[c] The positions 1, 2, 3 and 4 correspond to those displayed in Figure 1. R, L, u and d refer to righ-handed, left-handed, upward and downward, respectively.

Table 4. Average dihedral angles[a] and standard deviations[a] for the 7/2 helix of PMP obtained from Monte Carlo simulations for the packing mode a[b]. The values obtained from the refinement against the X-ray data are also displayed[c].

Force-Field	τ_1	τ_2	τ_3	τ_4
AMBER/IUA	-77.1±0.1	179.9±0.1	178.9±14.1	119.3±51.7
AMBER/AUA	-77.1±0.1	179.9±0.1	179.3±19.5	116.6±45.7
AMBER/AA	-77.0±0.9	179.4±3.3	-178.8±13.1	120.6±45.3
X-ray refinement[c]	-72	165	147	154

[a] In degrees.

[b] See Table 3.

[c] From reference 7.

Table 5. Fraction of predicted unoccupied space[a] (V_{us}; in %) for the different penetrants in the four models of crystalline PMP. V_{us} was measured for the microstructures generated from AMBER/IUA simulations considering spacings between consecutive nodes of 0.75 (top), 0.50 (middle) and 0.25 (bottom) Å.

Penetrant	model a	model b	model c	model d
	1.23	2.53	2.83	3.03
He (R=1.290 Å)	1.23	2.49	2.81	3.07
	1.26	2.56	2.90	3.16
	0.47	1.22	1.48	1.68
H_2 (R=1.475 Å)	0.48	1.21	1.49	1.67
	0.49	1.22	1.52	1.73
	0.07	0.29	0.44	0.52
Ar (R=1.725 Å)	0.07	0.29	0.42	0.52
	0.07	0.28	0.44	0.54
	0.02	0.14	0.24	0.30
O_2 (R=1.790 Å)	0.02	0.14	0.24	0.31
	0.03	0.14	0.24	0.31
	0.01	0.05	0.10	0.14
CH_4 (R=1.909 Å)	0.01	0.05	0.10	0.14
	0.01	0.05	0.10	0.14
	0.00	0.00	0.00	0.00
CO_2 (R=2.243 Å)	0.00	0.00	0.00	0.00
(spherical model)	0.00	0.00	0.00	0.00
	0.01	0.03	0.13	0.20
CO_2	0.02	0.05	0.22	0.26
(explicit model[b])	0.06	0.17	0.35	0.40

[a] Averaged over the 100 microstructures generated by MC simulations.

[b] Force-field parameters for explicit CO_2 are displayed in Table 6 (see text).

Table 6. Force-field parameters for explicit CO_2.

Atom	R (Å)	ε (kcal/mol)
C	1.850	0.120
O	1.60	0.200

Table 7. Fraction of predicted unoccupied space[a] (V_{us}; in %) for the different penetrants in the model **a** of crystalline PMP. V_{us} was measured for the microstructures generated from AMBER/IUA, AMBER/AUA and AMBER/IUA simulations considering spacings between consecutive nodes of 0.75 (top), 0.50 (middle) and 0.25 (bottom) Å

Penetrant	AMBER/IUA	AMBER/AUA	AMBER/AA
	1.23	1.13	0.35
He (R=1.30 Å)	1.23	1.12	0.38
	1.26	1.15	0.39
	0.47	0.42	0.08
H_2 (R=1.46 Å)	0.48	0.43	0.08
	0.49	0.44	0.08
	0.07	0.06	0.00
Ar (R=1.70 Å)	0.07	0.06	0.00
	0.07	0.06	0.00
	0.02	0.02	0.00
O_2 (R=1.79 Å)	0.02	0.02	0.00
	0.03	0.02	0.00
	0.01	0.00	0.00
CH_4 (R=1.90 Å)	0.01	0.00	0.00
	0.01	0.00	0.00
	0.00	0.00	0.00
CO_2 (R=2.24 Å)	0.00	0.00	0.00
(spherical model)	0.00	0.00	0.00
	0.01	0.00	0.00
CO_2	0.02	0.00	0.00
(explicit model[b])	0.06	0.02	0.00

[a] Averaged over the 100 microstructures generated by MC simulations.

[b] Force-field parameters for explicit CO_2 are displayed in Table 6 (see text).

Table 8. Solubilities predicted for crystalline PMP. Solubilities were measured for the microstructures generated from AMBER/IUA simulations considering spacings between consecutive nodes of 0.75 (top), 0.50 (middle) and 0.25 (bottom) Å.

Penetrant	model a	model b	model c	model d
	2.07	4.28	4.78	5.13
He	2.07	4.21	4.75	5.18
	2.13	4.33	4.90	5.34
	0.81	2.07	2.52	2.87
H_2	0.81	2.06	2.53	2.85
	0.83	2.08	2.59	2.94
	0.13	0.50	0.76	0.90
Ar	0.13	0.49	0.74	0.91
	0.13	0.48	0.76	0.94
	0.05	0.24	0.42	0.55
O_2	0.05	0.25	0.41	0.53
	0.05	0.24	0.42	0.51
	0.01	0.09	0.17	0.25
CH_4	0.01	0.09	0.18	0.24
	0.01	0.08	0.18	0.25
	0.01	0.05	0.26	0.39
CO_2	0.03	0.08	0.42	0.48
(explicit model)	0.06	0.24	0.70	0.66

Table 9. Solubilities predicted for a statistical lattice of PMP.

Grid Spacing[a]	CH_4	CO_2
0.75	0.018	0.020
0.50	0.019	0.051
0.25	0.020	0.097

[a] In Å.

CAPTIONS TO FIGURES

Figure 1. Schematic representation of the simulation box used for crystalline PMP. The dashed circles correspond to the position of the four chains explicitly included in the simulation. The chains are labelled with numbers. R and L refer to right- and left-handed helices, respectively. The fiber axis is 13.68 Å.

Figure 2. Representative microstructure of the PMP obtained in the MC-2 simulation of model **a**. It consist of pairs of upward (u) and downward (d) helices with different handedness. R and L refer to right- and left-handed helices, respectively.

Figure 3. Setting angle of PMP as a function of the number of steps obtained from MC simulations with the AMBER/IUA, AMBER/AUA and AMBER/AA force-fields.

Figure 4. Fractional unoccupied space distribution with respect to the sphere radius of gas penetrants for different helical polymers.

Figure 5. Solubility-unoccupied space correlation map. The solubilities predicted for He (a), Ar (b) and CH_4 (c) in different polymeric matrices are plotted against the fractional unoccupied space.

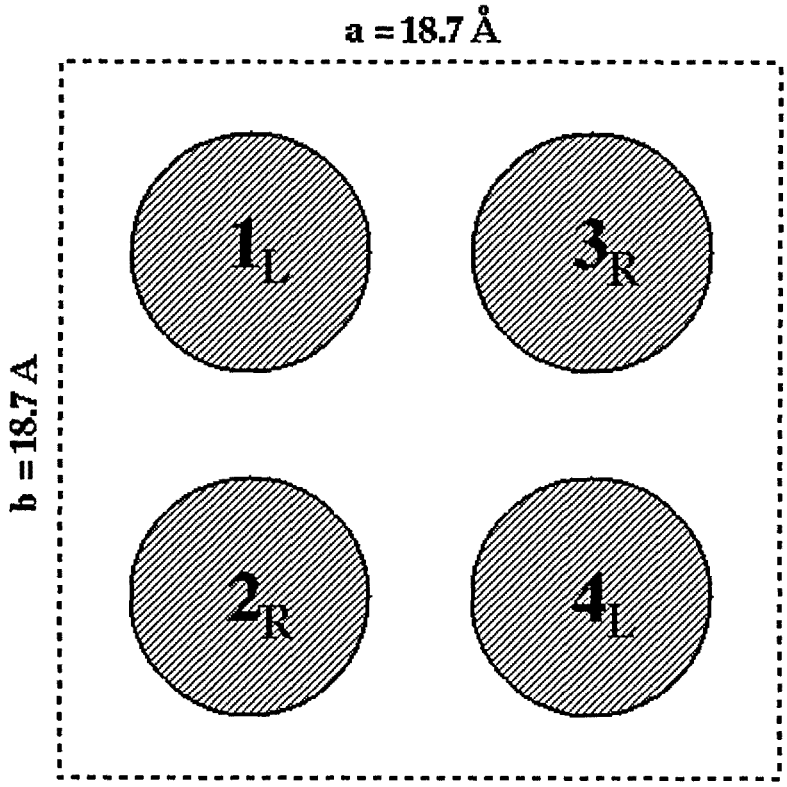

Fig.1. Zanuy et al

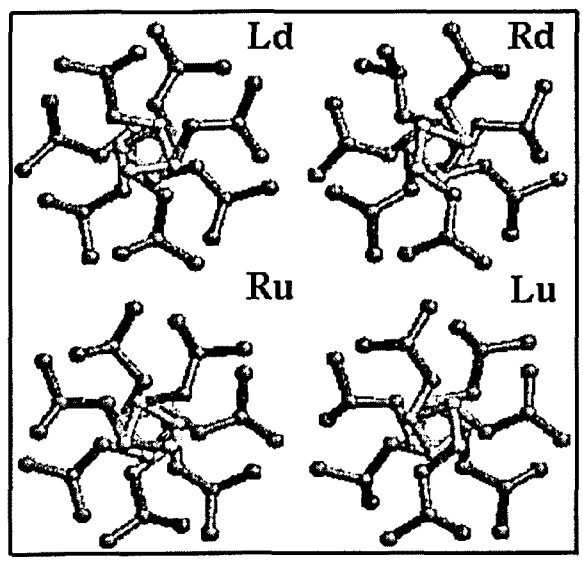

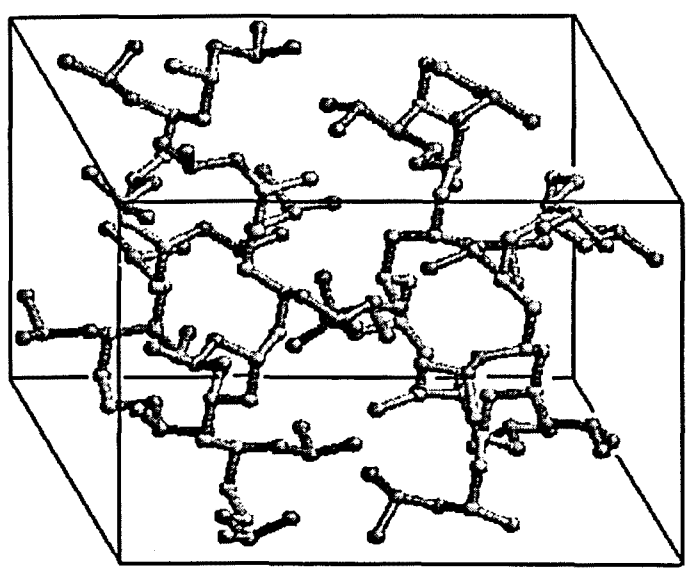

Fig.2. Zanuy et al

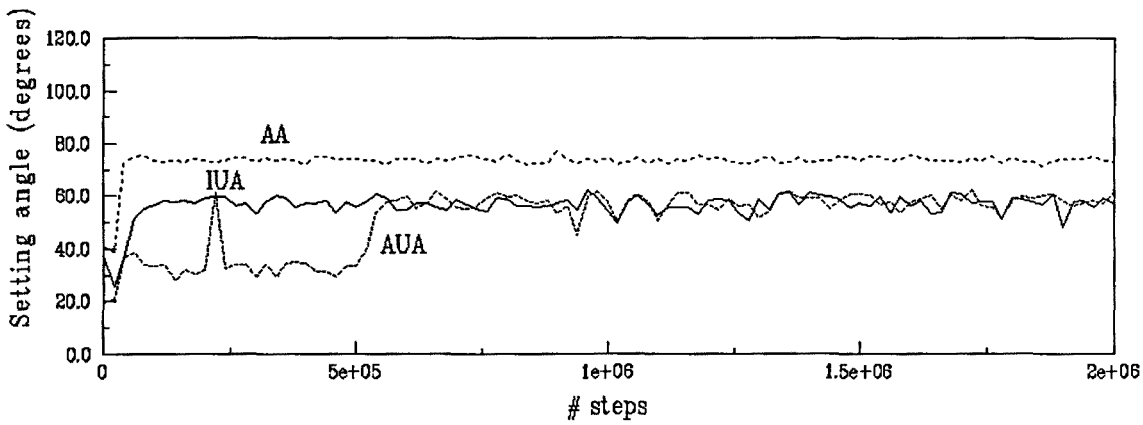

Fig.3. Zanuy et al

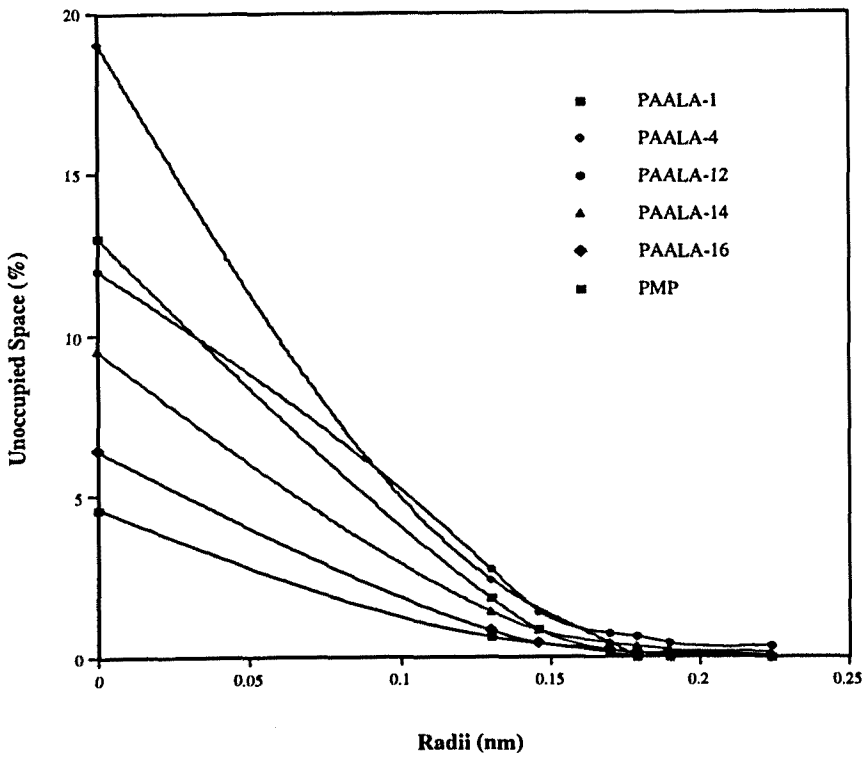

Fig.4. Zanuy et al

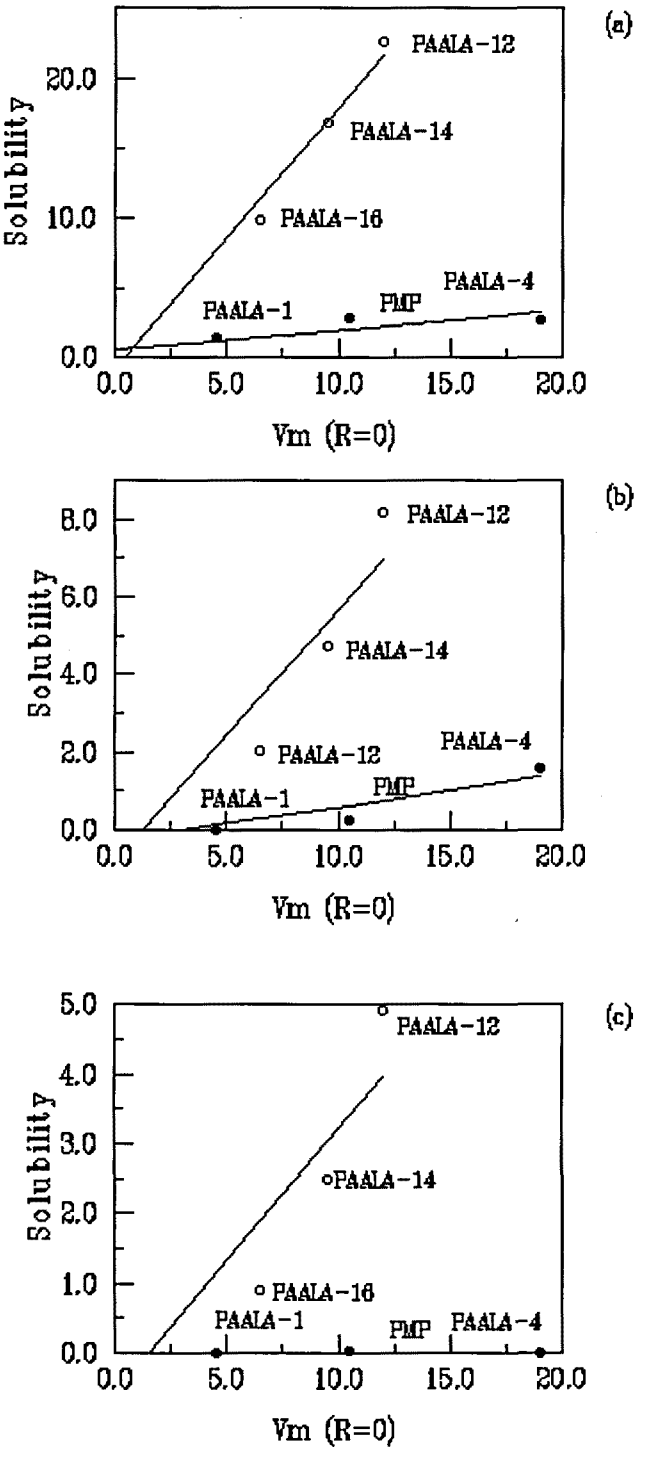

Fig.5. Zanuy et al

VIII.6. "Molecular simulations of gas solubilities in cristalline poly(α-alkyl-β-L-aspartate)s"

Zanuy, D.; León S.; Alemán C.; Muñoz-Guerra, S. *Polymer*, **2000**, *41*, 4169-4177.

ELSEVIER

Polymer 41 (2000) 4169–4177

polymer

Molecular simulation of gas solubilities in crystalline poly(α-alkyl-β-L-aspartate)s

D. Zanuy, S. León, C. Alemán*, S. Muñoz-Guerra

Departament d'Enginyeria Química, E.T.S. d'Enginyers Industrials de Barcelona, Universitat Politècnica de Catalunya, Diagonal 647, Barcelona E-08028, Spain

Received 29 March 1999; received in revised form 2 July 1999; accepted 2 September 1999

Abstract

We have studied the solubility of a small probe particle, the atoms He and Ar and the molecule CH_4 in the helical poly(α-alkyl-β-L-aspartate)s using molecular simulations. The hexagonal and tetragonal crystal forms of poly(α-*n*-butyl-β-L-aspartate) and the hexagonal form of the poly(α-methyl-β-L-aspartate) have been chosen for the study as the most representative structures for this family of polymers. An important characteristic of these structures is that the helical conformations are retained at high temperatures. The excess chemical potentials have been determined using Widom's test-particle insertion method considering an ensemble of microstructures generated by Monte Carlo calculations. The solubility of the different penetrants in the polymer systems was explained in terms of the distribution of the unoccupied space.

Keywords: Solubility; Molecular simulation; Poly(α-alkyl-β-L-aspartate)s

1. Introduction

The application of atomistic simulations to study the solubility of gas molecules in dense polymers has become a topic of broad interest in recent years due to the availability of more powerful computers [1,2]. These simulations are able to afford information about the polymer and/or the penetrant that is not readily accessible from experiments. Thus force-field simulations have provided a description of the mechanism of gas permeation in terms of the *free volume*. It should be mentioned that the term *free volume* in the context of gas transport refers to the volume not occupied by the atoms in the system [3,4]. Furthermore, atomistic simulations have confirmed that diffusion involves jumps of the gas molecules in the polymeric matrix, i.e. the hopping mechanism deduced 50 years ago [1,5–7]. In such a description the movement of the gas molecules is thought to be coupled to the elastic motion of the polymer chains but it is independent from the structural relaxation of the polymeric matrix.

Computational studies usually involve the solubility of gas molecules in amorphous host polymers. This is because the mobility of the penetrant is much higher in the amorphous phase than in the crystalline phase since the packing of the chains is much more loose in the former state. Accordingly, it has been traditionally accepted that the transport of gases in a semicrystalline polymer takes place mainly through the amorphous phase and so it has been confirmed in recent studies [8]. However, Puleo et al. [9] demonstrated that poly(4-methyl-1-pentene) (Fig. 1), abbreviated PMP displayed an exceptional behavior since similar permeabilities were found for the amorphous and crystalline regions. This finding is supported by the fact that the crystalline and amorphous densities in PMP are very similar and, therefore, the two phases should have a nearly equal amount of *free volume*. The crystal structure of PMP was determined by Tadokoro and coworkers [10]. It consists of four 7/2 helices packed together to form a tetragonal unit cell. In this structure the packing of the helices is very inefficient due to the presence of bulky and flexible pendent groups. The diffusion of carbon dioxide and methane in crystalline PMP was investigated at the atomistic level by Müller-Plathe using molecular dynamics simulations [11]. The results allowed to understand better the behavior of these penetrants in crystalline PMP and the unusually low barrier to gas diffusion displayed by this polymer.

Poly(α-alkyl-β-L-aspartate)s are nylon 3 derivatives with an alkoxycarbonyl group stereoregularly attached to every third backbone carbon atom of the repeating unit [12]. A schematic representation of the chemical formula of this

* Corresponding author. Tel.: +34-93401-6680/6681; fax: +34-93401-6600/7150.

E-mail address: aleman@eq.upc.es (C. Alemán).

0032-3861/00/$ - see front matter
PII: S0032-3861(99)00635-7

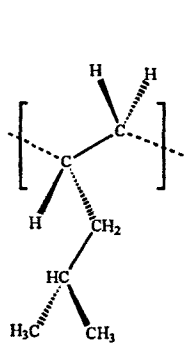

PMP

Poly 4-methyl-1-pentene

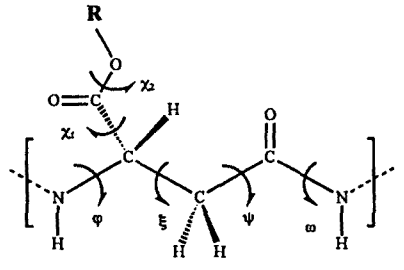

a) R: $-CH_2-(CH_2)_2-CH_3$ PAALA-4

b) R: $-CH_3$ PAALA-1

Poly (α-alkyl-β-L-aspartate)s

Fig. 1. Structure formulae of the repeating units of poly(4-methyl-1-pentene) and poly(α-alkyl-β-L-aspartate)s. Notations used for the dihedral angels in poly(α-alkyl-β-L-aspartate) are indicated.

family of polymers is given in Fig. 1. Recent studies on a number of poly(α-alkyl-β-L-aspartate)s including a variety of side chain compositions have shown that they adopt helical structures with features similar to those of the α-helix of polypeptides [13–19]. The most frequent helical arrangement found in the solid state for poly(α-alkyl-β-L-aspartate)s is the right-handed 13/4 helix, with intramolecular hydrogen bonds set between the amide groups i and $i + 3$. A second important conformation is the 4/1 helix based on an $i - i + 4$ hydrogen-bonding scheme. Other related helices occasionally observed are those consisting of 16/5 and 17/4 arrangements [15,16], which are closely related to the 13/4 helix and 4/1 helices, respectively.

The mode of packing and degree of ordering achieved in these systems are known to be largely dependent on the length of the alkyl side groups. Thus, the so-called hexagonal form, which is a monoclinic lattice of up-and-down chains in the $P2_1$ space group, is a structure invariably found in poly(α-alkyl-β-L-aspartate)s with alkyl side chains containing up to five carbon atoms [13–15]. In addition a second polymorph with a tetragonal structure in the space group $P4_1$ is observed when the polymer adopts the 4/1 helical conformation. On the other hand, a biphasic structure with 13/4 helices arranged in layers and side chains crystallized in a separated phase has been observed for derivatives bearing linear alkyl groups with 12, 18 and 22 carbon atoms [18,19]. An important characteristic of all these structures is that the backbone helical conformations are retained at high temperatures remaining immobilized in the crystal lattices, as revealed X-ray diffractograms recorded at different temperatures [18].

There are significant resemblances between the crystal structures of poly(α-alkyl-β-L-aspartate)s, in particular of those bearing short to medium size linear side chains, and that of PMP: (i) their molecular chains adopt helical conformations with a relatively close symmetry; (ii) the 4/1 helices of poly(α-alkyl-β-L-aspartate)s pack in a tetragonal lattice similar to that found for the 7/2 helices of PMP; and (iii) the flexible side groups protrude from the main chain to invade the intermolecular space in a similar manner. Furthermore, it should be noticed that poly(α-alkyl-β-L-aspartate)s present a lower density of side groups than PMP so that a larger *free volume* should be expected a priori for the formers. Accordingly, a study about the behavior of small penetrants in poly(α-alkyl-β-L-aspartate)s is highly desirable.

In this work we present a predictive study about the behavior of small gas molecules in some crystalline poly(β-L-aspartate)s using molecular simulations. Since no experimental evaluation is available at the present time, simple penetrants He, Ar and CH_4 were chosen. In addition a probe particle (abbreviated SPP) with a size even smaller was analyzed. The systems investigated were the hexagonal and tetragonal forms of poly(α-*n*-butyl-β-L-aspartate) (PAALA-4) and the hexagonal form of poly(α-methyl-β-L-aspartate) (PAALA-1), which are the most representative crystal structures of this family of polymers. To generate a number of PAALA-4 and PAALA-1 microstructures, we performed Monte Carlo calculations in periodic simulation cells where the conformation of the side chains were allowed to vary. The excess chemical potentials were then computed using an efficient implementation of Widom's test-particle insertion method [20].

2. Methods

2.1. Starting structures

The starting geometries for the different structures investigated were taken from our previous works [14,15]. The unit cell for the hexagonal and tetragonal forms of PAALA-4 are ($a = 13.4$ Å, $c = 20.60$ Å) and ($a = 14.1$ Å, $c = 4.90$ Å), respectively, whereas the unit cell of the hexagonal form of PAALA-1 is ($a = 12.03$ Å, $c = 20.51$ Å). The

Table 1
Crystallographic parameters and dihedral angles (in °) for the helical conformations of PAALA-4 and PAALA-1 obtained from the refinements against the X-ray data

Polymer	Helix	Crystal form	Unit cell (Å)	Space group	ϕ	ξ	ψ	ω	χ_1	χ_2	χ_i ($i = 2,5$)
PAALA-4	13/4	Hexagonal	$a = 13.4$; $c = 20.60$	$P2_1$	146.2	−59.8	128.8	180.0	173.4	180.0	180.0
PAALA-4	4/1	Tetragonal	$a = 14.1$; $c = 4.90$	$P4_1$	144.4	−87.2	148.1	180.0	146.4	180.0	180.0
PAALA-1	17/4	Hexagonal	$a = 12.03$; $c = 20.51$	$P2_1$	141.7	−92.3	155.4	180.0	145.8	180.0	–

position of the helices within the unit cell as well as the conformational parameters of the three types of helices were refined against the X-ray diffraction data in previous works [14,15]. Table 1 reports the crystallographic parameters and dihedral angles obtained from these refinements for the 13/4 and 4/1 helices of PAALA-4 and the 17/4 helix of PAALA-1. The projection along the *c*-axis of the three crystal forms investigated is displayed in Fig. 2.

2.2. Generation of microstructures

A number of microstructures for the hexagonal and tetragonal forms of PAALA-4 and the hexagonal form of PAALA-1 was required in order to study the solubility of the penetrants in these systems. They were obtained using an advanced Monte Carlo sampling technique (continuum configurational bias, CCBMC), which has already been found to be efficient in the study of dense systems [21,22]. In addition to CCB moves, a small fraction (20%) of Metropolis moves were also used. It should be remarked that the generated microstructures only differ in the conformations of the flexible side chains and that the helices within the unit cell were retained in the positions observed by X-ray diffraction (see later). The simulations started from the unit cells described in Section 2.1 and showed in Fig. 3. The boxes used in the simulation consist of four independent chains of 13, 12 and 17 residues for the hexagonal and tetragonal forms of PAALA-4 and the hexagonal form of PAALA-1, respectively. The size and density of the boxes used for the simulations are displayed in Table 2, where the experimental density is also included for comparison. Periodic continuation conditions and the minimum-image convention were applied to all simulations. MC simulations of 100,000 steps of the NVT type, i.e. without varying the size of the cell, were performed at 298 K after equilibration. For each simulation 50 microstructures were sampled at 2000 steps intervals.

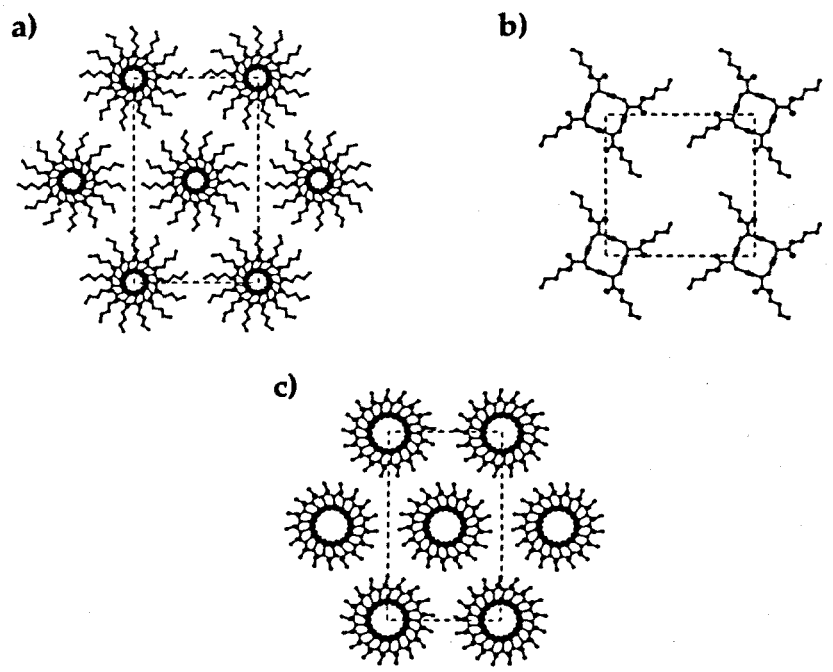

Fig. 2. Projection along the *c*-axis of the unit cells of the: (a) hexagonal form of poly(α-*n*-butyl-β-L-aspartate) 13/4 helices; (b) tetragonal form of poly(α-*n*-butyl-β-L-aspartate) 4/1 helices; and (c) hexagonal form of poly(α-methyl-β-L-aspartate) 17/4 helices. The chains have been drawn with an increased separation between them in order to show the molecular arrangement more clearly.

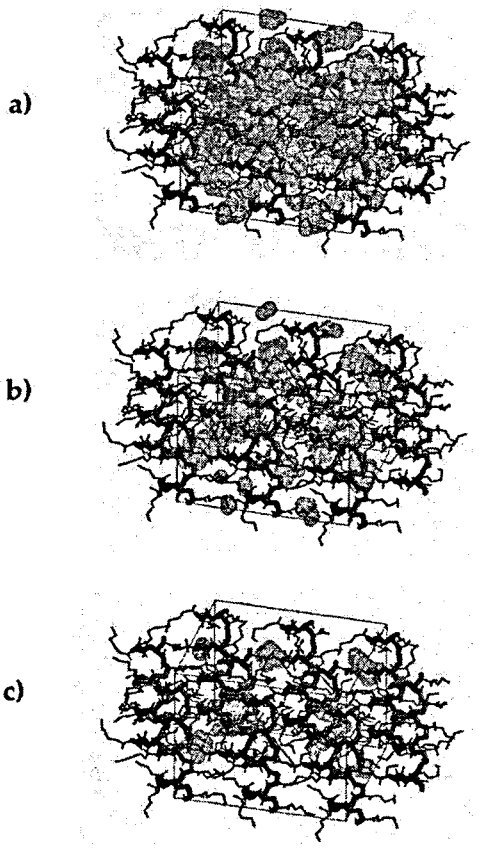

Fig. 3. Unoccupied space for (a) SPP, (b) He (c) and Ar penetrants in one of the microstructures generated for the hexagonal form of poly(α-*n*-butyl-β-L-aspartate).

The model used in the MC calculations assumed fixed bond lengths and bond angles for the side chains; main chain dihedral angles were entirely fixed to the values found from the refinement of the X-ray data (see Table 1). The assumption of fixed backbones is quite reasonable for the systems under study since X-ray diffraction studies at different temperatures clearly revealed that the corresponding helical conformations are retained at high temperatures [18]. Helix centers, defined as the intersections of helix axes (running along the *z*-direction) with *xy*-plane, were fixed relative to the unit cell, i.e. they remained fixed during all the moves. The only degrees of freedom of the system were therefore the torsional angles associated to the ethylene

Table 2
Size (in Å) and density (ρ, in g/ml) of the boxes used for the Monte Carlo simulations (experimental densities (ρ_{exp}) are also displayed for comparison)

PAALA	Crystal form	*a*	*b*	*c*	ρ	ρ_{exp}
PAALA-4	Hexagonal	26.9	23.3	20.60	1.18	1.17
PAALA-4	Tetragonal	28.2	28.2	14.73	1.21	1.18
PAALA-1	Hexagonal	24.06	20.89	21.90	1.33	1.36

Table 3
Lennard-Jones potential parameters for the penetrants

Penetrant	*R* (Å)	ϵ (kcal/mol)
SSP	0.93	0.010
He	1.30	0.020
Ar	1.70	0.238
CH_4	1.91	0.294

bonds of the side chains. The AMBER [23] force field was used to represent the van der Waals and torsional energies of the system. Electrostatic interactions were neglected since all the polar groups were kept fixed along the simulations. The results of preliminary calculations using models of all atoms and united atoms models for both methyl and methylene groups were very similar. Accordingly, the model of united atoms was used due to its lower computational cost. The van der Waals energy was computed in the usual pairwise additive way using a Lennard-Jones 6–12 potential. Lennard-Jones potentials were truncated at 8 Å.

2.3. Free volume measurements

The unoccupied space in a given microstructure was estimated using the van der Waals radii of both the penetrant and polymer. This was done by dividing the simulation box of every microstructure into a three-dimensional uniformly spaced grid. These grids consisted of 975529, 893101 and 794325 nodes for the hexagonal and tetragonal forms of PAALA-4 and the hexagonal form of PAALA-1, respectively. Then, a penetrant was centered in each node and the distance to the nearest atom of the polymeric matrix was measured. If this distance was larger than the sum of the van der Waals radii of the penetrant and the polymer atom the node was identified as unoccupied. The van der Waals radii used for the penetrants are displayed in Table 3, whereas those of the polymer atoms were taken from the AMBER libraries [23].

2.4. Widom's test-particle insertion method

The infinite-dilution excess chemical potentials of a penetrant sorbed in poly(β-L-aspartate)s structures were estimated using Widom's test-particle insertion method [24,25]. In this method the chemical potential of species *i* in a frozen *N*-particle system relative to an ideal gas mixture is related to the potential energy of inserting a test-particle into the system at randomly chosen positions. The expression for the excess chemical potential is:

$$\beta\mu_i^{ex}(\rho,T) = -\ln\langle\exp(-\beta\phi_t)\rangle_N \quad (1)$$

where $\beta = 1/k_BT$, ϕ_t is the interaction energy between the test-particle and the *N* particles of the system, and $\mu_i^{ex}(\rho,T)$ is the excess of chemical potential of species *i* at temperature *T* and number density $\rho = N/V$. The brackets $\langle\cdots\rangle_N$

Table 4
Fraction of predicted *free volume* (averaged over the 50 microstructures generated by MC simulations) (V_{free}; in %) for the different penetrants (the V_{free} for CH_4 was zero in all the cases) in the hexagonal and tetragonal forms of PAALA-4 and the hexagonal form of PAALA-1 [the standard deviation (σ; in %) and the maximum and minimum values (in %) of the *free volume* for each set of microstructures are also displayed]

Polymer	Form	Diffusant	V_{free}	σ	Maximum	Minimum
PAALA-4	Hexagonal	SPP	6.24	±0.35	7.05	5.49
		He	2.37	±0.27	3.02	1.89
		Ar	0.70	±0.16	1.09	0.41
PAALA-4	Tetragonal	SPP	2.70	±0.21	3.08	2.13
		He	0.62	±0.15	0.94	0.31
		Ar	0.08	0.03	0.16	0.01
PAALA-1	Hexagonal	SPP	2.95	±0.04	3.04	2.87
		He	0.26	±0.02	0.29	0.23
		Ar	< 0.01	-	-	-

denote the canonical ensemble average over the original N-particle system (without test-particle) at the T and ρ of interest. The test-particle insertion method has been used successfully at low to moderate fluid densities [26–28]. However, at high densities the method becomes inefficient as it becomes increasingly unlike that a test particle can be inserted successfully into the fluid. That is, the insertions that provide a positive value for ϕ_t due to repulsive overlaps in a high-density fluid have a negligible contribution to μ_i^{ex} (see Eq. (1)). Different methods have been proposed to obtain significant improvements in the insertion efficiency [20,28–33]. These studies have revealed that a satisfactory approximation is achieved by searching only those regions where successful particle insertions are more likely to occur [20,31–33]. Within this framework Cuthbert et al. [20] defined the ensemble average $\langle \exp(-\beta\phi_t)\rangle_N$ (Eq. (1)) as follows:

$$\langle \exp(-\beta\phi_t)\rangle_N = \sum_{j=1}^{N_e} (1/N_{Tj}) \sum_{i=1}^{N_{Vj}} \exp(-\beta\phi_{t,i}) \qquad (2)$$

where N_{Vj} is the number of sites without overlaps in the microstructure j, N_{Tj} is the total number of insertions for a given microstructure j assuming a uniform insertion density, and N_e is the total number of microstructures available for computing the ensemble of averages.

We have used Eq. (2) to compute the excess chemical potential. For this purpose, we have divided the microstructures into uniformly spaced grids. A penetrant particle was centered in each node only if it is identified as unoccupied. Calculations were performed considering spacings between consecutive nodes of 1, 0.75, 0.50 and 0.25 Å. In order to normalize this biased sampling, the average of μ_i^{ex} for each microstructure was weighted by $\omega_j = N_{Vj}/N_{Tj}$ before being summed to yield the ensemble average. Lennard-Jones interactions between the penetrants and the polymer atoms were computed using a Lennard-Jones 6–12 potential and applying the standard Lorentz–Berthelot mixing rules. The force-field parameters used for the penetrants are displayed in Table 3. The interaction energies were truncated at 8 Å.

3. Results and discussion

In order to ensure that the generated microstructures are statistically independent we computed for the three systems under study the first and second degree bond autocorrelation functions as well as the relaxation function of the end-to-end distance vector [34]. All these functions decay rapidly to small values (data not shown) following the same behavior predicted for polyethylene chains [34]. These results indicate that the microstructures recorded out of each other by 2000 MC moves are independent.

As a first step of MC data evaluation, we examined the unoccupied space of all the generated microstructures. These results are summarized for each penetrant in Table 4, which displays the amount of *free volume* averaged over the 50 microstructures recorded for the three systems under study. It is worth to note that for PAALA-4 the largest *free volume* results for the hexagonal form, being about two times that of the tetragonal form for all the penetrants. This correlates well with the measured densities, which are 1.06 and 1.18 g/ml, respectively. On the other hand, the amount of *free volume* predicted for the hexagonal form of PAALA-1 is close to that of tetragonal form of PAALA-4. The large density measured for the hexagonal form of PAALA-1 (1.36 g/ml) revealed that it has a much more compact structure than the hexagonal form of PAALA-4. This is in part due to the different hydrogen bonding scheme adopted by these two polymers. In fact the central hole of the 17/4 helix of PAALA-1 is wider than that of the 13/4 helix of PAALA-4 (Fig. 2) providing the former with a more compact crystal packing of the side chains.

As can be seen from the small standard deviations of the averages as well from both the maximum and minimum values of the predicted *free volume* within each set of microstructures (see Table 4), all the models generated for a given polymer present a similar unoccupied space. This trend suggests that the number of microstructures generated is suitable for the present study.

An analysis of the results obtained for the different penetrants reveals some important features. As can be expected,

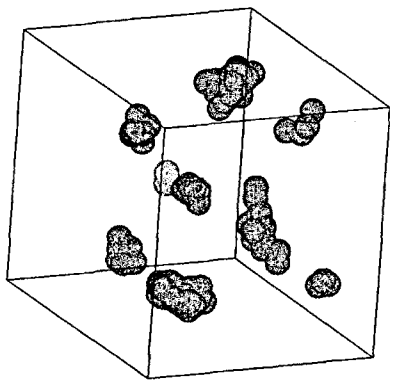

Fig. 4. Ellipsoid-shaped cavities for Ar penetrant in one of the microstructures generated for the hexagonal form of PAALA-4.

the *free volume* decreases when the size of the penetrant increases, being zero in all the cases for CH_4. These results further indicate that a number of SPP, He and Ar molecules are able to fit within the hexagonal form of PAALA-4, whereas the space available for the latter penetrant in the tetragonal form of PAALA-4 and the hexagonal form of PAALA-1 is very small. Thus, the ratios that relate the *free volume* for the different penetrants drastically increase with the density of the system. Thus, in the hexagonal form of PAALA-4 the *free volume* for SPP is a factor of 2.6 and 8.9 larger than those for He and Ar, respectively. These factors increase to 4.5 and 33.7 for the tetragonal form of PAALA-4, and to 11.3 and >100 for the hexagonal form of PAALA-1.

A visual inspection of the volume accessible to the penetrants in microstructures of the hexagonal form of

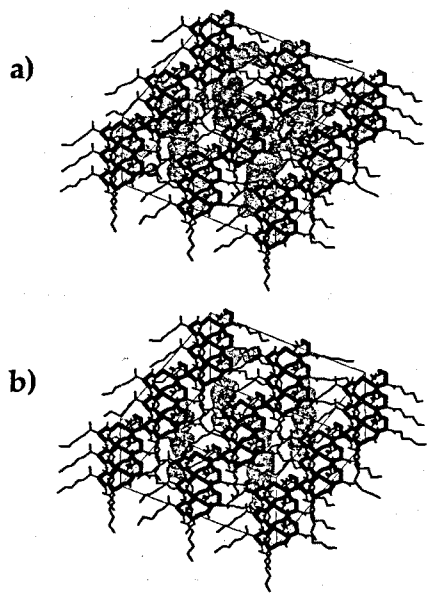

Fig. 5. Unoccupied space for (a) SPP (b) and He penetrants in one of the microstructures generated for the tetragonal form of poly(α-*n*-butyl-β-L-aspartate).

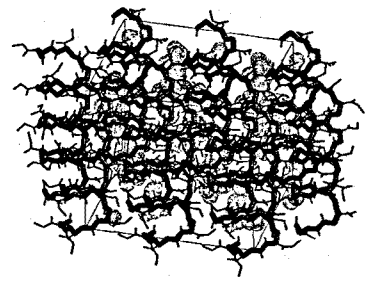

Fig. 6. Unoccupied space for SPP penetrant in one of the microstructures generated for the hexagonal form of poly(α-methyl-β-L-aspartate).

PAALA-4 reveals their cavernous distribution. Fig. 3 depicts the *free volume* for SPP, He and Ar in one of the microstructures. Typically, the cavities are ellipsoids with 3–9, 3–7 and 3–6 Å in length for SPP, He, and Ar, respectively. Fig. 4 shows a detailed view of the ellipsoid-shaped cavities for Ar in one of the microstructures. In all cases these ellipsoids are less than 3.5 Å in width. For the SPP penetrant, the cavities are occasionally separated by a bottleneck of about 3–4 Å in length and 1–2 Å in width allowing the easy passage from one cavity to other. On the other hand, we never found long channels constituted by a number of cavities connected by passages.

Analysis of the *free volume* for the SPP and He penetrants in microstructures of the tetragonal form of PAALA-4 revealed a completely different distribution of the unoccupied space. Thus, about 70 and 16% of the microstructures display one or more channels crossing the simulation box for SPP and He, respectively. Fig. 5 illustrates the presence of channels for SSP and He in one microstructure. These channels are about 1.5–3.5 and 1.5–2.25 Å in width, respectively. This is a surprising result since the *free volume* is smaller for the tetragonal form than for the hexagonal form. This apparently anomalous behavior is due to the more ordered packing of the side chains in the former form. On the contrary, a cavernous distribution of the accessible volume similar to that of the hexagonal form was detected when Ar was the tested penetrant.

A cavernous distribution of the *free volume* was also found for the hexagonal form of PAALA-1. The cavities are 3–5 and 2–3 Å in size for SPP and He penetrants, respectively. Bottlenecks of about 2 Å in length and 1.5 Å in width connecting different cavities were found for SSP, whereas no passage was found for He. As was discussed before no cavity was found for Ar. Fig. 6 shows the distribution of the *free volume* for SSP in one of the microstructures of PAALA-1 with no channels outlined.

Table 5 shows the calculated excess chemical potentials for the three structures investigated considering grid spacings of 1, 0.75, 0.50 and 0.25 Å. The results indicate that grid spacings finer than 0.75 Å displayed no significant changes in the resulting excess chemical potential of the hexagonal and tetragonal forms of PAALA-4. Conversely, the excess chemical potential for PAALA-1 fluctuates when

Table 5
Excess chemical potentials (kcal/mol) for the different penetrants in the hexagonal and tetragonal forms of PAALA-4 and the hexagonal form of PAALA-1

Penetrant	Grid spacing	PAALA-4 Hex	PAALA-4 Tet	PAALA-1 Hex
SPP	1	−2.17	−1.66	1.73
	0.75	−2.18	−1.68	−1.72
	0.50	−2.18	−1.68	−1.69
	0.25	−2.19	−1.68	−1.65
He	1	−1.60	−0.81	−0.29
	0.75	−1.62	−0.80	−0.18
	0.50	−1.62	−0.82	−0.26
	0.25	−1.63	−0.83	−0.23
Ar	1	−0.81	0.38	–
	0.75	−0.91	0.34	–
	0.50	−0.91	0.37	–
	0.25	−0.93	0.37	–

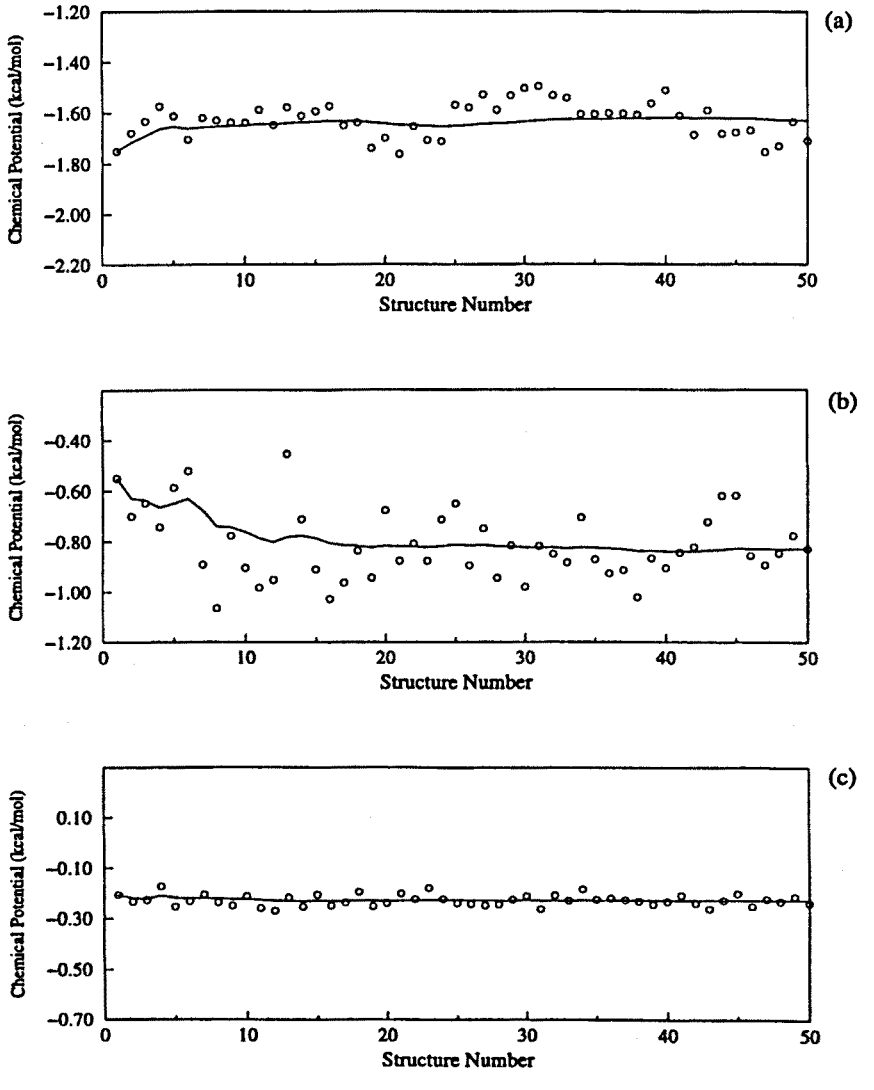

Fig. 7. Convergence of the excess chemical potential of He calculated using Widom's test-particle insertion method in the 50 microstructures obtained from MC calculations for the: (a) hexagonal form of poly(α-*n*-butyl-β-L-aspartate); (b) tetragonal form of poly(α-*n*-butyl-β-L-aspartate); and (c) hexagonal form of poly(α-*n*-methyl-β-L-aspartate).

the size of the grid changes. This could be due either to using an insufficient number of microstructures to converge the process or to the particular distribution of the *free volume* in this polymer. Fig. 7 shows the progress of the excess chemical potential of He for the 50 generated microstructures of the three polymers considering a grid spacing of 0.25 Å. Each point corresponds to one application of Eq. (1) to one of the 50 microstructures generated from MC simulations whereas the solid line displays the mean value of resulting excess chemical potential up to this microstructure. It is worth to note that the line drawn is running average over the points indicating the convergence of these calculations. Accordingly, we can conclude that the fluctuating behavior of the resulting excess chemical potential for PAALA-1 is due to the cavernous distribution of the *free volume* in this system. Thus, it should be emphasized that although the hexagonal form of PAALA-4 also presents a similar distribution of the *free volume*, the size of the cavities is considerably higher due to its lower density (see Table 4).

The results displayed in Table 5 indicate that the interactions of both SPP and He penetrants with the polymer matrix are favorable in all cases. Within a given crystal form the strength of these interactions decreases with the size of the penetrant, whereas for a given penetrant the interactions are more favorable when the amount of *free volume* increases. It is seen as Ar has a significantly higher excess chemical potential in the tetragonal form of PAALA-4 relative to the hexagonal form. These less favorable interactions would result from a larger number of low-energy configurations when Ar is inserted into the polymer matrix. Thus, the small amount of *free volume* for Ar indicates that there are few cavities inside the polymer matrix that are of sufficient size to stabilize the insertion of this penetrant.

Results achieved in this study indicate that the solubility of small penetrants in poly(α-alkyl-β-L-aspartate)s is lower than that observed and predicted for crystalline PMP [9,11] as a logical consequence of the smaller amount of *free volume* present in those polymers. Furthermore, the *free volume* in PMP is distributed in channels of sufficient size to accommodate CO_2 and CH_4 gas molecules. Conversely, the hexagonal forms of PAALA-1 and PAALA-4 present an irregular distribution of the *free volume*. On the other hand, the unoccupied space of tetragonal form of PAALA-4 is distributed in channels, although they continue to be unable to fit penetrants higher than He.

4. Conclusions

We have performed a molecular simulation study of the solubility of small gaseous penetrants in crystalline poly(α-alkyl-β-L-aspartate)s. More specifically, the solubilities of SPP, He, Ar and CH_4 in the hexagonal and tetragonal forms of PAALA-4 and the hexagonal form of PAALA-1 were predicted using Widoms test-particle insertion method. A number of microstructures were generated for the three crystal forms using an advanced Monte Carlo sampling technique.

A cavernous distribution of the *free volume* was found for the hexagonal form of PAALA-4 and PAALA-1, the dimensions of the cavities precluding the accommodation of penetrants larger than Ar and He, respectively. On the other hand, a number of microstructures with channels were detected for the tetragonal form of PAALA-4. The size of the channels was sufficient to accommodate SPP and He particles but not Ar. In all the systems investigated the holes were too small to permit the solubility of CH_4. The calculated excess chemical potentials reveal favorable interactions between the polymer matrix and the two smallest penetrants SPP and He, for the three crystal forms. However, Ar was predicted to be soluble in the hexagonal form of PAALA-4 but not in the tetragonal form. The large excess chemical potential predicted for this gas in the tetragonal form of PAALA-4 was caused by the much stronger repulsive Lennard-Jones interactions. The present results indicate that small gaseous penetrants present a lower solubility in poly(α-alkyl-β-L-aspartate)s than crystalline PMP even though both types of compounds share many structural features.

Acknowledgements

This work was supported by DGICYT with grant no. PB96-0490. D.Z. and S.L. acknowledge the support of the Ministry of Education of Spain for the award of a scholarship. Authors wish to thank Prof M. Laso, Universidad Politécnica de Madrid, for assistance in the preparation of MC simulations.

References

[1] Gusev AA, Müller-Plathe F, van Gunsteren WF, Suter UW. Adv Polym Sci 1994;116 p. 116, 207.
[2] Müller-Plathe F. Acta Polym 1994;45:259.
[3] Arizzi S, Mott PH, Suter UW. J Polym Sci Part B 1992;30:415.
[4] Vrentas JS, Duda JL. J Polym Sci, Polym Phys Ed 1977;15:403.
[5] Sok RM, Berendsen HJC, van Gunsteren WF. J Chem Phys 1992;96:4699.
[6] Müller-Plathe F. J Chem Phys 1991;94:3192.
[7] Sonnenburg J, Gao J, Weiner JH. Macromolecules 1990;23:4653.
[8] Müller-Plate F. Chem Phys Lett 1991;177:527.
[9] Puleo AC, Paul DR, Wong PK. Polymer 1989;30:1357.
[10] Kusanagi H, Takase M, Chatani Y, Tadokoro H. J Polym Sci, Polym Phys Ed 1978;16:131.
[11] Müller-Plathe F. J Chem Phys 1995;103:4346.
[12] Fernández-Santín JM, Aymamí J, Rodríguez-Galán A, Muñoz-Guerra S, Subirana JA. Nature (London) 1984;311:53.
[13] López-Carrasquero F, Alemán C, García-Alvarez M, Martínez de Ilarduya A, Muñoz-Guerra S. Makromol Chem Phys 1995;196:253.
[14] Navas JJ, Alemán C, López-Carrasquero F, Muñoz-Guerra S. Macromolecules 1995;28:4487.
[15] López-Carrasquero F, García-Alvarez M, Navas JJ, Alemán C, Muñoz-Guerra S. Macromolecules 1996;29:8449.

[16] García-Alvarez M, León S, Alemán C, Campos JL, Muñoz-Guerra S. Macromolecules 1998;32:124.
[17] García-Alvarez M, Martínez de Ilarduya A, León S, Alemán C, Muñoz-Guerra S. J Phys Chem A 1997;101:4215.
[18] López-Carrasquero F, Montserrat S, Martínez de Ilarduya A, Muñoz-Guerra S. Macromolecules 1995;28:5535.
[19] Navas JJ, Alemán C, López-Carrasquero F, Muñoz-Guerra S. Polymer 1997;38:3477.
[20] Cuthbert TR, Wagner NJ, Paulaitis ME. Macromolecules 1997;30:3058.
[21] de Pablo JJ, Laso M, Suter UW. J Chem Phys 1992;96:6157.
[22] de Pablo JJ, Laso M, Suter UW. Macromolecules 1993;26:6180.
[23] Weiner SJ, Kollman PA, Case DA, Singh UC, Ghio C, Alagona G, Profeta S, Weiner P. J Am Chem Soc 1984;106:765.
[24] Widom B. J Phys Chem 1982;86:869.
[25] Widom B. J Chem Phys 1963;39:2808.
[26] van der Vegt NFA, Briels WJ, Wessling M, Strathmann H. J Chem Phys 1996;105:8849.
[27] Bicerano J, Moll DJ. Comput Polym Sci 1996;6:117.
[28] Torrie GM, Valleau JP. Chem Phys Lett 1974;28:578.
[29] Knopp B, Suter UW, Gusev AA. Macromolecules 1997;30:6107.
[30] Knopp B, Suter UW. Macromolecules 1997;30:6114.
[31] Dietrick GL, Scriven LE, Davis HT. J Chem Phys 1989;90:2370.
[32] Sok RM, Berendsen HJC, van Gunsteren WF. J Chem Phys 1992;96:4699.
[33] Tamai Y, Tanaka H, Nakanishi K. Macromolecules 1995;28:2544.
[34] Leontidis E, de Pablo JJ, Suter UW. Adv Polym Sci 1994;116:283.

Prefacio

El autor de esta memoria únicamente ha obtenido una parte de los resultados presentados en esta sección. Estos corresponden específicamente al modelado de la estructura y al estudio de la solubilidad de gases.

VIII.7. "On the phase B of comb-like poly(α-alkyl-β-L-aspartate)s: A simulation of the solubility of small penetrants"

D. Zanuy, C. Aleman, F. Lopez-Carrasquero, M. E. Baez, M. Garcia-Alvarez, M. Laso, S. Muñoz-Guerra, *Macromol. Chem. Phys.* **2001**, *202*, 564-573

Macromol. Chem. Phys. 2001, 202, 564–573

Full Paper: The structure and thermal properties of the phase B of poly(α-alkyl-β-L-aspartate)s, abbreviated PAALA-*n* (*n* being the number of carbon atoms in the linear alkyl side chain), with *n* = 14 and 16 were determined using X-ray diffraction and DSC methods, respectively. These data together with those previously reported by us for the dodecyl derivative were used to perform Monte Carlo simulations of these comb-like polymers. The results allowed to predict the solubility of different gases in the phase B of PAALA-*n*. The variation of both the unoccupied space and the excess chemical potential with the size of the penetrant were computed. An attractive interaction between the polymer matrix and the penetrants was found when small gases were considered. The results have been compared with those recently obtained for crystalline poly(α-alkyl-β-L-aspartate)s bearing short linear alkyl side chains.

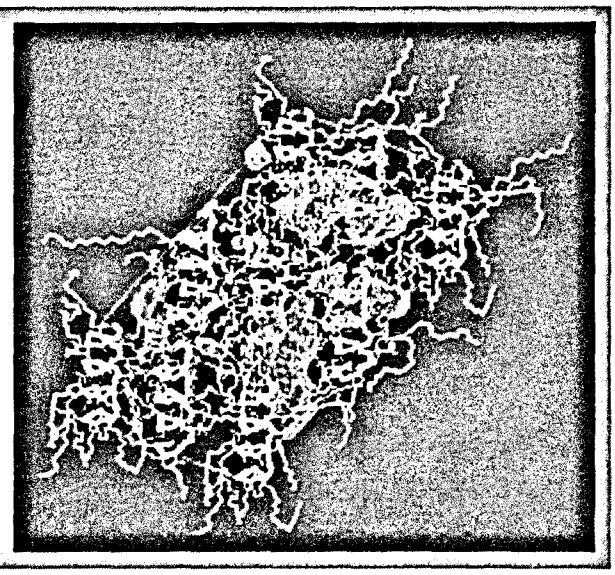

Unoccupied space for He penetrant in one of the microstructures generated for the phase B of PAALA-16.

On the Phase B of Comb-Like Poly(α-alkyl-β-L-aspartate)s: A Simulation of the Solubility of Small Penetrants

David Zanuy,[1] *Carlos Alemán,**[1] *Francisco López-Carrasquero,*[2] *María Eugenia Báez,*[2] *Montserrat García-Alvarez,*[1] *Manuel Laso,*[3] *Sebastián Muñoz-Guerra*[1]

[1] Departament d'Enginyeria Química, E.T.S. d'Enginyers Industrials de Barcelona, Universitat Politècnica de Catalunya, Diagonal 647, Barcelona E-08028, Spain
E-mail: aleman@eq.upc.es
[2] Grupo de Polímeros, Departamento de Química, Facultad de Ciencias, Universidad de Los Andes, Merida 5101A, Venezuela
[3] Department of Chemical Engineering, E.T.S. de Ingenieros Industriales, Universidad Politècnica de Madrid, José Gutierrez Abascal 2, Madrid E-28006, Spain

Introduction

Poly(α-alkyl-β-L-aspartate)s, abbreviated PAALA-*n* with *n* being the number of carbon atoms in the alkyl group, are nylon 3 derivatives with an alkoxycarbonyl group stereoregularly attached to every third backbone carbon atom of the repeating unit. These polymers are known to adopt helical conformations similar to the familiar α-helix characteristic of poly(α-amino acid)s for a wide variety of sizes and shapes of the side group.[1,2] Conversely, the degree of ordering that they attain in the solid state varies with the length of the alkyl side chain. PAALA-*n* with $n \leq 5$ crystallizes in hexagonal or tetragonal lattices composed of 13/4 or 4/1 helices[2–5] respectively, although other crystal forms based on 16/5 and 17/4 helices have been occasionally found.[5,6] On the other hand, those members bearing long linear alkyl side chains ($n \geq 12$) organize in lamellar structures lacking three-dimensional order but with chains retaining the 13/4 helical conformation characteristic of lower members of the series.[7] Those members bearing alkyl side chains of medium size (*n* = 6 and 8) display an intermediate depending on the history of the samples.[8]

Three structurally distinct phases, namely A, B and C, were observed in long side chain PAALA-*n* with *n* = 12,

  1022-1352/2001/0402-0564$17.50+.50/0

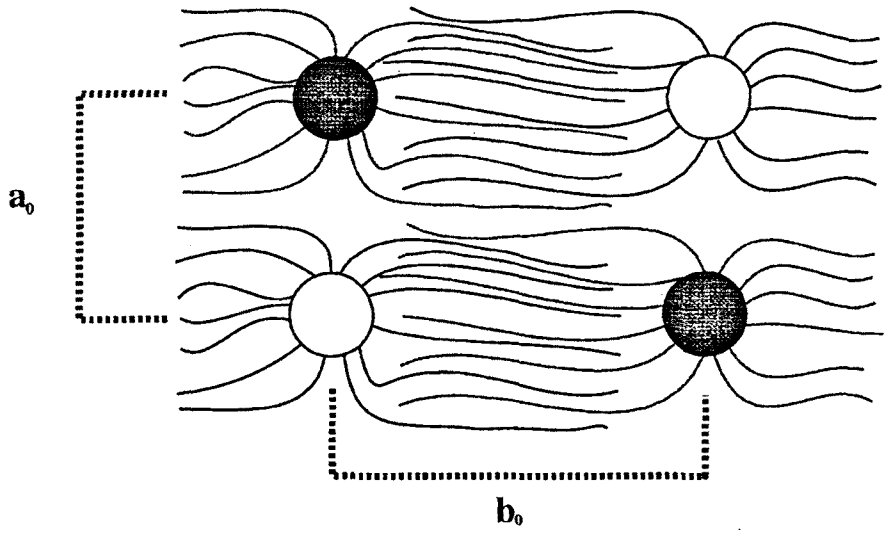

Figure 1. Schematic pictures of the biphasic structure of PAALA-n with $n \geq 12$.

18 and 22 upon increasing temperature, which were characterized by DSC and low-angle X-ray diffraction.[7] Phase B is the phase occurring at intermediate temperatures between phases A and C. Thus, it is obtained from phase A upon heating above T_1 and converts into phase C upon heating above T_2. In phase A main chain helices are arranged side-by-side in layers with side chains crystallized in a separated hexagonal lattice while in phase B the same arrangement is retained for the main chain helices but side chains are in the molten state. A rough representation of phase B is depicted in Figure 1. Finally, phase C has been interpreted to consist of an uniaxial arrangement of independent helices embedded in a matrix made up of side chains in a nearly coiled state. Phase B is particularly interesting because it is able to display thermotropic properties characteristic of cholesteric mesophases.[9] The PVT and structural properties of phase B were recently investigated using Monte Carlo simulations.[10]

The solubility of small penetrants, i.e. He, Ar and CH_4 in the hexagonal and tetragonal forms of PAALA-4 and PAALA-1 have been recently examined using the Widom's test-particle insertion method.[11] The results allowed both to characterize the distribution of the unoccupied space and to determine the solubility of such small gaseous penetrants in these systems. The ability of PAALA-n with $n \geq 12$ to generate layered supramolecular structures coupled with the high flexibility inherent to the polymethylene side chains makes these systems attractive to mimic both barrier synthetic composites and biological structures related with permeation processes. It is therefore encouraging to extend to these systems the simulation studies of gas solubility carried out previously on lower homologues. In this work we present a computational study about the behavior of a set of small gas molecules in the phase B of PAALA-12, PAALA-14 and PAALA-16 using molecular simulations.

To undertake this work experimental information about PAALA-14 and PAALA-16 is required. Thus, these polymers were synthesized for such purpose and their thermal properties and structure have been examined using DSC and X-ray diffraction methods, respectively. These experimental data together with those previously obtained for PAALA-12[7] have been used to obtain a number of microstructures using Monte Carlo calculations in periodic simulation cells. The excess chemical potentials have been predicted for seven different penetrants. The results have been compared with those previously obtained for poly(α-alkyl-β-L-aspartate)s bearing short linear alkyl side chains.[11]

Experimental Part

Methods

PAALA-14 and PAALA-16 were prepared by nonassisted anionic ring-opening polymerization of the corresponding optically pure (*S*)-4-(alkoxycarbonyl)-2-azetidinones. The synthesis of these monomers from L-aspartic acid has been performed as were reported in full detail for the monomers of other poly(α-alkyl-β-L-aspartate)s.[12] The methodology used for polymerization is that generally applied in the preparation of this family of polyamides.[13] Some data of the three polymers studied in this work are given in Table 1.

Calorimetric measurements were performed with a Perkin-Elmer Pyris-I DSC instrument operating under a nitrogen atmosphere and calibrated with indium. X-ray diffraction diagrams were recorded on flat films in a Statton-type camera using nickel-filtered copper radiation of wavelength 0.1542 nm and calibrated with molybdenum sulfide (d_{002} =

Table 1. Data of the poly(α-alkyl-β-L-aspartate)s studied in this work.

PAALA-*n*	Yield / %	$[\eta]$ / dL/g	$M_v \times 10^{-5}$ [a]	ρ / g/mL
12	74	2.70[b]	4.2	0.99
14	79	2.24[c]	4.4	1.01
16	73	3.46[b]	–	1.02

[a] Estimated by viscosimetry by using the Mark-Houwink equation reported for poly(γ-benzyl-α,L-glutamate).[7]
[b] Intrinsic viscosity measured at 25 °C in a mixture of chloroform and dichloroacetic acid (2:1).
[c] Intrinsic viscosity measured at 25 °C in dichloroacetic acid.

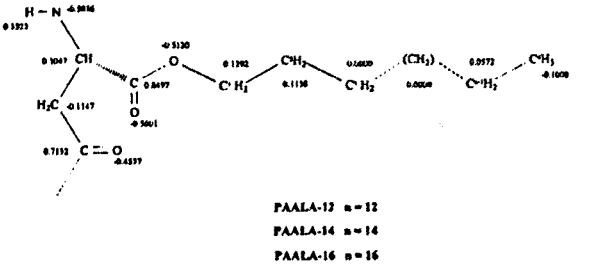

Figure 2. Electrostatic charges computed for PAALA-12, PAALA-14 and PAALA-16.

0.6147 nm). Polymer films were prepared by casting from chloroform. Thermodiffractograms were recorded from unoriented films in a Siemens D-500 diffractometer with Cu K_α radiation provided with a TPK-A Park heating stage and a scintillation counter.

Construction of the Simulated Models

The starting geometries for the layered structures of PAALA-12, PAALA-14 and PAALA-16 were built using the experimental information obtained in this work together with the data obtained from related previous molecular modeling studies.[4,8,10] The helical conformation used for the polymers under study was constructed using the conformational parameters obtained for other poly(α-alkyl-β-L-aspartate)s.[4] According to previous reported works the conformation is assumed to be a right-handed 13/4-helix with 3.25 residues per turn and an axial repeat length of c_o = 1.99 nm. The distance between the helices along the *a*- and *b*-axis (Figure 1) was fixed at the values calculated on the basis of X-ray diffraction data. According to all our previous results on poly(α-alkyl-β-L-aspartate)s the helices were placed in antiparallel.[2-6,8] On the other hand, the side chains were arranged to obtain a layered structure similar to that displayed in Figure 1. For this purpose, structural information obtained from our previous studies for PAALA-8[8] and PAALA-18[10] was used.

Generation of Microstructures

The microstructures required to study the solubility of penetrants in the phase B of PAALA-12, PAALA-14 and PAALA-16 were obtained using an advanced Monte Carlo sampling technique (Continuum Configurational Bias, CCB-MC).[14,15] This method was initially developed to be efficient in the study of dense systems. In addition to CCB moves, a small fraction (20%) of Metropolis moves were also used. It should be emphasized that both backbone conformations and positions of the helices within the unit cell were fixed according to the data provided by X-ray diffraction. The influence of backbone fluctuations on the solubility of small penetrants was recently investigated for PAALA-4 using CCB-MC simulations.[11] Results indicated that such movements can be neglected since the most important contribution to the solubility is provided by the flexibility of the polymethylene side chains.

The boxes used in the simulation of each polymer consist of four independent chains of 13 residues. Periodic continuation conditions and the minimum-image convention were applied to all simulations. MC simulations of 2×10^5 steps of NVT type, i.e. without varying the size of the box, were performed after 100000 steps of equilibration. For each polymer the simulation was performed at the temperature domain of phase B, which was characterized by DSC measurements. For each simulation 100 microstructures were recorded at 2000 steps intervals. The model used in the MC calculations assumed fixed bond lengths and bond angles. Accordingly, the torsional angles associated to the ethylene bonds of the side chains were the only degrees of freedom of the system. The AMBER force-field[16] was used to represent the electrostatic, van der Waals and torsional energies of the systems. Both methyl and methylene groups were described considering a model of united atoms, and their van der Waals energy was computed in the usual pairwise additive way using a Lennard-Jones 6–12 potential. Electrostatic charges were estimated by fitting the molecular electrostatic potential derived from quantum mechanical calculations to the classical one. The charge values resulting for the monomeric units of PAALA-12, 14 and 16 are given in Figure 2. Electrostatic interactions were evaluated using a standard Coulombic potential. Nonbonding interactions were truncated at 0.8 nm.

Measurement of the Unoccupied Space

The term "unoccupied space" in the context of gas transport refers to the volume not occupied by the atoms in the system.[17] Unoccupied space estimation was done by dividing the simulation box of every microstructure into a three-dimensional uniformly spaced grid. These grids consisted of 60180, 66300 and 71400 nodes for PAALA-12, PAALA-14 and PAALA-16, respectively. Then, a penetrant was centered in each node and the distance to the nearest atom of the polymeric matrix was measured. If this distance was larger than the sum of the van der Waals radii of the penetrant and the polymer atom, the node was identified as unoccupied. A set of seven simple penetrants was chosen: He, H_2, Ar, O_2, N_2, CH_4 and CO_2. The van der Waals radii used for the penetrants are displayed in Table 2, whereas those of the polymer atoms were taken from the AMBER libraries.[16]

Table 2. Lennard-Jones potential parameters for the penetrants.

Penetrant	R / nm	ε / kcal/mol
He	0.1290	0.0203
H_2	0.1475	0.0734
Ar	0.1725	0.2379
O_2	0.1790	0.2333
N_2	0.1849	0.1888
CH_4	0.1909	0.2943
CO_2	0.2243	0.3753

Widom's Test Particle Insertion Method

The infinite-dilution excess chemical potential of a penetrant sorbed in PAALA-12, PAALA-14 and PAALA-16 structures was estimated using the Widom's test particle insertion method.[18] In this method the chemical potential of species i in a frozen N-particle system relative to an ideal gas mixture is related to the potential energy of inserting a test-particle into the system at randomly chosen positions. The expression of the excess chemical potential is:

$$\beta \mu_i^{ex}(\rho, T) = -\ln \langle \exp(-\beta \phi_t) \rangle_N \quad (1)$$

where $\beta = 1/k_B T$, ϕ_t is the interaction energy between the test-particle and the N-particles of the system, and $\mu_i^{ex}(\rho,T)$ is the excess of chemical potential of species i at temperature T and number density $\rho = N/V$. The brackets $\langle ... \rangle_N$ denote the canonical ensemble average over the original N-particle system, i.e. without test-particle, at the T and of ρ interest. In order to improve the insertion efficiency the ensemble average $\langle \exp(-\beta \phi_t) \rangle_N$ has been defined as follows:[19]

$$\langle \exp(-\beta \phi_t) \rangle_N = \Sigma_{j=1} N_e (1/N_{Tj}) \Sigma_{j=1} N_{vj} \exp(-\beta \phi_{t,i}) \quad (2)$$

where N_{vj} is the number of sites without overlaps in the microstructure j, N_{Tj} is the total number of insertion for a given microstructure j assuming a uniform insertion density, and N_e is the total number of microstructures available for computing the ensemble averages.

We have used Eq. (2) to estimate the excess chemical potential. For this purpose, we have divided the microstructures into uniformly spaced grids. A penetrant particle was centered in each node if it was identified as unoccupied. Calculations were performed considering a spacing between consecutive nodes of 0.075 nm. Thus, this was considered as the most suitable value from a comparative study on PAALA-1 and PAALA-4 using spacings of 0.1, 0.075, 0.050 and 0.025 nm.[11] In order to normalize this biased sampling, the average of for each microstructure was weighted by $\omega_j = N_{vj}/N_{Tj}$ before being summed to yield the ensemble average. Interactions between the penetrants and the polymer were computed using a Lennard-Jones 6–12 potential and applying the standard Lorentz-Berthelot mixing rules. Such interactions were truncated at 0.8 nm. The force-field parameters for the penetrants are displayed in Table 2.

Results and Discussion

Structural Phases of PAALA-14 and PAALA-16 as a Function of the Temperature. Calorimetric and X-ray Diffraction Measurements

Figure 3a shows DSC thermograms of PAALA-14 and PAALA-16 registered at heating. The thermogram of PAALA-12 is also displayed in the Figure 3a for comparison. The broad peak T_1 was assigned to the melting of the paraffinic side chains and appeared at about 52 and

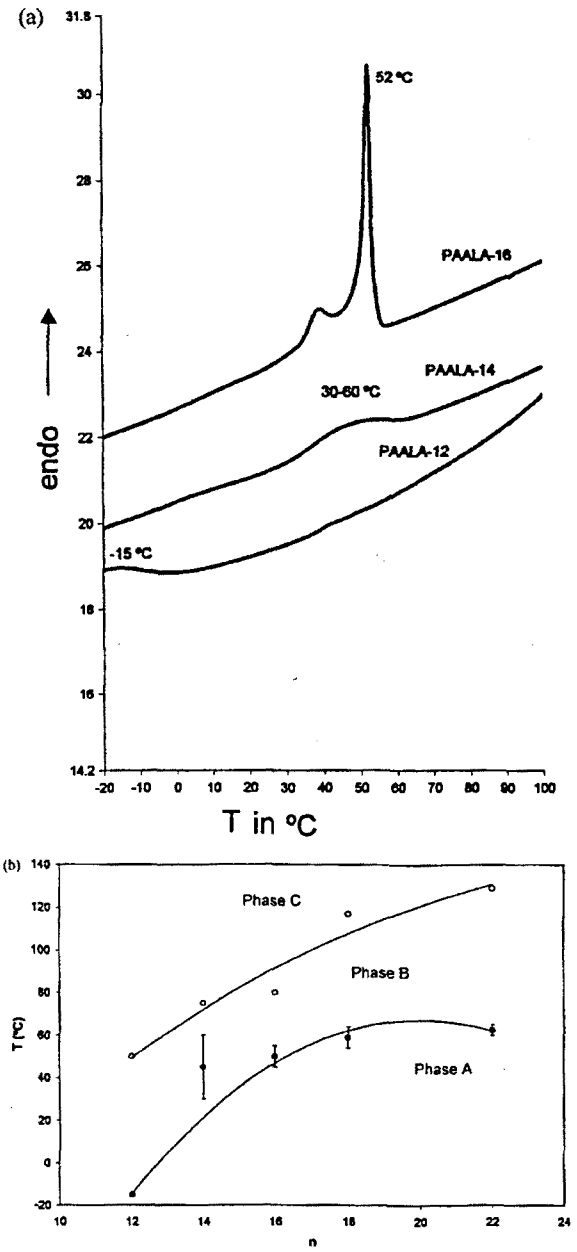

Figure 3. DSC thermograms of PAALA-14 and PAALA-16 (a). Temperature domains of phases A and B in the PAALA-n with n ranging from 12 to 22 (b).

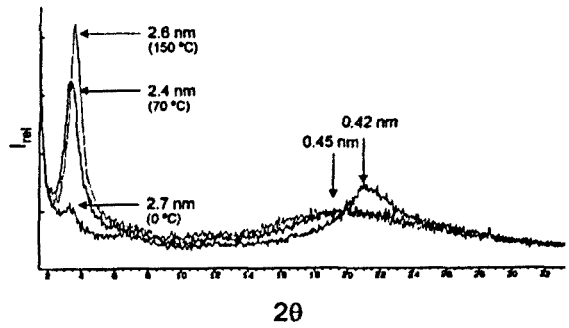

Figure 4. X-ray radial profiles of PAALA-14 film taken at the labeled temperatures.

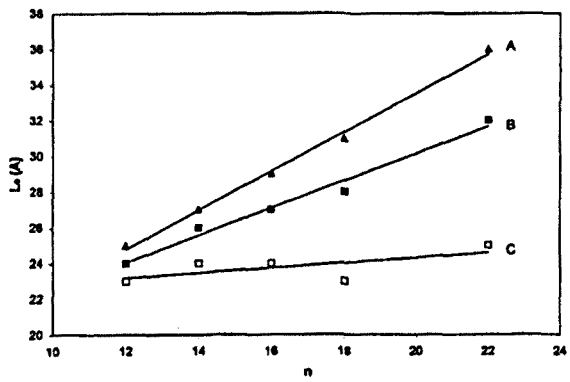

Figure 5. Interlayer distances in phases A, B and C of PAALA-*n* as a function of the number of carbon atoms contained in the alkyl side chain.

60 °C for PAALA-14 and PAALA-16, respectively. Accordingly, at such temperatures the phase A with helices immobilized by the crystallized side chains changes to phase B in which the side chains are mobile but the backbones retain their positions. The T_i measured for PAALA-14 and PAALA-16 are within the range of temperatures previously determined for PAALA-*n* with *n* = 12, 18 and 22.[7] Thus, T_i varies from −15 °C for PAALA-12 to 75 °C for PAALA-22 indicating that the thermal behavior of this family of polymers correlates with the length of the alkyl side chain. On the other hand, the two traces show a prominent peak above 300 °C which corresponds to the melting-decomposition of the polymer.[20] Figure 3b shows the temperature domains of phases A and B in the PAALA-*n* with *n* ranging from 12 to 22.

The biphasic structures of PAALA-14 and PAALA-16 were investigated at different temperatures by X-ray diffraction. The scattering profiles obtained for an unoriented sample of PAALA-14 at temperatures increasing from 0 to 150 °C are displayed in Figure 4. The diffraction patterns at temperatures below T_i are very similar to those previously obtained for PAALA-18 and PAALA-22.[8] The crystallization of the alkyl side chains is revealed by the presence of the discrete reflection with a spacing of 0.42 nm what is characteristic of phase A. The interlayer distance measured for PAALA-14 and PAALA-16 in phase A is 2.6 and 2.9 nm, respectively. At temperatures above T_i the interlayer distance decreases to 0.24 and 0.26 nm for PAALA-14 and PAALA-16, respectively, indicating the melting of the paraffinic side chains. The presence of the arced-shaped reflection with a spacing of 0.45 nm is consistent with the existence of the 13/4 helical conformation characteristic of poly(*α*-alkyl-*β*-L-aspartate)s bearing small linear side chains. Figure 5 shows the variation of the interlayer distances in the phases A and B of PAALA-*n* as a function of the number of carbon atoms included in the alkyl side chain.

Monte Carlo Simulations

The MC simulations of the phase B of PAALA-*n* with *n* = 12, 14 and 16 were performed under NVT conditions. The distance between the helices along the *b*-axes were taken from X-ray data (see the previous section), and along the *a*-axes were estimated from density data assuming a constant **c** parameter. Thus, the size of the boxes used in the simulations were [**a** = 2.46 nm, **b** = 4.60 nm, **c** = 1.99 nm], [**a** = 2.46 nm, **b** = 4.80 nm, **c** = 1.99 nm] and [**a** = 2.46 nm, **b** = 5.20 nm, **c** = 1.99 nm] for PAALA-12, PAALA-14 and PAALA-16, respectively. The temperatures chosen for the simulations were 10, 65 and 70 °C for PAALA-12, PAALA-14 and PAALA-16, respectively, which are well above the respective T_i of these polymers.

In order to investigate how fast the local properties change as the MC simulations run, the first and second degree bond autocorrelation functions ($f_{1;bcf}$ and $f_{2;bcf}$, respectively) were computed using the following expressions:[20]

$$f_{1;bcf}(n) = \langle v_i(j)\, v_i(j+n)\rangle_{ij} \tag{3}$$

$$f_{2;bcf}(n) = 3/2\, \langle (v_i(j)\, v_i(j+n))^2\rangle_{ij} - 1/2 \tag{4}$$

where the subscripts *i* and *j* correspond to the bonds and to the microstructures, respectively, and v_i is the unit vector of the *i*-th bond. The bond autocorrelation functions provide an estimation of how fast the tumbling motion of the bonds erases the memory of the previous local configuration. The decay of both $f_{1;bcf}(n)$ and $f_{2;bcf}(n)$ is shown in Figure 6. The bond autocorrelation function $f_{2;bcf}(n)$ drops below 0.42 for the three polymers after 2×10^5 steps. These results clearly indicate that local relaxation rates are similar for the three polymers. Accordingly, it should be expected a small dependence of these short-range properties with the length of the alkyl side chain for the PAALA-*n* with $n \geq 12$ synthesized so far since the largest length corresponds to *n* = 22. A measure of the

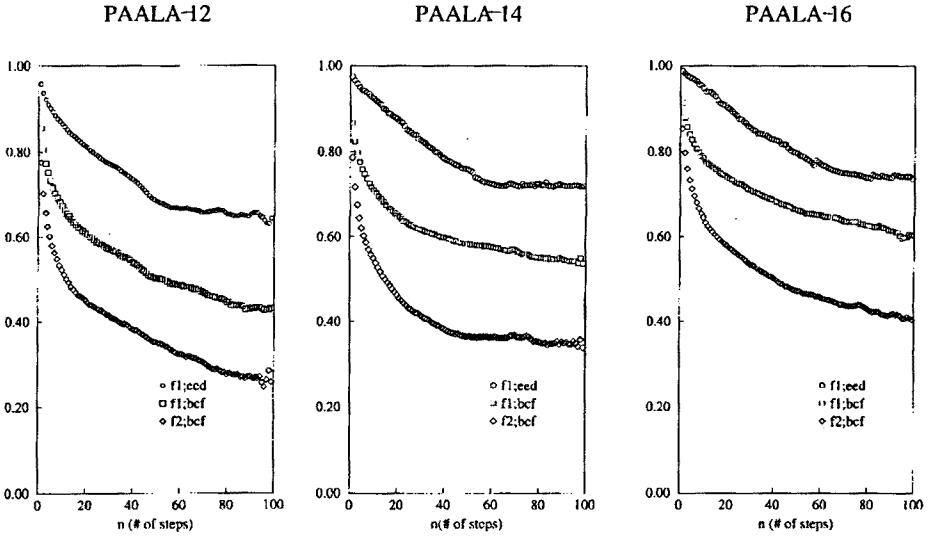

Figure 6. Bond autocorrelation functions ($f_{1;bcf}$ and $f_{2;bcf}$) and relaxation function of the end-to-end distance vector ($f_{1;eed}$) for the phase B of PAALA-12, PAALA-14 and PAALA-16.

Table 3. Fraction[a] in % of predicted unoccupied space for the different penetrants in the phase B of PAALA-12, PAALA-14 and PAALA-16. Results obtained for the hexagonal crystal form of PAALA-1 and PAALA-4 are also displayed for comparison.[b]

System	He	H_2	Ar	O_2	N_2	CH_4	CO_2
PAALA-12[c]	4.1 ± 0.6	3.1 ± 0.5	2.0 ± 0.4	1.7 ± 0.5	1.5 ± 0.4	1.4 ± 0.4	0.7 ± 0.3
PAALA-14	1.4 ± 0.3	0.8 ± 0.3	0.4 ± 0.2	0.3 ± 0.2	0.2 ± 0.1	0.2 ± 0.1	0.1
PAALA-16	0.8 ± 0.2	0.4 ± 0.2	0.2 ± 0.1	0.1	0.1	0.1	0.0
PAALA-12[d]	2.0 ± 0.3	1.4 ± 0.3	0.7 ± 0.2	0.6 ± 0.2	0.5 ± 0.2	0.4 ± 0.2	0.2 ± 0.1
PAALA-4	2.4 ± 0.3	–	0.7 ± 0.2	–	–	0	–
PAALA-1	0.6 ± 0.1	–	0.1 ± 0.1	–	–	0	–

[a] Averaged over the 100 microstructures generated by MC simulations.
[b] Taken from ref.[11]
[c] Using a simulation box of [**a** = 2.46 nm, **b** = 4.60 nm, **c** = 1.99 nm] (see text).
[d] Using a simulation box of [**a** = 2.46 nm, **b** = 4.40 nm, **c** = 1.99 nm] (see text).

side chain rotation, i.e. the spatial relaxation, has been provided by the relaxation function of the end-to-end distance vector:

$$f_{1;eed}(n) = [(r_N(n) - r_1(n))\,(r_N(0) - r_1(0))]/$$
$$[|r_N(n) - r_1(n)|\,|r_N(0) - r_1(0)|] \quad (5)$$

This provides a measure of the overall relaxation of the chains, i.e.the sampling efficiency. Results, which are also displayed in Figure 6, suggest also a similar relaxation for the three polymers. As it is expected the relaxation function $f_{1;eed}(n)$ decays much more slowly than the bond autocorrelation functions.[21] Thus, it drops to 0.63, 0.72 and 0.74 for PAALA-12, PAALA-14 and PAALA-16, respectively, after 2×10^5 steps. These values are similar to those obtained for C_{24} and C_{71} polybead chains using a similar CCB-MC method.[20,22] On the other hand, it should be emphasized that for the systems here investigated, one of the ends of the side chain is anchored to the helix backbone precluding a complete lost of either short- and large-range correlation. According to this and to the results displayed in Figure 6, the configurations obtained in the present simulations should be considered statistically independent. A very recent study for the phase B of PAALA-18 using CCB-MC showed that about 100 cycles are required to obtain a sufficiently decorrelated new system conformation.[10]

Measurement of the Unoccupied Space

The results derived from the analysis of the unoccupied space in all the generated microstructures are summarized for each penetrant in Table 3, which displays the amount of unoccupied space averaged over the 100 microstructures recorded for the three systems under study. Results obtained for the hexagonal crystal form of PAALA-1 and

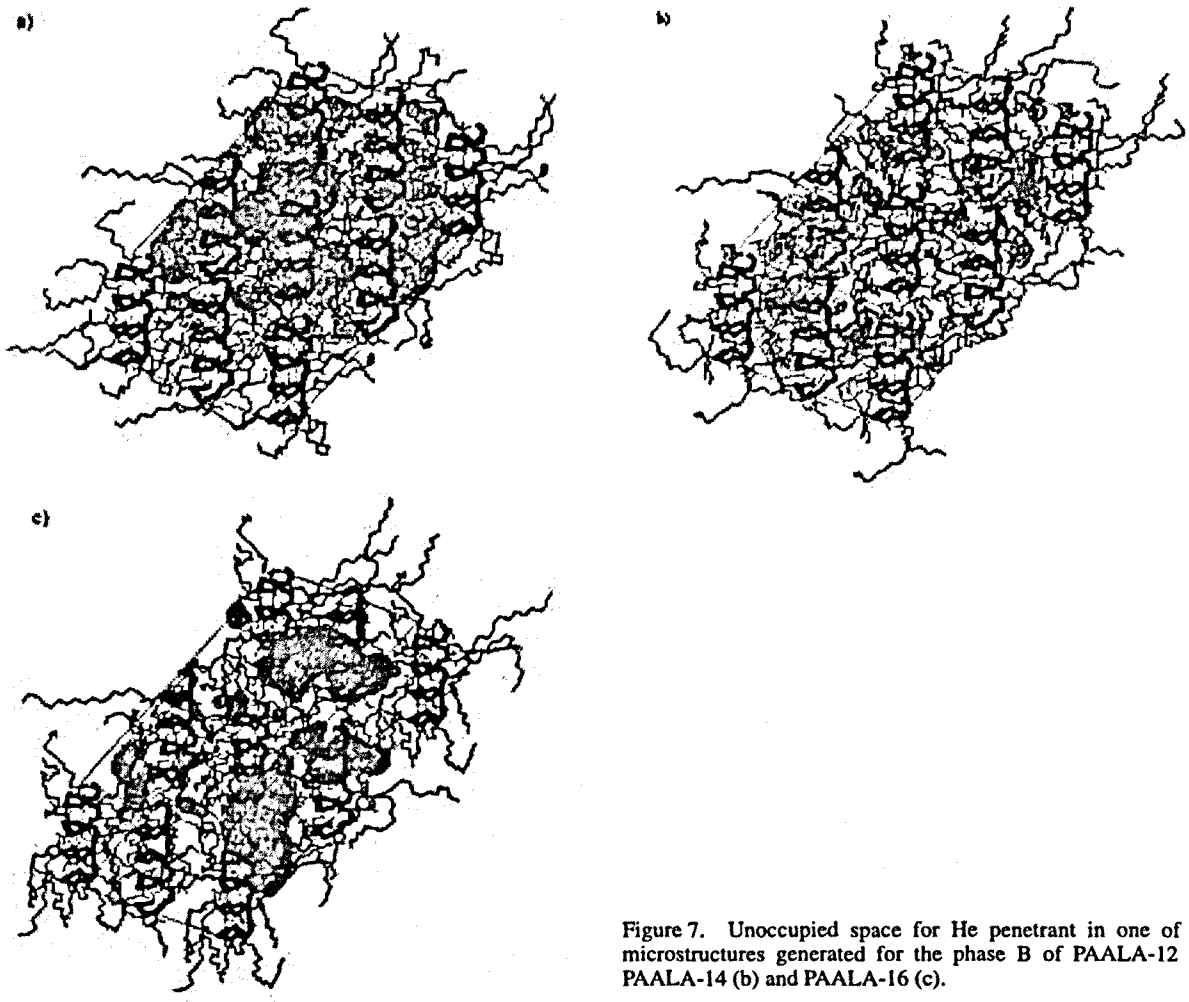

Figure 7. Unoccupied space for He penetrant in one of the microstructures generated for the phase B of PAALA-12 (a), PAALA-14 (b) and PAALA-16 (c).

PAALA-4 have been included for comparison.[11] It is worth noting that the amount of unoccupied space decreases with the length of the side alkyl group, even although the three systems are known to have very similar densities. This feature should be attributed to the presence of additional flexible dihedral angles. This means that, when degree of freedom increases, the interhelical region is more homogeneously filled. Inspection to the small standard deviations listed in Table 3 reveals that all the generated microstructures for a given polymer present a similar amount of unoccupied space.

The analysis of the results obtained for the different penetrants indicates that the unoccupied space decreases with the size of penetrant. Furthermore, it should be noted that the space available for the larger ones is almost negligible. These results are in agreement with those obtained for the crystalline PAALA-1 and PAALA-4 in which the unoccupied space calculated for penetrants larger than He was very small. Indeed, He and Ar also fit better in the hexagonal crystal form of PAALA-4 than in the phase B of PAALA-14 and PAALA-16 (Table 3).

An anomalous behavior is shown in Table 3 for the phase B of PAALA-12. Thus, the unoccupied space calculated for this compound is considerably large with respect to that of PAALA-14 and PAALA-16. This trend can be attributed to the lattice parameters used for the CCB-MC simulations of PAALA-12. Thus, it should be noted that the interlayer distance obtained from X-ray diffraction for PAALA-14 is 0.2 nm shorter than that of PAALA-16, this trend being also consistent with the values measured for PAALA-18 and PAALA-22. Nevertheless, a reduction of only 0.1 nm was observed for PAALA-12 with respect to PAALA-14. This value is probably due to the poor resolution of the X-ray diffractograms previously obtained for PAALA-12.[7] In order to get a deeper insight into this feature we perform CCB-MC simulations considering an interlayer distance of 2.20 nm, i.e. the box used in the simulations was [a =

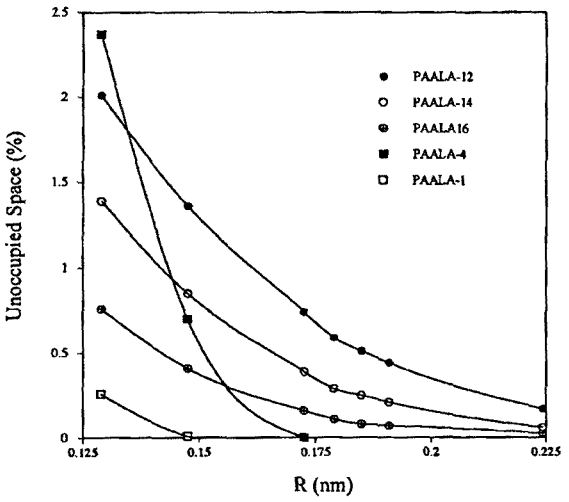

Figure 8. Variation of the unoccupied space (in %) versus the radii of the penetrants (in nm) for the phase B of PAALA-12, PAALA-14 and PAALA-16 as well as for the hexagonal crystal forms of PAALA-1 and PAALA-4.

2.46 nm, **b** = 4.40 nm, **c** = 1.99 nm]. The results derived from the analysis of the unoccupied space are included in Table 3. It is worth noting that the results reached from these calculations are in good agreement with those obtained for PAALA-14 and PAALA-16 showing a correlation between the amount of unoccupied space for a given penetrant and the length of the alkyl side chain. Thus, the goodness of the results achieved for PAALA-12 with an interlayer distance of 2.20 nm suggests that such distance was overestimated by about 0.1 nm in our previous work.[7] Figure 7 illustrates the unoccupied space for He in one microstructure of PAALA-12, PAALA-14 and PAALA.-16.

Figure 8 shows the variation of the unoccupied space with the size of the penetrants for the different polymers. As we can see in this figure, the best fit of the data for PAALA-12, PAALA-14 and PAALA-16 corresponds to an exponential function of the form: $V_{us} = a \times \exp(-b \times r)$. Thus, in order that the quantity of unoccupied space reaches a negligible value, i.e. V_{us} lower than ~0.25%, penetrants with van der Waals radii of approximately 0.16, 0.18 and 0.22 nm are needed for PAALA-16, PAALA-14 and PAALA-12, respectively. On the other hand, the variation of the unoccupied space with the size of the penetrant for the hexagonal crystal form of PAALA-4 (Figure 8) reveals a drastic reduction of the unoccupied space with the size of the penetrant. The different behavior between PAALA-4 and the polymers investigated in this work reflects the structural differences between the crystal and cholesteric phases of poly(α-alkyl-β-L-aspartate)s. Thus, in the phase B of PAALA-*n* with n = 12, 14 and 16 the alkyl side chains are melt giving place to a partially disordered state while in PAALA-4 the butyl side chains are crystallized. On the other hand, the profile displayed in Figure 8 for PAALA-1 shows a particular behavior. This is a very reasonably result since in this polymer the effect of the side chain is minimized and the results mainly depend on the peculiar helical conformation, i.e. PAALA-1 forms a 17/4 helix whereas the conformation adopted by PAALA-*n* with n = 4, 12, 14 and 16 is a 13/4 helix.

Excess Chemical Potentials

Table 4 shows the calculated excess chemical potentials for the three polymers investigated. Figure 9 shows the progress of the excess chemical potential of the He penetrant for the 100 generated microstructures of the three polymers. Each point corresponds to one application of Eq. (1) to one of the 100 microstructures generated from MC simulations whereas the solid lines display the mean values of the excess chemical potential up to this microstructure. It is worth noting that the lines drawn are running over the points indicating the convergence of the simulations. The results displayed in Figure 9 indicate that the interaction of the penetrant with the polymer matrix is favorable. The strength of these interactions is similar for PAALA-12 and PAALA-14 but decreases for PAALA-16. These results are consistent with the measured unoccupied spaces (Table 3). On the other hand, results listed in Table 4 indicate that the interactions between the polymer and the penetrants decrease with the size of the penetrant. Such interactions become repulsive

Table 4. Excess chemical potentials (kcal/mol) for the different penetrants in the phase B of PAALA-12, PAALA-14 and PAALA-16. Results obtained for the hexagonal crystal form of PAALA-1 and PAALA-4 are also displayed.[a]

System	He	H_2	Ar	O_2	N_2	CH_4	CO_2
PAALA-12[b]	-1.78	-1.54	-1.20	-1.07	-0.98	-0.91	-0.35
PAALA-14	-1.89	-1.55	-1.04	-0.84	-0.72	-0.61	0.16
PAALA-16	-1.56	-1.14	-0.48	-0.23	-0.07	0.06	0.97
PAALA-4	-1.62	-	-0.91	-	-	-	-
PAALA-1	-0.18	-	-	-	-	-	-

[a] Taken from ref.[11]
[b] Using a simulation box of [**a** = 2.46 nm, **b** = 4.40 nm, **c** = 1.99 nm] (see text).

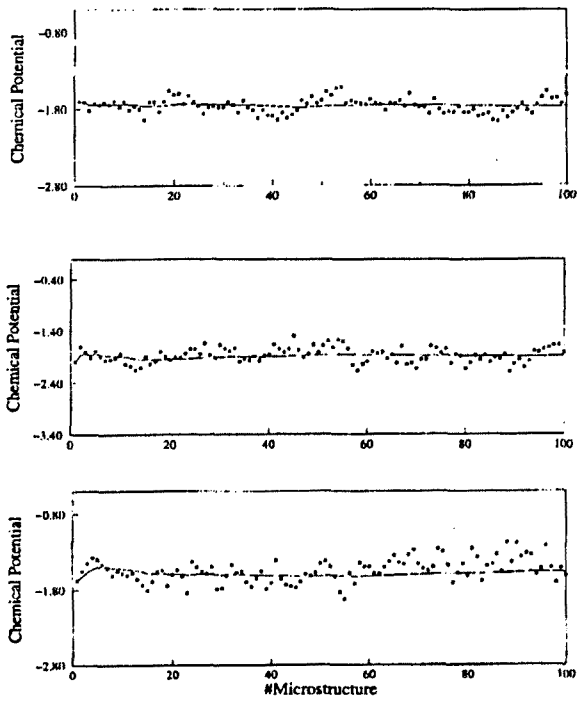

Figure 9. Convergence of the excess chemical potential (in kcal/mol) of He (solid line) calculated using the Widom's test-particle insertion method in the 100 microstructures obtained from MC calculations for the phase of PAALA-12 (a), PAALA-14 (b) and PAALA-16 (c).

for the larger penetrants (CH_4 and CO_2), as indicate the positive excess chemical potentials listed in Table 4. According to overall results, it can be concluded that small penetrants like He and H_2 present a considerable solubility in the phase B of PAALA-*n* with $n \geq 12$.

Table 4 also includes the excess chemical potentials predicted for the hexagonal crystal form of PAALA-4.[11] The results indicate that the solubility of small penetrants in this crystalline polymer is within the range of values predicted for the phase B of PAALA-12, PAALA-14 and PAALA-16. This feature is due to both the particular distribution of unoccupied space in PAALA-4[11]and the effect on Eq. (1) of the temperature used in the CCB-MC simulations. As was discussed before, crystalline PAALA-1 presents a particular situation which must be attributed to the intrinsic conformational characteristics of the 17/4 helix.

The solubility (S) is related with the excess of chemical potential by Eq. (6):

$$S = \exp(-\mu^{ex}/RT) \quad (6)$$

with R being the gas constant. The simulated solubilities for PAALA-12, PAALA-14 and PAALA-16 derived from the application of Eq. (6) are represented in Figure 10

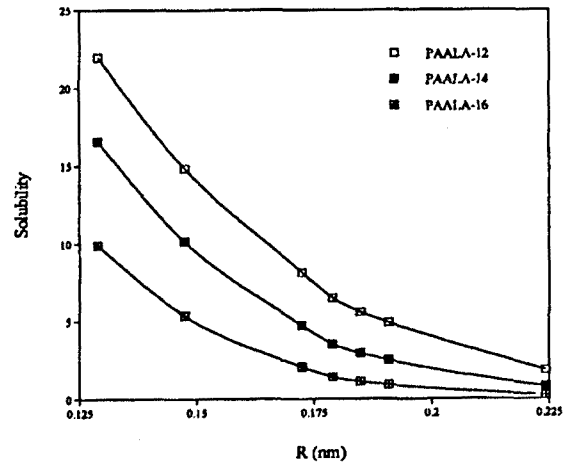

Figure 10. Variation of the solubility versus the radii of the penetrants (in nm) for the phase B of PAALA-12, PAALA-14 and PAALA-16.

against the size of the penetrants. It is worth noting that a similar profile to that presented above in Figure 8 is obtained. These results indicate that the solubility of small gas penetrants in the phase B of PAALA-12, PAALA-14 and PAALA-16 depends on the amount space available to the penetrants, which in its turn depends on their size.

It is worth noting that results obtained for compounds under study are in discrepancy with respect to those reported for amorphous polyethylene.[23,24] Thus, it was observed that gas solubility in amorphous polyethylene increases as the size of the penetrant increases. This trend was related with the strengthening of the enthalpic interactions between the penetrant and the polymeric matrix. However, as was described along this work, the biphasic structure of the phase B of PAALA-*n* with $n \geq 12$ is very different from that of amorphous polyethylene. In order to explain better this discrepancy as well as to validate the results described in this paper, experimental work and additional simulations are in progress.

Conclusions

The structural and thermal properties of PAALA-14 and PAALA-16 have been investigated using X-ray diffraction and DSC methods. These data together with those available on members containing 12, 18 and 22 atoms of carbon in the linear alkyl side chains provides a complete picture of this family of comb-like polyamides. A computational study of the phase B of PAALA-*n* with $n = 12$, 14 and 16 has been performed in order to investigate their utility in permeation processes. CCB-MC simulations have been used for the calculation of unoccupied spaces and solubilities of small gas molecules. The variation of the unoccupied space with the size of the penetrant for

the phase B of PAALA-12 and PAALA-16 fits a smooth exponential plot. This behavior differs from that predicted for the hexagonal crystal form of PAALA-4 which shows a much more drastic variation. On the other hand, the calculated excess chemical potentials reveal favorable interactions between the polymer matrix and all the smaller investigated penetrants. The most significant result provided by this study is that penetrants like He, H_2 and Ar present a considerable solubility in the phase B of PAALA-12, PAALA-14 and PAALA-16.

Acknowledgement: This work was supported by *DGICYT* (PB96-0490), *CONICIT* (G-97000594) and *CDCHT-ULA* (C831-97-08-B). D. Z. acknowledges the support of the *Ministery of Education of Spain* for the award of a scholarship. Authors thank to *CESCA* and *CEPBA* for computational facilities. Authors are indebted to *Salvador Leon* for assistance in the preparation of the MC simulations.

Received: October 13, 1999
Revised: May 17, 2000

[1] J. M. Fernández-Santín, J. Aymamí, S. Muñoz-Guerra, A. Rodríguez-Galán, J. A Subirana, *Nature* **1984**, *311*, 53.
[2] S. Muñoz-Guerra, F. López-Carrasquero, J. M. Fernández-Santín, J. A. Subirana, in: "*Encyclopedia of Polymeric Materials*", J. C. Salomone, Ed., CRC, Boca Raton, Fl, 6, p. 4694.
[3] F. López-Carrasquero, C. Alemán, M. García-Alvarez, A. Martínez de Ilarduya, S. Muñoz-Guerra, *Makromol. Chem. Phys.* **1995**, *196*, 253.
[4] J. J. Navas, C. Alemán, F. López-Carrasquero, S. Muñoz-Guerra, *Macromolecules* **1995**, *28*, 4487.
[5] F. López-Carrasquero, M. García-Alvarez, J. J. Navas, C. Alemán, S. Muñoz-Guerra, *Macromolecules* **1996**, *29*, 8449.
[6] M. García-Alvarez, S. León, C. Alemán, J. L. Campos, S. Muñoz-Guerra, *Macromolecules* **1998**, *32*, 124.
[7] F. López-Carrasquero, S. Montserrat, A. Martínez de Ilarduya, S. Muñoz-Guerra, *Macromolecules* **1995**, *28*, 5535.
[8] J. J. Navas, C. Alemán, F. López-Carrasquero, S. Muñoz-Guerra, *Polymer* **1997**, *38*, 3477.
[9] F. López-Carrasquero, *PhD dissertation*, Universitat Politècnica de Catalunya, 1995.
[10] S. León, C. Alemán, S. Muñoz-Guerra, M. Laso, *Comput. Theor. Polym. Sci.* **2000**, *10*, 177.
[11] D. Zanuy, S. León, C. Alemán, S. Muñoz-Guerra, *Polymer* **2000**, *41*, 4169.
[12] M. García-Alvarez, F. López-Carrasquero, E. Tort, A. Rodríguez-Galán, S. Muñoz-Guerra, *Synth. Commun.* **1994**, *24*, 745.
[13] F. López-Carrasquero, M. García-Alvarez, S. Muñoz-Guerra, *Polymer* **1994**, *35*, 4502.
[14] J. J. de Pablo, M. Laso, U. W. Suter, *J. Chem. Phys.* **1992**, *96*, 6157.
[15] J. J. de Pablo, M. Laso, U. W. Suter, *Macromolecules* **1993**, *26*, 6180.
[16] S. J. Weiner, P. A. Kollman, D. A. Case, U. C. Singh, C. Ghio, G. Alagona, S. Profeta, P. Weiner, *J. Am. Chem. Soc.* **1984**, *106*, 765.
[17] S. Arizzi, P. H. Mott, U. W. Suter, *J. Polym. Sci., Part B: Polym. Phys.* **1992**, *30*, 415.
[18] B. Widom, *J. Phys. Chem.* **1982**, *86*, 869.
[19] T. R. Cuthbert, N. J. Wagner, M. E. Paulaitis, *Macromolecules* **1997**, *30*, 3058.
[20] E. Leontidis, J. J. de Pablo, U. W. Suter, *Adv. Polym. Sci.* **1994**, *116*, 283.
[21] K. Kremer, G. Grest, *J. Chem. Phys.* **1990**, *92*, 5057.
[22] E. Leontidis, B. M. Forrest, A. H. Widmann, U. W. Suter, *J. Chem. Soc., Faraday Trans.* **1995**, *91*, 2355.
[23] J. G. Curro, K. G. Honnell, J. D. McCoy, *Macromolecules* **1997**, *30*, 145.
[24] J. L. Budzien, J. D. McCoy, D. H. Weinkauf, R. A. La Violette, E. S. Peterson, *Macromolecules* **1998**, *31*, 3368.

Prefacio

El autor de esta memoria únicamente ha obtenido una parte de los resultados presentados en esta sección. Estos corresponden específicamente al modelado de la estructura y al estudio teórico de la solubilidad de gases.

VIII.8. "Permeation properties of the estereoregular *nylon*-3 analog, Poly(α-*n*-hexyl-β-L-Aspartate)"

Compañ, V.; Zanuy, D.; Andrio, A.; Morillo, M.; Alemán C.; Muñoz-Guerra, S. *Macromolecules*

(Enviado, febrero 2001)

PERMEATION PROPERTIES OF THE STEREOREGULAR NYLON-3 ANALOG, POLY(α-*n*-HEXYL-β,L-ASPARTATE)

Vicente Compañ,[1] David Zanuy,[2] Andreu Andrio, Marga Morillo[2]
Carlos Alemán,[2] and Sebastián Muñoz-Guerra*[2]

[1]Departament de Ciencies Experimentals. Universitat Jaume I
12080 Castellón. Spain

[2]Departament de'Enginyeria Química, Universitat Politécnica de Catalunya
ETSEIB, Diagonal 647, 08028 Barcelona, Spain

Corresponding author: munoz@eq.upc.es

ABSTRACT

The permeability of thin films of the α-helix-like poly(β-peptide), poly(α-*n*-hexyl-β, L-aspartate), to O_2, N_2 and CO_2 penetrants was measured by diffusion experiments at temperatures ranging between 20 and 80 ºC. P and D coefficients were found to be higher for CO_2 and both parameters increased with temperatures for the three gases. Solubilities of N_2 and O_2 appeared to be practically independent on temperature whereas that of CO_2 largely decreased upon heating. Solubilities of the three penetrants in the polypeptide were calculated by using advanced Monte Carlo methods specifically developed for the simulation of dense polymers. The structure of the polymer was modelled and optimized in a quasi-hexagonal array of 13/4 helices with an average interchain distance of 14.6 Å. Values predicted at low temperature were in satisfactory agreement with experimental data. At high temperatures significant discrepancies were found for N_2 and O_2 which revealed the limitation of our simulation method method to evaluate accurately the influence of temperature on the distribution of the unoccupied space.

INTRODUCTION

Poly(α-alkyl-β,L-aspartate)s constitute a family of poly(β-peptide)s able to adopt regular folded arrangements similar to the well-known α-helix characteristic of poly(α-peptide)s and proteins.[1,2] These polymers may be also considered as nylon 3 analogs bearing an alkoxycarbonyl side group stereoregularly attached to the β carbon atom of the main chain:

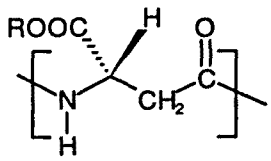

The structure of members with linear alkyl side groups, henceforth abbreviated PAALA-*n*, where *n* stands for the number of carbons contained in the alkyl chain, has been systematically studied from methyl (*n* =1) up to docosyl (*n* = 22).[1-5] The conformation preferred by these poly(β-peptide)s consists of a right-handed helix stabilized by intramolecular hydrogen bonds with 13 residues in four turns, *i.e.* the 13/4 helix. The length of the alkyl side group determines the type of arrangement adopted by the PAALA-*n* helices in the solid state. On one side, PAALA-*n* with $n \leq 4$ tend to crystallize in a tridimensional array of helices with the alkyl side groups forming part of the crystal lattice[2-4] (Figure 1a). On the other side, comb-like PAALA-*n* with $n \geq 12$ form layered structures with main chain helices and alkyl side chains distributed in two separate crystalline phases[5] (Figure 1b). PAALA-*n* with side chains of intermediate size, which are those with n = 6, 8 and 10, display a rather ambiguous behavior consistent with the structural discontinuity existing between short and long alkyl side chain polymers.[5,6] In fact, they tend to be arranged in a two-dimensional array of side-by-side packed helices with the alkyl chains remaining in the molten state.

The structure of poly(α-*n*-hexyl-β,L-aspartate), *i.e.* PAALA-6, has been examined by X-ray diffraction, solid state NMR and computer simulations.[5,6] X-ray diffraction of uniaxially oriented films of this polymer revealed the existence of an equatorial spacing at ~1.7 nm that could be associated to the lateral dimension of a

rough hexagonal array of 13/4 helices. CP-MAS ^{13}C NMR spectra recorded at temperatures between 25 and 80 ºC were in accordance with the presence of the helical conformation along the whole interval of examined temperatures and did not show differences indicative of the occurrence of structural transitions upon heating. Furthermore, molecular mechanics calculations indicated that the hexyl side chains are unable either to crystallize separately or to pack efficiently in a tridimensional lattice.[6] As a result, the structure of PAALA-6 was envisaged as an approximate hexagonal packing of 13/4 helices lacking axial register and having the hexyl side chains in a disordered arrangement.

The solubility and transport of penetrant molecules in semicrystalline polymers have become a topic of interest in the last years. In this type of polymers, the nature, amount and distribution of the amorphous phase are known to be the factors determining largely the permeability of the material. Permeation properties have been investigated for a number of partially ordered polymers using both experimental and computational methods.[7-14] In this context, PAALA-*n* with medium or large values of *n* deserve particular attention since they form supramolecular structures composed of two well delineated phases with completely different characteristics:[15] Since a different response to external stimuli may be expected for each phase, these systems open the door to the the control of certain properties, which like permeability, depend on the microscopical structure and morphology of the material. However no experimental determination of gas transport in biphasic poly(β-peptide)s, or even in the more widely known biphasic poly(α-peptide)s, has been performed so far. Recently we have carried out some theoretical studies on the solubility of small molecules in polymeric matrices of PAALA-*n*. We specifically examined the solubility of gaseous penetrants in the crystal structures of PAALA-1 and PAALA-4[12] as well as in the layered structures of PAALA-*n* with $n \geq 12$.[13,14] Results obtained from these computational studies predicted that small penetrants are considerably soluble in the latter compounds but that a much lower solubility should be expected in PAALA-*n* with $n \leq 4$. No similar study on the behavior of PAALA-*n* bearing side chains of intermediate size has been carried out yet. The main objective of the present work is to evaluate the transport properties of simple penetrants in films of PAALA-6 and to correlate the observed behavior with the microscopic structure of the polymer. For this, the permeation coefficients of N_2, O_2

and CO_2 gases are firstly measured by membrane diffusion experiments and then the solubility of these penetrants in PAALA-6 are calculated by computational methods using suitable modeled molecular structures.

METHODS

Experimental methods

Materials and Intermediate Products. All chemicals were obtained commercially from either Aldrich or Merck. They were analytical grade or higher and used without further purification. Solvents to be used under anhydrous conditions were dried by standard methods. Poly(α-benzyl-β,L-aspartate) (PABLA) was obtained by anionic ring opening polymerization of 4(*S*)-4-benzyloxy carbonyl-2-azetidinone, as reported elsewhere.[16] This optically pure β-lactame was synthesized from natural L-aspartic acid by a well established esterification-cyclation sequence of reactions.[17]

Polymer Synthesis. PAALA-6 was obtained by transesterification of PABLA with 1-hexanol in the presence of titanium tetrabutoxide, as it is shown in Scheme I. This procedure is of general validity for the preparation of PAALA-*n* and a detailed account of the method will be published in a near future. In brief, a mixture of finely powdered PABLA and Ti(BuO)$_4$ suspended in an excess of 1-hexanol was heated at 180 ºC under magnetically stirring and a nitrogen atmosphere. ^{1}H NMR analysis revealed that the replacement of the benzyl group by the *n*-hexyl group was complete after 25 min of treatment. The final reaction mixture solution was left to cool down and then added with methanol to precipitate the alkylated polymer. PAALA-6 was recovered by filtration and repeatedly washed with methanol. For purification, the polymer was dissolved in chloroform added with a few drops of trifluoroacetic acid and then precipitated by addition of methanol. Synthesis data together with some of the most relevant characteristics of PAALA-6 are given in Table 1.

Permeation measurements. PAALA-6 films to be used for permeation experiments were prepared by hot-pressing with a thickness of approximately 150-200 μm in a Specac accessory (CTFM-P/N 15620). Permeation measurements were carried out

in the experimental device schematically represented in Figure 2. The apparatus consists of a cell with two chambers separated by the membrane, which is immersed in a computer controlled thermostatic bath. Vacuum is made in both chambers by means of a Leybold AG vacuum pump model Trivac D 1,6 B that can reach $4x10^{-4}$ mbar. Pressures were measured using capacitive sensors. Leybold DI 2000 sensor (S1) and Tylan General CDHD45-11 sensor (S2), with an accuracy of 0.15% of reading, were used in the upstream- and downstream chambers, respectively. Nupro pneumatic electrovalves, model SS-4BK-1C, controlled from a computer program were used. This program also controls temperature, vacuum and gas filling of the upstream chamber and calculates both permeability and diffusion coefficients using the pressured data of the chambers. The program automatically repeats this job for each temperature and pressure of the upstream chamber. Before measurements were performed, the system was vacuum calibrated by measuring the inlet of air into the downstream chamber. Keeping all the valves open except valve 5, high vacuum was made for 24 hours in both chambers. Then valves 2 and 3 were closed and valve 5 was opened allowing the gas to fill the reservoir up to a pressure near to that used for the experiment. Then valve 1 was suddenly closed and valve 3 opened, and this time taken as zero reference. The evolution of the pressure in the downstream chamber with time was monitored by the transducer pressure sensor CDHD45-11. The volume in the downstream chamber was measured by using the helium expansion technique. The value of this volume was fixed at 33.5 mL in order to get downstream pressures sufficiently low in relation to the pressure of the upstream chamber. In all experiments, the relation $p_l<0.01p_0$ was satisfied. The permeation measurements were performed in the temperature range 20 ºC – 80 ºC, using steps of 10 ºC for pressure differences of 0.5, 1 , 2, 4 and 7 atm.

Computational methods

Monte Carlo Simulations. The atomistic structure of PAALA-6 was reinvestigated using an advanced Monte Carlo (MC) sampling technique (Continuum Configurational Bias, CCB-MC).[19,20] This method has been recently adapted to the study of dense polymers with either partially or completely ordered structures. The method has been implemented into a computer program denoted MCDP (Monte

Carlo simulations of Dense Polymers),[21] which has been optimized and parallelized to obtain a maximum computational efficiency. This strategy has been successfully used in the structural study of PAALA-*n* with *n* = 8, 12, 14, 16 and 18.[13,14,21] In addition to CCB moves, a small fraction of Metropolis moves (20%) were also used in all the simulations.

The box used in the simulations of PAALA-6 consists of eight independent chains arranged in antiparallel, as schematically represented in Figure 3. Periodic boundary continuation conditions and the minimum-image convention were applied to all simulations. The initial atomic coordinates were taken from our previous molecular mechanics study, in which an atomistic model was proposed for PAALA-6 on the basis of energy minimization calculations.[6] Such a model was compatible with the experimental information gained from X-ray and NMR diffraction data: *i*) the chain backbone is in a 13/4 helical conformation, and *ii*) the helices are packed in a quasi-hexagonal array lacking axial register. The torsional angles of the 13/4 helix were kept fixed at the following values: φ= 146.2º, ξ= -59.8º and ψ= 128.8º. This agrees with the experimental observation that this helical conformation is retained in the solid at high temperatures[5] and also in solution.[22]

MC simulations of both *NPT* and *NVT* type, *i.e.* with and without varying the size of the box respectively were performed at temperatures of 20 ºC and 80 ºC. All the *NVT* simulations at room temperature were run for a total of $7.5 \cdot 10^5$ steps and the coordinates were saved every 2500 steps after $2.5 \cdot 10^5$ steps of equilibration. *NPT* simulations at 20 ºC were stopped when both the energy and the cell parameters were equilibrated. Simulations at 80 ºC were run for a total of $6 \cdot 10^5$ steps, the coordinates being saved every 2500 steps after $1 \cdot 10^5$ steps of equilibration. Accordingly, 200 microstructures were recorded and analyzed for each simulation of *NVT* type.

The AMBER force-field[23] was used to represent the electrostatic, van der Waals and torsional energies of the system. Both methyl and methylene groups were described considering a model of united atoms and their van der Waals energy was computed in the usual pairwise additive way using a Lennard-Jones 6-12 potential. Electrostatic charges were determined by fitting the molecular electrostatic potential derived from quantum mechanical calculations to the classical one.

Electrostatic interactions were evaluated using a standard Coulombic potential. Nonbonding interactions were truncated at 8 Å.

Measurement of the Unoccupied Space. The volume not occupied by the polymer chains was estimated by dividing the simulation box of every microstructure into a three-dimensional uniformly spaced grid. Then, a penetrant was centered in each node and the distance to the nearest atom of the polymeric matrix was measured. If this distance was larger than the sum of the van der Waals radii of the penetrant and the polymer atom, the node was identified as unoccupied. Calculations were performed considering a spacing between consecutive nodes of 0.50 Å. The O_2 and N_2 penetrants were described as simple spheres whereas a model including explicitly the three atoms was used to represent CO_2.[7] The dimensions estimated for the three penetrants are listed in Table 2.

Solubility Calculations. Solubility, S_o, gives the concentration of the gas in a volume element of the polymer that is in equilibrium with the outside gas at a given pressure. The determination of S_0 is based on the calculation of the interaction energy of the penetrant with the polymer in which it has been inserted at random. Such energy is used for obtaining the excess chemical potential (μ_{ex}), S_o, which is related to μ_{ex} by the following equation:

$$S_o = \exp(-\mu_{ex}/RT) \qquad (1)$$

The relation between the calculated solubility, S_o, and the experimental solubility coefficient S, in a unit of $cm^3(STP)(cm^3Pa)^{-1}$ is written by:[24]

$$S = (T_o/ T\, p_o)\, S_o \qquad (2)$$

where $T_o = 273.15$ K, T is the temperature of measurement and $p_o = 1.013 \cdot 10^5$ Pa.

The infinite-dilution μ_{ex} of a penetrant sorbed in PAALA-6 was estimated using the Widom´s test particle insertion method.[25] In this method the chemical potential of species *i* in a frozen N-particle system relative to an ideal gas mixture is related to the potential energy of inserting a test-particle into the system at randomly chosen positions. The expression of μ_{ex} is:

$$\beta \mu_{ex}(\rho, T) = - \ln \langle \exp(-\beta \phi_t \rangle_N \qquad (3)$$

where $\beta = 1/k_bT$, ϕ_t is the interaction energy between the test particle and the N particles of the system, and $\mu_{ex}(\rho, T)$ is the excess chemical potential of species *i* at temperature T and number density $\rho=N/V$. The brackets $\langle ....\rangle_N$ denote the canonical ensemble average over the original N-particle system at the T and ρ of interest. In order to improve the insertion efficiency the ensemble average $\langle \exp(-\beta \phi_t \rangle_N$ has been defined as follows:

$$\langle \exp(-\beta \phi_t \rangle_N = \Sigma_{j=1,N_\theta} (1/N_{T,j}) \Sigma_{i=1,N_{v,j}} \exp(-\beta \phi_{t,i} \rangle \qquad (4)$$

where $N_{v,j}$ is the number of sites without overlaps in the microstructure *j*, $N_{T,j}$ is the total number of insertions for a given microstructure *j* assuming a uniform insertion density, and N_θ is the total number of microstructures available for computing the ensemble of averages.

In order to evaluate Equation 4, the penetrant was centered at each node identified as unoccupied. Interactions between the penetrants and the polymer were computed using the Lennard-Jones 6-12 potential and applying the Lorenz-Berthelot mixing rules. Such interactions were truncated at 8 Å. The force-field parameters for the different penetrants considered in this study are displayed in Table 2.

RESULTS

Permeation Measurements. The transport of gases through membranes is generally expressed in terms of the apparent permeability coefficient P and the apparent diffusion coefficient D. Illustrative plots showing the variation with time of the pressure in CO_2 of the down-stream chamber, at 25º C and different pressures in the up-stream chamber are represented for PAALA-6 in Figure 4. As usual, the curves present a transient state at short times followed by steady- state transport conditions at longer times. The intercept of the extrapolated steady part of the curve with the time axis gives the time-lag, θ. This parameter is related to D, as indicated by Barrer,[26]

$$D = \frac{L^2}{6\theta} \qquad (5)$$

where L is the thickness of the film. Under conditions of steady-state permeation, the apparent permeability can be evaluated by means of the following expression,[27]

$$P = \frac{273}{76} \cdot \frac{V \cdot L}{A \cdot T \cdot p_0} \cdot \frac{dp(t)}{dt} \qquad (6)$$

where V and p are the volume and pressure of the downstream chamber, respectively, A is the effective area of the film, p_0 is the pressure in cm of Hg of the penetrant gas in the upstream chamber and T is the absolute temperature. P and D were found to be quite well reproducible so that the standard deviations for three consecutive measurements were ±2% and ±10%, respectively.

The dependence of the permeability coefficient of O_2, N_2 and CO_2 on temperature through PAALA-6 films, at p_0 = 1 atm, is represented in Figure 5a. Similar plots have been obtained for other pressures. This figure shows clearly that the permeability coefficient of the gases increases in the following order $P(CO_2) > P(O_2) > P(N_2)$ at any temperature, the former being much larger than the other two. This result is in accordance with the general trend observed for other polymers.[28] The temperature dependence of the diffusion coefficient of O_2, N_2 and CO_2 are shown in Figure 5b. As expected, D increases steadily with temperature and show the same relative order as the the permeability coefficient with $D(CO_2) > D(O_2) > D(N_2)$. Contrary to what occurs in other many systems, the value of the apparent diffusion coefficient of O_2, N_2 and CO_2, in PAALA-6 films at low temperatures are very close to each other. This is also in contrast to the behavior observed for the permeability coefficient, which appears to be significantly larger for CO_2 than for O_2 and N_2. Comparison of results plotted in figures 5a and 5b suggests that the permeability of CO_2 in PAALA-6 is mainly governed by the solubility of the gas in the membrane.

The apparent solubility coefficient, S, is defined as,

$$S = \frac{P}{D} \qquad (7)$$

The S coefficients calculated for the three gases at p = 1 atm are plotted in Figure 5c for the considered interval of temperatures. It is seen that they follow the same relative order as the permeability and diffusion coefficients, *i.e.* $S(CO_2)>$ $P(O_2)>$ $S(N_2)$, but showing larger differences between them. The solubility of the three gases in the films decreases when the temperature increases, but the variation is much greater for CO_2 than for $S(N_2)$ and $S(O_2)$. Whereas at 20 ºC the coefficients of these two gases are about twenty and ten times smaller than that of CO_2, at 80 ºC such ratios become reduced to one sixth and one third, respectively .

The results obtained with PAALA-6 films show a logical correspondence between the permeation properties of the polymer and the the physical characteristics of the diffusing molecule. On one side it is apparent that both the permeability and the diffusion coefficient decrease as the size of the diffusing molecule increases. On the contrary, the solubility coefficient increases with increasing molecular dimensions. These tendencies are in accordance with the general behavior observed for other semicrystalline polymers.[29]

The effect of the pressure in the upstream chamber on the permeation properties of PAALA-6 films to O_2, N_2 and CO_2 at 25 ºC for pressures up to 7 atm is depicted in Figure 6. The isotherms representing the variation of P, D and S show the same pattern of behavior for the three gases. Whereas the permeability coefficient P appears to be unaffected by the pressure (Figure 6a) within the whole range of pressures, the diffusion coefficient D (Figure 6b) exhibits an anomalous decrease in the low-pressure region, the upturn being smaller for O_2 and even much smaller for N_2. This behavior is opposite to that generally observed in semicrystalline polymers.[27,30] The effect of the pressure on the apparent solubility coefficient is plotted in Figure 6c. As expected, the values of the solubility coefficient for the three gases shows a small increase or upturn in the low-pressure region with differences among them similar to those observed on the D-p isotherms. Such a behavior is thought to be due to the plasticization effects exerted by the gases on the transport process. The more condensable is the gas, the more soluble is it. In other words, the relatively high boiling point of CO_2 is responsible for the high solubility of this gas in PAALA-*n* in comparison with that of N_2 and O_2.

On the assumption that the films are homogeneous systems, the transport of gases through the films may be described as a thermally activated process where the temperature dependence of the permeability parameters obeys the Arrhenius law given by:

$$X = X_0 \exp-\left(\frac{E_x}{RT}\right) \qquad (8)$$

In this equation, X stands for either the permeability or the diffusion coefficient , whereas X_0 and E_X are their corresponding pre-exponential factors and activation energies, respectively. Activation energies associated with the diffusion process may be therefore determined from semilogarithmic plots of X against 1/T, as depicted in Figure 7. The values of E_P and E_D obtained by this means are compared in Table 3. It can be seen that the relative values of E_P and E_D follow the trends $Ep(CO_2) < Ep(N_2) < Ep(O_2)$ and $E_D(CO_2) < E_D(O_2) < E_D(N_2)$, and that E_P is smaller than E_D for all cases. Consequently, the heat of solution, ΔH, of PAALA-6 will be negative and decreases from N_2 to CO_2 in a similar manner as it happens in other polymers such as LLDPE films although a positive heat of solution is usually measured in these cases.

The permselectivity of films is usually expressed in terms of an ideal separation factor, α (A/B), equal to the ratio of the permeability coefficient of the two gases considered.

$$\alpha\left(\frac{A}{B}\right)=\left(\frac{P_A}{P_B}\right)=\left(\frac{D_A}{D_B}\right)\cdot\left(\frac{S_A}{S_B}\right) \qquad (9)$$

Accordingly, values of the selectivity coefficient of CO_2 respect to N_2 and O_2 resulting for PAALA-6 used in this study are shown in Table 4, which shows that the transport of CO_2 is favored respect to both N_2 and O_2. As expected, an increase in temperature tends to decrease the permselectivity of the films.

Computer Simulations. The Structure of PAALA-6 Revisited. The poorly ordered nature of PAALA-6 makes difficult the structural study of this polymer by X-ray diffraction.[5,6] The scarce number of reflections observed in the diffraction patterns are broad and diffuse adding a considerable degree of uncertainty to spacing

determinations. For this reason, the hexagonal form of PAALA-*n* common to all members with $n \leq 4$ was used as a model to interpret the structure of PAALA-6. The crystal unit cell of such form is monoclinic with two chains in antiparallel arrangement although for simplicity it is usually described in terms of a hexagonal pseudocell containing only one chain. Thus PAALA-6 was assumed to consist of a roughly hexagonal packing of right-handed 13/4 helices with an approximate interchain distance of 17 Å.[6] Since the size of hexyl side chains is unsuitable to pack efficiently in a three-dimensional crystal array, the helices should be staggered at random. An atomistic description of this structure was provided some years ago using simple energy minimization techniques with the lattice parameters inferred from X-ray diffraction data. As we will see below, large discrepancies between experimental and calculated solubility coefficienrts were obtained when such a structure was used for simulation. In order to get a more accurate description of the crystal structure of PAALA-6 which could explain better experimental permeation results, we ran two MC simulations at room temperature. The first one (MC/1) was performed under *NVT* conditions using the lattice parameters estimated from experimental data corresponding to a rectangular lattice of a = 17.0 Å, and b = 29.4 Å.[6] In the second simulation (MC/2), which was of *NPT* type, the dimensions of the box were initially set as indicated in the Methods section and allowed to vary. In both cases, the c-parameter of the lattice was kept 19.9 Å which is the length of the identity period of the 13/4 helix of PAALA-*n*.

Figure 8a shows the evolution of the energy as a function of the number of steps for both MC/1 and MC/2. It can be seen that the system was equilibrated rapidly in the two cases but the structure resulting from the MC/2 simulation became more stable than that of MC/1. Figure 8b shows the evolution of the lattice parameters a and b resulting in the MC/2 simulation. Both parameters, a and b, were found to shorten spontaneously with relative changes of about 15 and 10%, respectively. Thus, MC/2 simulations predict a quasi-hexagonal pseudocell for PAALA-6 with parameters smaller than those provided by energy minimization methods. The density calculated for this highly compacted structure is 1.12 g·mL^{-1}, in much better agreement with the measured value (1.07 g·mL^{-1}) than that calculated for the structure resulting from MC/1 simulation, which is 0.86 g·mL^{-1}.

Inspection to the side chain dihedral angles of the different helices contained in the simulation boxes of either MC/1 or MC/2 corroborates that the hexyl chains are not crystallized. Thus, equivalent residues belonging to independent chains show quite different conformational angle distributions. This is illustrated in Figure 9a, which displays the conformational distribution of the two central dihedral angles for the sixth residue of the four chains pointing to the same directions (white circles in the simulation box depicted in Figure 3). It should be mentioned that for a three-dimensional ordered arrangement, the conformation distributions should be identical or almost identical. Similar results were obtained when other residues were analyzed (data not shown). On the other hand, the helices become slightly tilted with respect to the *c*-axis of the structure, an effect that had been previously detected with higher intensity by energy minimization calculations.[6] Figure 9b shows a representative structure of PAALA-6 as projected along the *c*-axis with 13/ 4 helices hexagonally packed and the hexyl side chains in the liquid state. In conclusion, the MC simulations carried out in this study reveal that the structure of PAALA-6 should be more compacted than previously described and corroborate that the hexyl side chains are in the liquid-like state.

Predicted Solubilities. MC simulations of *NVT* type were performed in order to compute the solubilities of N_2, O_2 and CO_2 in PAALA-6 at room temperature. Calculations were performed at 20ºC using the parameters for the uncompacted (MC/3 simulation) and compacted (MC/4 simulation) lattices described in in the previous section. Both simulations were run for a total of $1 \cdot 10^6$ steps. The starting structures of MC/3 and MC/4 were the last snapshot provided by MC/1 and MC/2, respectively, and therefore no equilibration period was required. Indeed, MC/3 is only an enlargement of MC/1. It should be noted that in order to apply the Widom´s test-particle insertion method the volume of the simulation box is convenient to be kept constant.

As a first step, we examined the unoccupied space for all the microstructures generated by MC/3 and MC/4 simulations. The results are summarized for each penetrant in Table 5, which displays the amount of unoccupied space averaged over the 200 microstructures recorded from both simulations. As expected, the available space calculated by MC/4 is smaller than that obtained by

MC/3. It is further observed that the amount of unoccupied space in the latter case is similar for the three penetrants, whereas MC/4 simulations yield a significantly higher value for CO_2. The amount of unoccupied space for CO_2 predicted by MC/3 is about three times larger than that resulting from MC/4. Figure 10 illustrates the amount and distribution of the unoccupied space for CO_2 in representative structures of PAALA-6 generated by MC/3 and MC/4. On the other hand, the unoccupied space for O_2 and N_2 becomes reduced up to twenty times when MC/·4 is used instead of MC/3. This is a very striking result since the lattice volumes used in the two methods differ in only about 80%. Such dramatic change in the available space may be accounted by a "densification" process that takes place when the interchain distances are too large. In this situation the void volume is distributed in large cavities that can be readily filled by penetrants. When the chains close up to each other at the equilibrium distances, the space is evenly distributed in small cavities of irregular shape, many of then being too small as to be occupied by the penetrants. This restriction is more severe for the case of spherical particles (O_2 and N_2) with regards to ellipsoids (CO_2) since the geometry of these particles allows a more efficient accommodation in the elongated space provided by the cavities.

Table 6 shows the calculated excess chemical potentials for the three penetrants investigated. The predicted solubilities, which were calculated using equations 1 and 2, are compared with the experimental data in the same table. For both MC/3 and MC/4, the calculated solubility increased in the order $CO_2 > O_2 > N_2$, according to what is experimentally observed. However, a quantitative comparison of calculated and experimental data reveals a strong discrepancy between MC/3 and MC/4. The solubilities predicted by MC/3 are overestimated by almost two orders of magnitude with respect to those obtained from experimental P and D values by means of equation 7. Conversely, the solubilities predicted by MC/4 are comparable to those derived from experimentation, the calculated values being around three times higher than the experimental ones. It should be noted that the value of S depends on the accuracy of P and D, and that these coefficients are largely determined by the crystallinity of the sample. Unfortunately, the latter effect has not been considered in our computational simulations. At any case, comparison of results obtained with MC/3 and MC/4 clearly indicates that the lattice parameters

resulting from *NPT* simulations provide a more correct description of the structure of PAALA-6 than was previously attained.

Finally, we have investigated the effect of the temperature on the predicted solubilities by MC simulations. For this purpose, we run MC simulation of *NVT* type at 80 ºC (MC/5). The unoccupied space, excess chemical potential and calculated solubility for the three penetrants are included in Tables 5 and 6. Results indicate that the amount of unoccupied space for spherical penetrants increases with the temperature. Thus, the space available for the O_2 and N_2 penetrants is near to three times larger at 80 ºC than at 20 ºC. Accordingly, the solubilities predicted for these two penetrants at 80 ºC are between two and three times greater than those obtained at 25 ºC. This is poor agreement with experimental data, which show that the solubilities of O_2 and N_2 are almost independent of the temperature. An opposite behavior is simulated for CO_2. The available space for this penetrant was found to decrease more than three times when the temperature increased from 20 ºC to 80 ºC and in consequence, the solubility predicted at 80 ºC for CO_2 in PAALA-6 arrives to be about seven times smaller than that calculated at 20 ºC. This trend is in accordance with experimental results which show that the solubility of CO_2 in PAALA-6 decreases about three times when the temperature grows. Calculations at 80ºC using the uncompacted lattice (data not shown) showed the same trend for the three gases. At this moment we have not a plausible explanation for the lack of concordance found for the spherical penetrants N_2 and O_2. It is apparent however that the redistribution of the ineratomic space taking place upon heating is defectively simulated.

The method used in this work for the prediction of the solubility is a result from combining an advanced MC simulation for generation of microstructures in dense systems with the Widom´s test to insert particles in a polymeric matrix at random. The obtained results lead to conclude that these simulations are able to provide an accurate description of the structure of PAALA-6 as well as an adequate prediction of the solubility parameters at room temperature. Unfortunately these simulations produces unsatisfactory results at high temperatures, most probably due to the inefficiency of the method to evaluate the changes in shape of the cavities that take place upon heating. Further improvements of the methodology taking into

account temperature effects on the distribution of the void space are required, a research which is under course in our laboratory.

ACKNOWLEDGEMENTS

This research has been supported by Ministerio de Ciencia y Tecnología (grants nº BQU2000-0990 and MAT99-1127-C04-04), and by Fundació Caixa-Castelló through Grant P1B97-03. The authors are indebted to CESCA for computational facilities. David Zanuy acknowledges the grant received from the Ministerio de Educación to support the realization of his PhD.

REFERENCES

1) Muñoz-Guerra, S; López-Carrasquero, F., Fernández-Santín, J.M.; Muñoz-Guerra, S. In *Polymeric Materials Encyclopedia*, *6*, 4694, J.C. Salamone, Ed., CRC Press, Boca Raton, Fl, 1996.

2) López-Carrasquero, F; García-Alvarez, M.; Muñoz-Guerra, S.; *Polymer.* **1994**, *35*, 4502.

3) López-Carrasquero, F.; García-Alvarez, M., Navas, J.J.; Alemán, C.; Muñoz-Guerra, S. *Macromolecules* **1996**, *29*, 8449.

4) López-Carrasquero; Alemán, C.; García-Alvarez, M.; Martínez de Ilarduya, A.; Muñoz-Guerra, S.; *Macromol. Chem. Phys.* **1995**, *196*, 253.

5) López-Carrasquero, F.; Montserrat, S.; Martínez de Ilarduya, A.; Muñoz- Guerra, S. *Macromolecules* **1995**, *28*, 5535.

6) Navas, J.J.; Alemán, C.; López-Carrasquero, F.; Muñoz-Guerra, S. *Polymer* **1997**, 38, 3484.

7) Zanuy, D.; Alemán, C.; Muñoz-Guerra, S. Submitted work.

8) Puleo, A. C.; Paul, D. R.; Wong, P. K. *Polymer* **1989**, *30*, 1357.

9) Mohr, J. M.; Paul, D. R. *Polymer* **1991**, *32*, 1236.

10) Durrill, P. L.; Griskey, R. G. *AIChE J* **1996**, *15*, 106.

11) Mogri, Z.; Paul, D. R. *Polymer* **2001**, *42*, 2531.

12) Zanuy, D.; León, S.; Alemán, C.; Muñoz-Guerra, S. *Polymer* **2000**, *41*, 4169.

13) Zanuy, D.; Namba, A.; León, S.; Alemán, C.; Muñoz-Guerra, S. *Polymer* **2001**, *42*, 281.

14) Zanuy, D.; Alemán, C.; López-Carrasquero, F.; Báez, M. E.; García-Alvarez, M.; Laso, M.; Muñoz-Guerra, S. *Macromol. Chem. Phys.* **2001**, in press.

15) Loos, K.; Muñoz-Guerra, S. *Supramolecular Polymers*, p 209-231, Ed. A. Ciferri,

Marcel Dekker, 2000.

16) Rodríguez-Galán, A.; Muñoz-Guerra, S.; Subirana, J.A.; Chuong, B.; Sekiguchi, H. *Makromol. Chem., Macromol. Symp.* **1986**, *6*, 277.

17) García-Alvarez; M.; López-Carrasquero, F.; Tort, E.; Rodríguez-Galán, A.; Muñoz-Guerra, S. *Synth. Commun.* **1994**, *24*, 745.

18) Tanaka, S. Ph. D. Thesis 1972. University of Kyoto.

19) De Pablo, J. J.; Laso, M.; Suter, U. W. *J. Chem. Phys.* **1992**, *96*, 6157.

20) Siepmann, J. I.; Frenkel, D. *Mol. Phys.* **1992**, *75*, 59.

21) León, S.; Alemán, C.; Escalé, F.; Laso, M. *J. Comput. Chem.* **2001**, *22*, 162.

22) Martínez de Ilarduya, A.; García-Alvarez, M.; Alemán, C.; López-Carrasquero, F.; Muñoz-Guerra, S. *Macromolecules* **1999**, *32*, 3257.

23) Weiner, S. J.; Kollman, P. A.; Case, D. A.; Singh, U. C.; Ghio, C.; Alagona, G.; Profeta, S.; Weiner, P. *J. Am. Chem. Soc.* **1984**, *106*, 765.

24) Müller-Plathe, F. *Macromolecules* **1991**, *24*, 6475.

25) Widom, B. *J. Phys. Chem.* **1982**, *86*, 869.

26) Barrer, R. M. *Trans Faraday Soc.* **1939**, 35, 628.

27) Compañ, V.; López, Mª.L.; Andrio, A.; Riande, E. *Macromolecules* **1998**, 31, 6884.

28) Glatz, F.P.; Mülhanpt, R. *J. Membr. Sci.* **1991**, 90, 151.

29) Haraya, K.; Hwang, S.T. *J. Membr. Sci.* **1992**, 71, 13.

30) Michaels, A.S.; Bixler, H. *J. Polym. Sci.* **1961**, 50, 393.

Table 1. Synthesis Data of PAALA-6

[PABLA]/[*n*-$C_6H_{11}OH$]	1/115
[PABLA]/[$Ti(OBu)_4$]	1/0.4
Yield (%)	85
Conv (%)[a]	100
[η] ($dL \cdot g^{-1}$)[b]	2.62
M_v[c]	$2.2 \cdot 10^5$
ρ ($g\ mL^{-1}$)[d]	1.06

[a]Degree of replacement of benzyl by *n*-hexyl group as determined by ^1H NMR.

[b]Intrinsic viscosity measured in dichloroacetic acid at 25 ± 0.1 ºC

[c]Viscosity average molecular weight estimated by using the Mark-Howink equation reported for poly(γ-methyl-α-L-glutamate).[18]

[d]Density of the polymer measured by flotation in KBr aqueous solution-water water mixtures.

Table 2. Lennard-Jones Potential Parameters for the Penetrants

penetrant	R (Å)	ε (kcal/mol)
N_2[a]	1.850	0.1890
O_2[a]	1.790	0.2333
CO_2[b]		
C	1.850	0.1200
O	1.600	0.2000

[a]An spherical model was used to describe these penetrants.

[b]Represented by a model including the all thre atoms with a C=O bond length of 1.162 Å. Accordingly, the penetrant is viewed as an ellipsoid of dimensions $d_1 = 2(1.600+1.162) + 1.850 = 7.374$ Å and $d_2 = 3.70$ Å.

Table 3. Activation Energy (kcal/mol) for CO_2, O_2 and N_2 Obtained from Permeabilitties and Diffusion Coefficient Measurements through PAALA-6 Films

gas	E_P(kcal mol^{-1})	E_D(kcal mol^{-1})	ΔH_S(kcal mol^{-1})[a]
CO_2	3.9	8.0	-4.1
O_2	6.6	7.4	-0.8
N_2	6.0	6.7	-0.7

[a]Heat of solution $\Delta H = (E_P - E_D)$.

Table 4. Permselectivity of PAALA-6 Films

T °C	$\frac{P(CO_2)}{P(O_2)}$	$\frac{P(CO_2)}{P(N_2)}$
20	10.3	24.4
30	6.8	22.7
40	5.8	21.1
50	5.4	20.2
60	4.8	16.8
70	4.6	15.1
80	4.0	12.0

Table 5. Predicted Unoccupied Space[a] (%) for Penetrants in the Quasi-hexagonal Structure of PAALA-6

lattice[b]	simulation	T (ºC)	O_2	N_2	CO_2
a = 17.0 Å, b = 29.4 Å, c = 19.9 Å	(MC/3)	20	2.39	2.07	2.36
a = 14.6 Å, b = 26.4 Å, c = 19.9 Å	(MC/4)	20	0.13	0.10	0.70
	(MC/5)	80	0.34	0.26	0.19

[a]Unoccupied space has been computed considering different temperatures and different simulation boxes and averaged over the 200 microstructures generated by MC simulations of *NVT* type.

[b]Models built using the lattice parameters obtained from energy minimization[6] and MC simulation methods.

Table 6. Calculated Excess Chemical Potentials (μ_{ex}, in kcal mol^{-1}), Predicted Solubilities (S_{calc}, in barrers) and Experimental solubilities (S_{exp}, in barrers) for Penetrants in the Quasi-Hexagonal Structure of PAALA-6

lattice	simulation	T (ºC)	#	O_2	N_2	CO_2
a = 17.0 Å, b = 29.4 Å, c = 19.9 Å	(MC/3)	25	μ_{ex}	-1.34	-1.25	-2.01
			S_{calc}	$11 \cdot 10^{-2}$	$9.8 \cdot 10^{-2}$	$35 \cdot 10^{-2}$
			S_{exp}	$0.27 \cdot 10^{-2}$	$0.14 \cdot 10^{-2}$	$2.4 \cdot 10^{-2}$
a =14.6 Å, b =26.4 Å, c = 19.9 Å	(MC/4)	25	μ_{ex}	0.40	0.57	-1.15
			S_{calc}	$0.60 \cdot 10^{-2}$	$0.50 \cdot 10^{-2}$	$8.3 \cdot 10^{-2}$
			S_{exp}	$0.27 \cdot 10^{-2}$	$0.14 \cdot 10^{-2}$	$2.4 \cdot 10^{-2}$
a =14.6 Å, b =26.4 Å, c = 19.9 Å	(MC/5)	80	μ_{ex}	-0.16	-0.02	-0.20
			S_{calc}	$1.5 \cdot 10^{-2}$	$1.2 \cdot 10^{-2}$	$1.2 \cdot 10^{-2}$
			S_{exp}	$0.23 \cdot 10^{-2}$	$0.11 \cdot 10^{-2}$	$0.72 \cdot 10^{-2}$

CAPTIONS TO FIGURES

Figure 1.- Schematic projections down the chain axis of PAALA-n: a) The hexagonal crystal structure of PAALA-4; b) The biphasic layered structure of PAALA-18.

Figure 2. Experimental device used in the gas transport measurements.

Figure 3. Schematic representation of the simulation box used for MC calculations of PAALA-6. The circles refer to the position of the eight chains explicitly included. Filled and empty circles correspond to chains pointing up and down, respectively.

Figure 4. Variation of the pressure of carbon dioxide in the downstream chamber with time in PAALA-6 films. p_0 = 0.5 atm (o), 1 atm (x), 2 atm (•) and 7 atm (■).

Figure 5. Temperature dependence of the apparent permeability (a), diffusion (b) and solubility (c) coefficients of CO_2 (◆), O_2 (■) and N_2 (●) through PAALA-6 films at p_0 = 1 atm. P is expressed in barrers. 1 barrer = 10^{-10} cm^3 (STP) of gas·cm·cm^{-2}·s^{-1}·cm^{-1} Hg^{-1}.

Figure 6. Variation of the apparent permeability (a), diffusion (b) and solubility (c) coefficients of CO_2 (◆), O_2 (■) and N_2 (●) with the pressure of the upstream chamber, at 25 ºC in PAALA-6 films.

Figure 7. Arrhenius plots for the apparent diffusion (a) and permeability (b) coefficients of CO_2 (◆), O_2 (■) and N_2 (●). The values were obtained at 25 ºC under an upstream pressure of 1 atm.

Figure 8. (a) Energy of PAALA-6 provided by MC/1 and MC/2 simulations as a function of the number of steps. (b) Cell parameters of PAALA-6 provided by MC/2 simulation as a function of the number of steps.

Figure 9. Conformational distribution obtained from MC/2 for two consecutive side chain dihedral angles of the sixth residue of the four independent chains arranged in the same direction (see Figure 3). (b) Projection along the *c*-axis of a representative snapshot obtained from MC/2 simulation. Note that the helices are slighted twisted with respect to the *c*-axis.

Figure 10. Unoccupied space for CO_2 in one of the microstructures of PAALA-6 generated by MC/3 (a) and MC/4 (b).

(a)

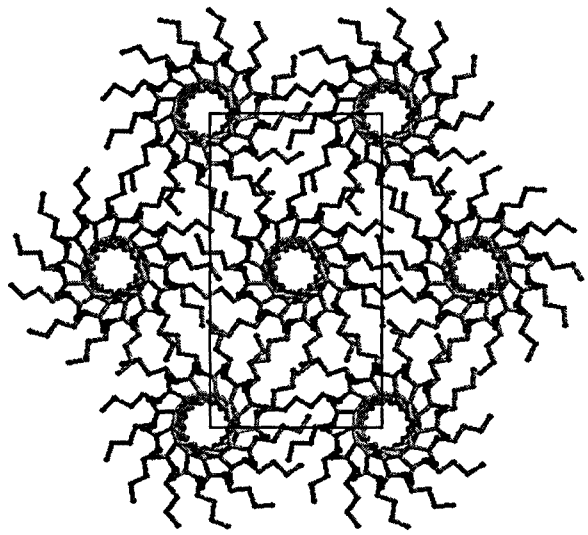

(b)

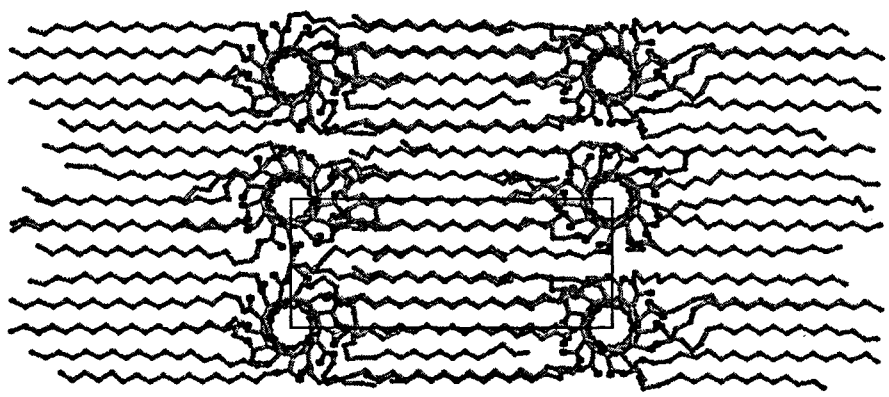

Figure 1. Compañ et al., 2001

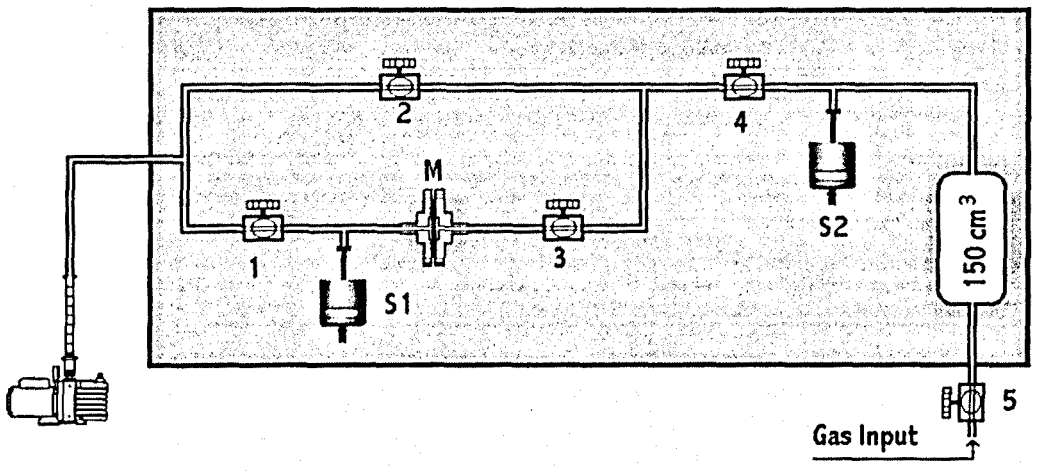

Figure 2. Compañ et al., 2001

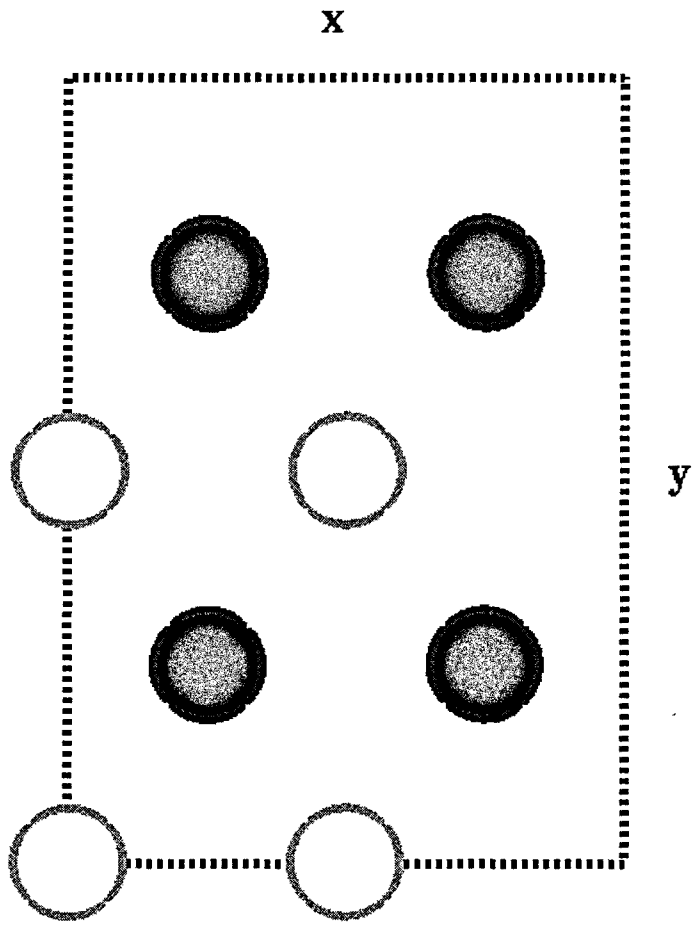

Figure 3. Compañ et al., 2001

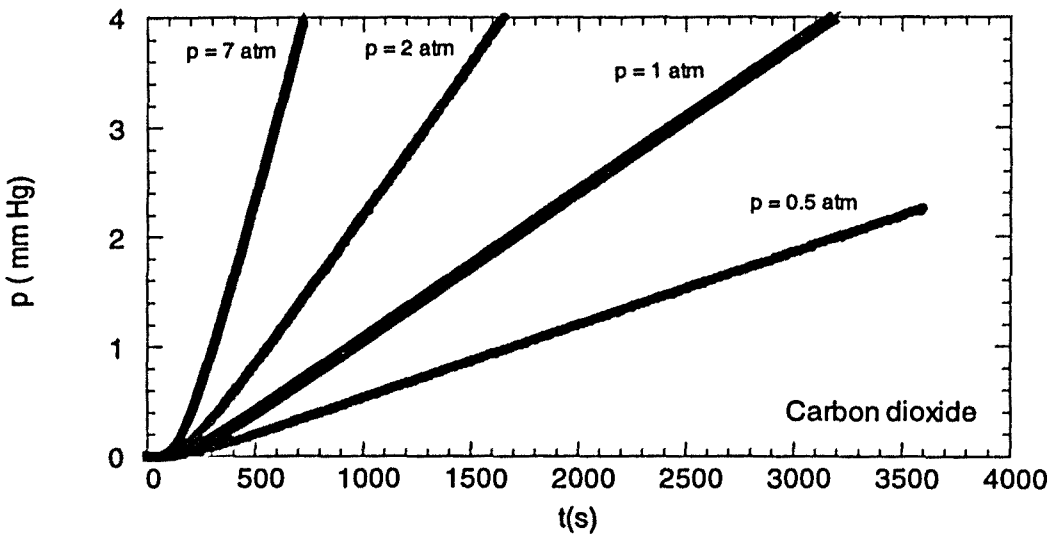

Figure 4. Compañ et al. 2001

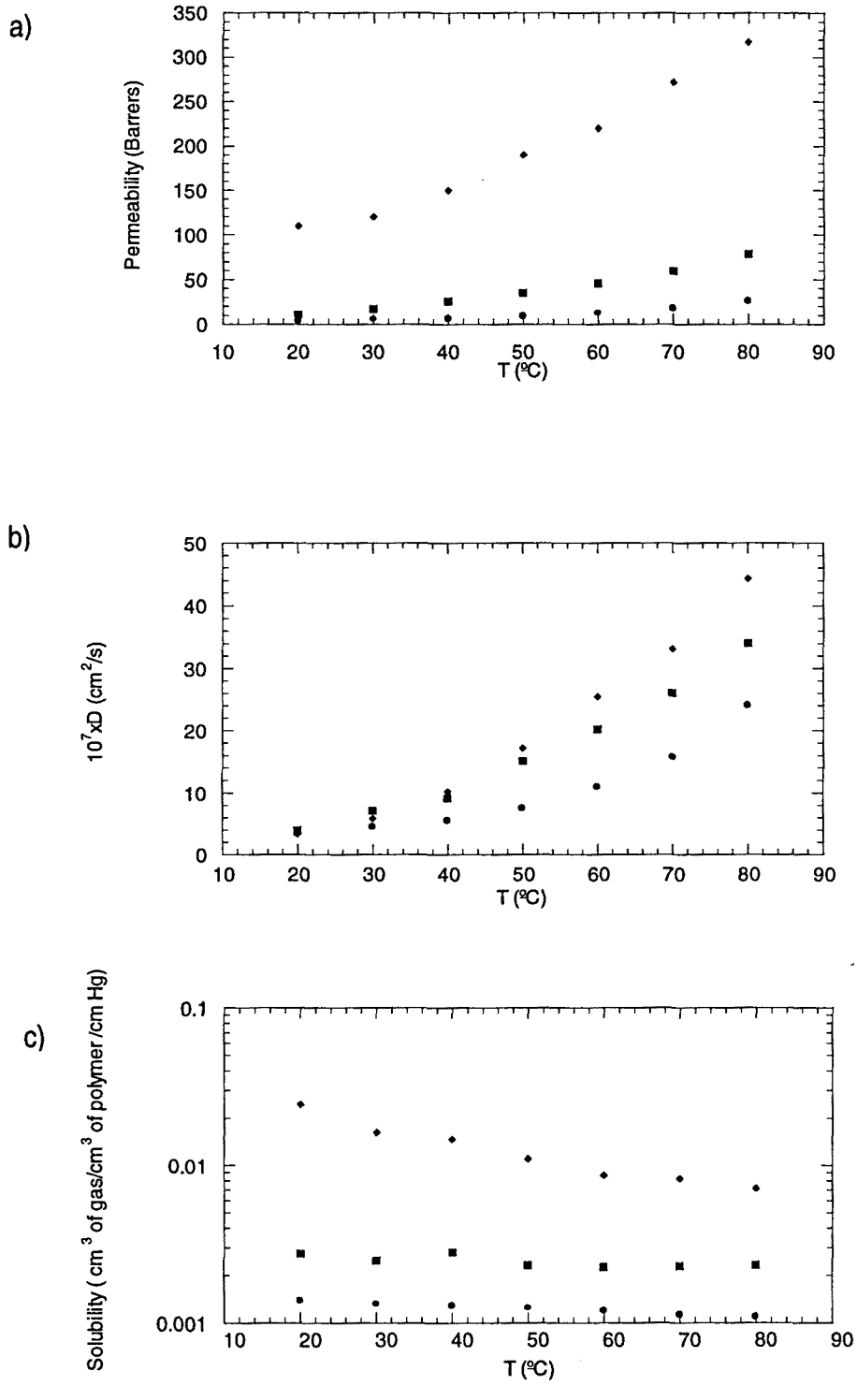

Figure.5. Compañ et al. 2001

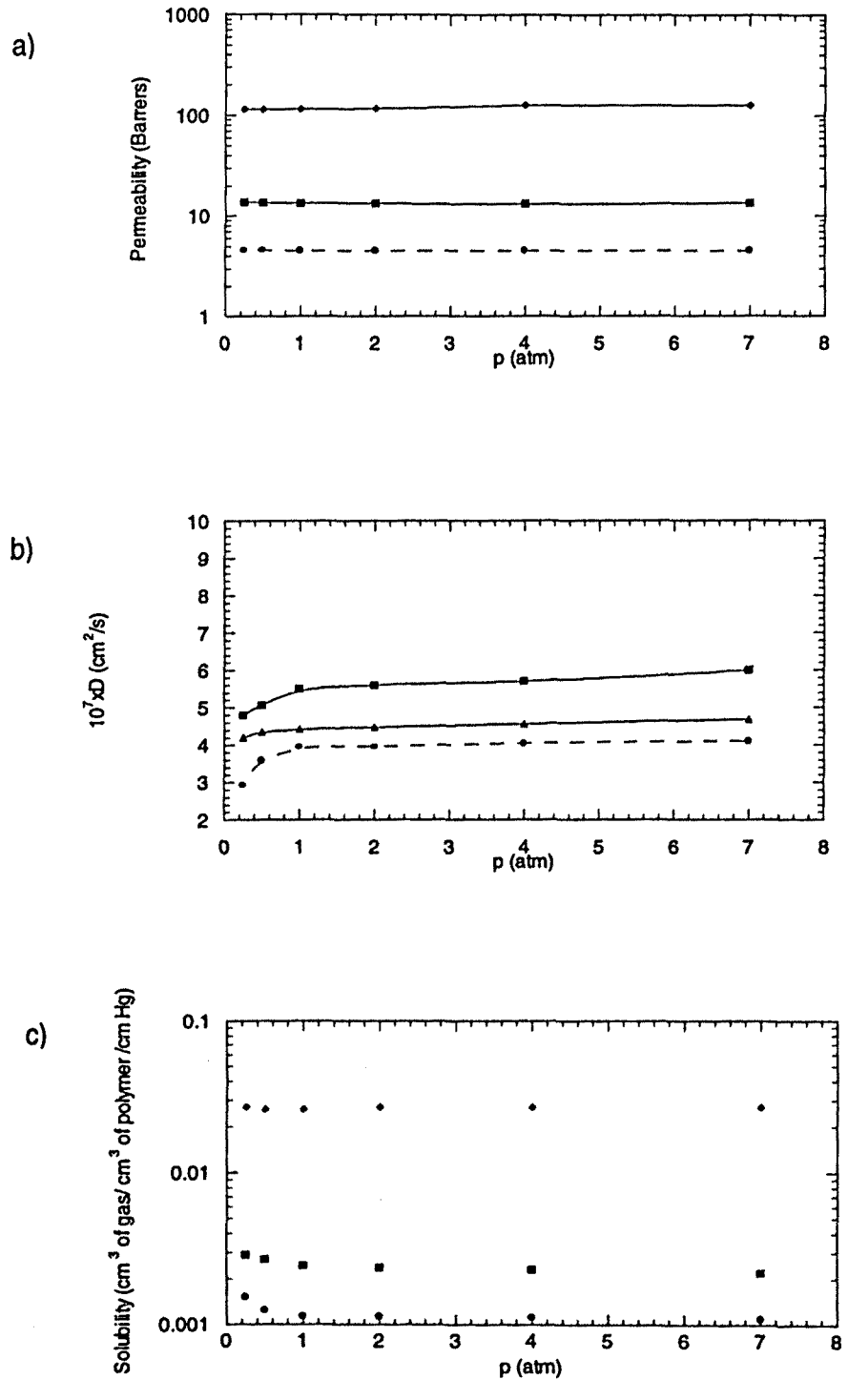

Figure.6. Compañ et al. 2001

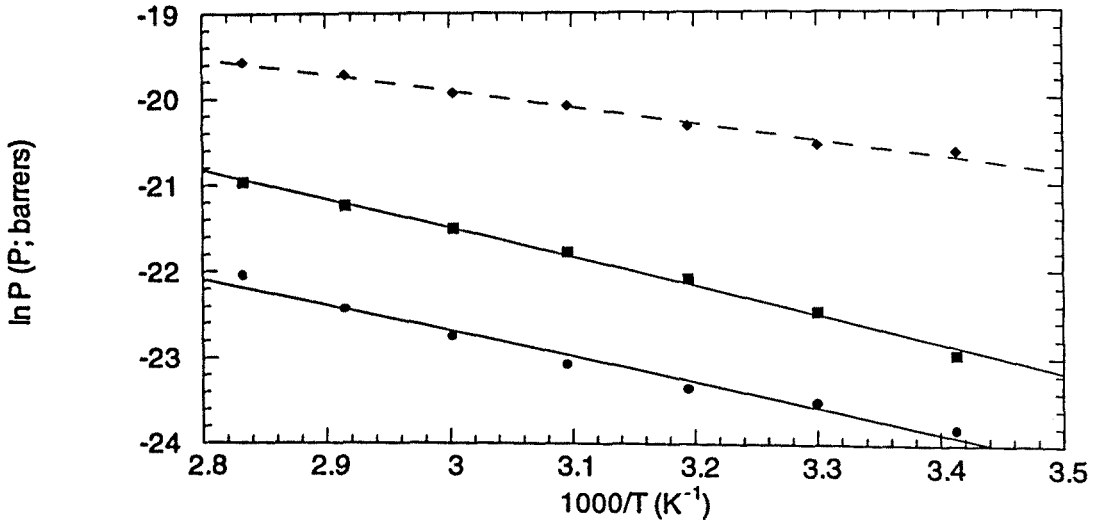

Figure 7. Compañ et al. 2001

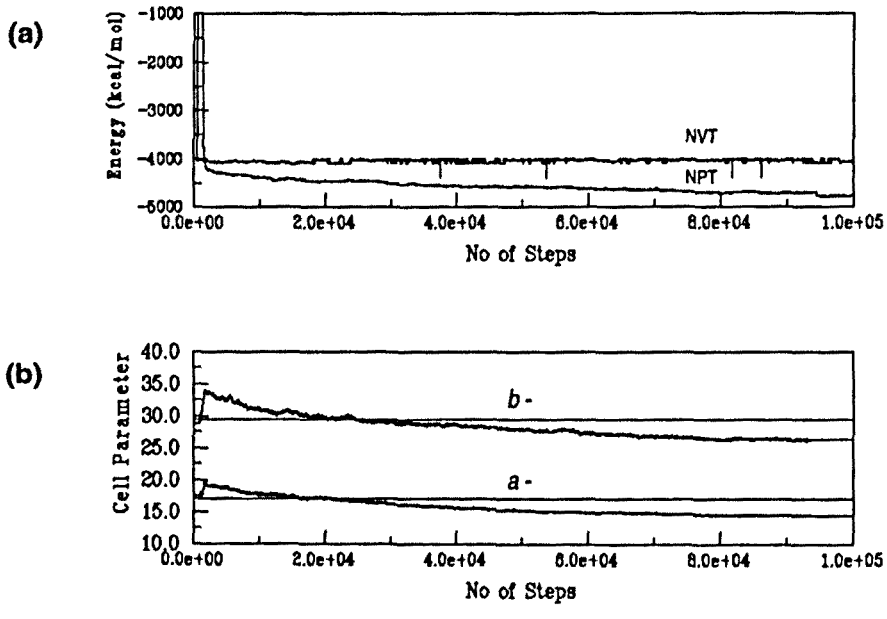

Figure 8. Compañ et al., 2001

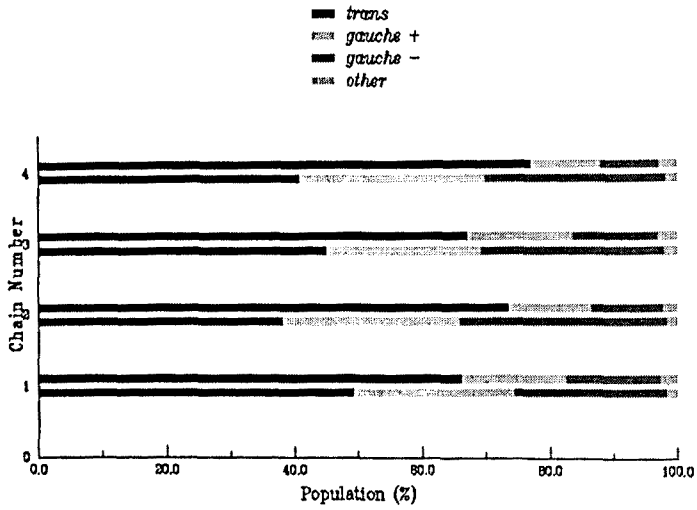

Figure 9a. Compañ et al., 2001

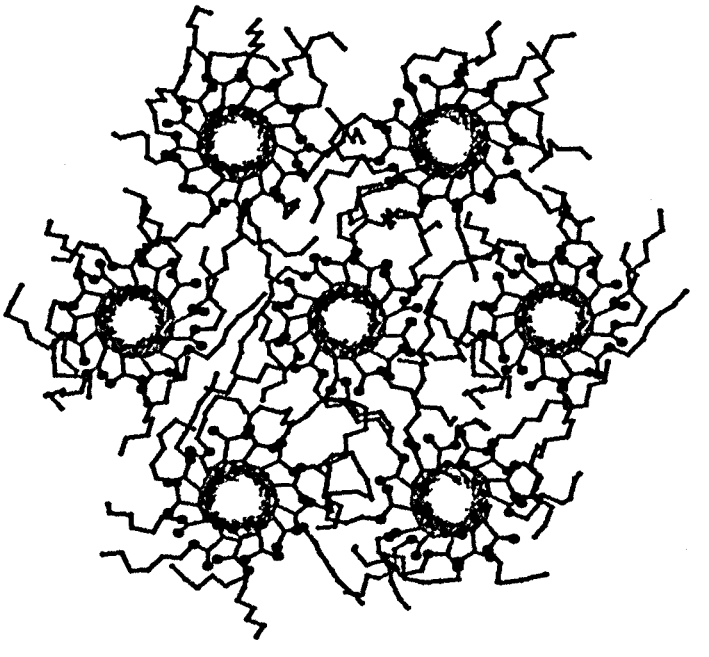

Figure 9b. Compañ et al., 2001

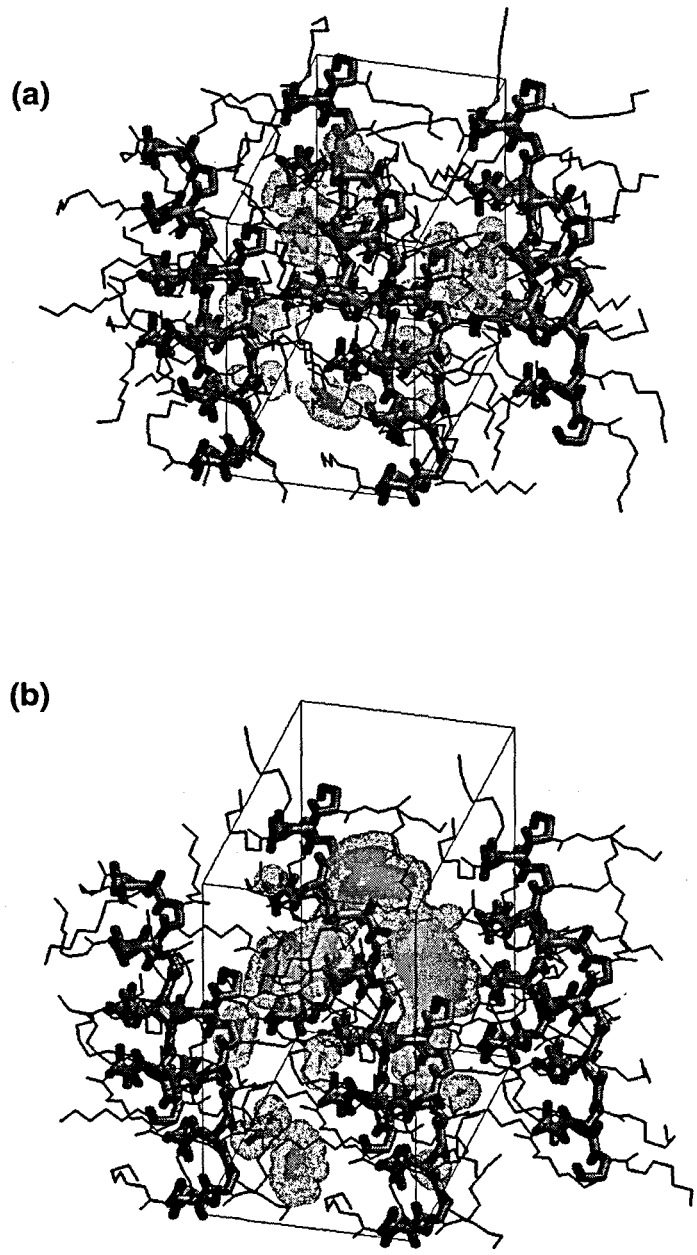

Figure 10. Compañ et al., 2001

VIII.9. Conclusiones parciales

1) Se ha desarrollado una metodología teórica capaz de evaluar la solubilidad de diferentes gases simples en matrices poliméricas ordenadas. La estrategia se basa en calcular el espacio no ocupado por las cadenas de polímero y accesible al penetrante. Este proceso se realiza empleando microestructuras de la matriz polimérica obtenidas a partir de la exploración del espacio conformacional mediante el método MC - CB. El espacio accesible al penetrante permite obtener el potencial químico a dilución infinita el cual, a su vez, está relacionado con la solubilidad del gas en la matriz polimérica.

2) La bondad de la metolodogía desarrollada ha quedado claramente puesta de manifiesto al comparar las solubilidades calculadas para el CO_2 y el CH_4 en el PMP cristalino con las obtenidas experimentalmente. Así, los resultados teóricos no sólo están en concordancia con los datos experimentales desde un punto de vista cualitativo, sino también cuantitativo.

3) Se ha estudiado la solubilidad de diferentes gases en las formas cristalinas hexagonal y tetragonal de los PAALA-*n* con $n = 1$ y 4. Los resultados han indicado que estos polímeros presentan solubilidades extremadamente bajas para los gases con un volumen de partícula superior al del He. Esto es debido a que las cadenas se empaquetan tridimensionalmente de forma muy eficaz y, en consecuencia, el volumen accesible al penetrante en la matriz polimérica es extremadamente pequeño. De hecho, estos polímeros, y en particular el PAALA-1, pueden considerarse como materiales barrera.

4) Se ha investigado la solubilidad de diferentes gases en la fase B de los PAALA-*n* con $n = 12$, 14 y 16. El espacio accesible al penetrante es mucho mayor en estos polímeros que en el PAALA-1 y el PAALA-4. Además, cuando se consideran penetrantes de pequeño volumen molecular, la interacción entre la matriz polimérica y el penetrante es considerablemente atractiva. En consecuencia, la solubilidad de gases en los polímeros con estructura bifásica es mucho mayor que en los polímeros ordenados tridimensionalmente.

5) Se ha estudiado la solubilidad de N_2, O_2 y CO_2 en el PAALA-6. Los valores calculados a temperatura ambiente están en excelente concordancia con los obtenidos experimentalmente. Para este polímero el espacio accesible al penetrante presenta un valor intermedio entre los obtenidos en los polímeros con cadenas laterales cortas y los PAALA-*n* con $n \geq 12$. Este hecho es debido al tipo de estructuración que presentan las cadenas de PAALA-6: un empaquetamiento hexagonal de hélices con las cadenas laterales totalmente desordenadas. Esta organización molecular es intermedia con respecto a la de los polímeros anteriormente citados.

IX. CONCLUSIONES

IX. CONCLUSIONES GENERALES.

1) Se ha propuesto un modelo para la conformación helicoidal del PGGA en estado no ionizado. La hélice obtenida es sinistrorsa y presenta puentes de hidrógeno intramoleculares entre los grupos amida *i* e *i+3*. La estabilidad del modelo propuesto se ha investigado en base al efecto del disolvente, la temperatura y el tamaño molecular. Se ha observado que el disolvente favorece considerablemente la conformación helicoidal, mientras que un aumento de la temperatura y/o la reducción del tamaño molecular inducen la evolución hacia un ovillo estadístico. La comparación entre el PGGA y el PAGA ha puesto de manifiesto que los homopolímeros enantioméricamente puros derivados del ácido glutámico son excelentes formadores de hélices, independientemente de su constitución química. Así, las conformaciones helicoidales obtenidas para ambos polímeros son morfológica y topológicamente análogas.

2) Se han investigado las diferentes formas cristalinas descritas para algunos de los poli(γ-glutamato)s derivados del PGGA de biosíntesis. El modelo propuesto para la forma I del PAB(D)G y PAB(D,L)G corresponde a una estructura ortorrómbica, con dos hélices 2/1 antiparalelas por celda, y situadas en las posiciones cristalográficas (0,0,0) y (1/2, 0,0). La forma II del PAB(D)G, PAAG-1, PAAG-2 y PAAG-3^{i} está constituida por un empaquetamiento pseudo - hexagonal de hélices 5/2 dextrorsas, con dos cadenas en las posiciones cristalográficas (0,0,0) y (1/2,1/2,0) de una celda ortorrómbica. Finalmente, la forma III del PAAG-2 corresponde a una estructura en láminas, con dos hélices 2/1 antiparalelas dispuestas en las posiciones cristalográficas (0,0,0) y (0,1/2,0) de una celda ortorrómbica. Las hélices 2/1 de las formas I y III están estabilizadas por puentes de hidrógeno intermoleculares, mientras que la hélice 5/2 de la forma II presenta puentes de hidrógeno intramoleculares entre los grupos amida *i* e *i+2*.

3) Se ha estudiado la naturaleza de la interacción electrostática característica de los complejos polipéptido - tensioactivo mediante compuestos modelo. Estudios mecanocuánticos han puesto de manifiesto que la interacción entre el anión acetato y el catión alquiltrimetilamonio viene modulada por la longitud del grupo alquilo. Los complejos constituidos por más de dos iones moleculares se caracterizan por presentar una geometría asimétrica y un efecto anticooperativo en la energía libre de interacción.

4) Los complejos PAGA·*n*ATMA y PGGA·*n*ATMA muestran grandes diferencias estructurales en disolución de cloroformo. En el primero, el polipéptido presenta una conformación en hélice α extremadamente estable, ya que el tensioactivo no puede interaccionar con los grupos amida esqueletales. Por el contrario, en el PGGA·*n*ATMA la cadena polipeptídica no es capaz de adoptar una conformación regular debido a las interacciones que se establecen entre los grupos amida y los tensioactivos. Por otro lado, se han caracterizado las interacciones electrostáticas presentes en este tipo de complejos mediante cálculos mecanocuánticos, poniéndose de manifiesto su naturaleza anticooperativa y su geometría asimétrica.

5) Se ha estudiado la estructura del PAALA-18 en las fases A y C. En la fase A las cadenas laterales se empaquetan en disposición hexagonal dando lugar a un cristal parafínico. Esta ordenación conduce a una distribución de densidades muy homogénea en la fase parafínica, que contrasta con la variabilidad mostrada en el perfil de densidades de la fase B. Por otro lado, se han caracterizado los principales cambios estructurales implicados en la transición entre las fases B y C. En este proceso, las cadenas alquílicas pierden la distribución conformacional característica de las fases A y B. Además, se ha observado como las cadenas de polímero tienden a perder su estructuración laminar. Así, la distancia entre cadenas adyacentes de una misma lámina aumenta mientras que la distancia entre cadenas de láminas diferentes tiende a reducirse.

6) Se ha desarrollado una metodología teórica capaz de estimar la solubilidad de gases simples en polímeros con estructuras ordenadas. Esta estrategia permite calcular el potencial químico en exceso, el cual se puede relacionar de forma sencilla con el coeficiente de solubilidad. Mediante esta metodología se ha investigado la solubilidad de algunos gases simples en diferentes estructuras ordenadas características de los PAALA-*n*. Los resultados obtenidos indican que los polímeros con estructuras ordenadas tridimensionalmente se comportan como materiales barrera, mientras que la solubilidad de los diferentes penetrantes se hace notable en los polímeros con estructuras bifásicas.

X. REFERENCIAS BIBLIOGRAFICAS

X. REFERENCIAS BIBLIOGRAFICAS

Alemán C., Subirana J.A., Pérez J.J. *Biopolymers* **1992**, *32*, 621

Alemán, C. *Biopolymers* **1994**, *34*, 841

Alemán, C. *Int, J. Peptide Prot. Res.* **1995**, *46*, 408

Alemán C. *Chem. Phys.* **1999**, *244*, 151

Alexander L.E. "*X-Ray diffraction methods in Polymer Science*" **1969**, Jon Wiley & Sons, Inc. New York.

Allen F.H., Tildesley D.J. "*Computer simulations of liquids*" **1989**, Claredon Oxford.

Allinger N.L., Tribble M.T., Miller M.A., Wertz D.H. *J. Am. Chem. Soc.* **1971**, *93*, 1637

Allinger N.L., Sprague J.T. *J. Am. Chem. Soc.* **1976**, *95*, 3893

Allinger N.L., Kok R.A., Iman M.R. *J. Comput. Chem.* **1988**, *9*, 591

Antonietti M., Conrad J., Thünemann A. *Macromolecules* **1994**, *27*, 6007

Bachs M., Luque F.J., Orozco M. *J. Comput. Chem.* **1994**, *15*, 446

Balasubramanian D., Kalita C.C., Kovacs J. *Biopolymers* **1973**, *12*, 1089

Bates D.R. (ed.) "*Quantum Theory*" **1961**, Academic Press., New York

Becke A.D. *Phys.Rev.A* **1988**, *38*,3098

Becke A.D. *J.Chem.Phys.* **1993**, *98*, 1372

Bella J., Alemán C., Fernández-Santín J.M., Alegre C., Subirana J.A. *Macromolecules* **1992**, *22*, 1540

Bermúdez M., León S., Alemán C., Muñoz-Guerra S. *Polymer* **2000**, *41*, 8961

Binder K. "*Monte Carlo methods in statistical physics*" **1986** Springer, Berlin Heidelberg New York.

Birrer G.A., Cromwick A-M., Gross R.A. *Int. J. Biol Macromol.* **1994**, *16*, 265

Bocchi V., Casnati G., Dossena A., Marchelli R. *Synthesis* **1979**, 961.

Borbély M., Nagasaki Y., Borbély J., Fan K., Bhogle A., Sevoian M. *Polym. Bull.* **1994**, *32*, 127

Brise, F. *J. Electron Microsc. Techn.* 1989, *11*, 272

Bruckner V., Katjár M., Kovács J., Nagy H., Wein J. *Tetrahedron* **1958**, 2, 211

Casanovas J., Alemán C. *J. Comput. Aided Mol. Des.* **1994**, *8*, 441

Cerius^2 1.6 (**1994**) Molecular Simulations Inc., Burlington, MA.

Colmenero J., Mukhopadhayay R., Alegría A., Frick B. *Phys. Rev. Lett.* **1998**, *80*, 2350

Colmenero J. *Revista de Plásticos Modernos* **2000**, *80*, 427

Choi H.J., Kunioka M. *Radiat. Phys. Chem.* **1995**, *46*, 175

Choy C.L., Leung W.P., J. *Polym. Sci. Polym. Phys. Ed.* **1985**, *23*, 1759

Cohen M.H., Turnbull D.J. *J. Chem Phys.* **1959**, *31*, 1164

Cornell W.D., Cieplak P., Bayly C.I., Gould I.R., Merz K.M., Ferguson M.D., Spellmeyer D.C., Fox T., Caldwell J.W., Kollman P. *J.Am.Chem.Soc.* **1995**,*117*, 5179

Cromwick A-M., Gros R.A. *Int. J. Biol Macromol.* **1995**, *17*, 259

Crescenzi V., DÁlagni M., Dentini M., Mattei B. *ACS Symp Ser.* **1996**, *627*, 233

Cuthbert T.R., Wagner N.J., Paulaitis M.E. *Macromolecules* **1997**, *30* 3058

Daly W.H., Poché F. Negulescu I.I. *Prog. Polym. Sci.* **1994**, *19*, 79.

Dewar M.J.S., Zoebisch E.G., Healy E.F., Stewart J.J.P. *J. Am. Chem. Soc.* **1985**, *107*, 3902

De Pablo J.J., Laso M., Suter V.W. *J. Chem. Phys.* **1992**, *96*, 6157.

De Pablo J.J., Laso M., Siepmann J.I., Suter U.W *Mol. Phys.* **1993**, *80*, 55 **(a)** De Pablo J.J., Laso M., Suter U.W *Macromolecules* **1993**, *26*, 6180 **(b)**

Edelhoch H., Bateman J.B. *J. Am. Chem. Soc.* **1957**, *79*, 6093

Edinger M.D., Adolf D.B. *Adv. Polym. Scien.* **1994**, *116*, 74

Elvira C., Gallardo A., San Román J., López A. *Revista de Plásticos Modernos* **1999**, *77*, 153

Ferguson D.M., Kollman P.A. *J. Comput. Chem.* **1991**, *12*,620

Ferro D.R., Brückner S., Meille S.V., Ragazzi. M. *Macromolecules* **1992**, *25*, 5231

Ferro D.R., Ragazzi M. "*Conformational (Hyper)Analysis Milan Package*" **1993** Instituto di Chimica delle Macromolecole del CNR, Milano, Italy.

Ferro D.R., Provasoli A. *Macromol. Theory Simul.* **1996**, *5*, 231

Ferro D.R., Porzio W., Destri S., Ragazzi M. *Macromol. Theory Simul.* **1997**, *6*, 713

Ferro D.R., Mielle S.V., Brückner S. Macromolecules, **1998**, *31*, 6926

Field M.J., Basch P.A., Karplus M. *J. Comput Chem.* **1990**, *11*, 700

Flectcher R., Powell M.D.N., *Comp. J.* **1963**, *6*, 163

Flory, P.J. "*Statistical Mechanics of Chain Molecules*" **1969** Interscience Publ. New York.

Frank F.C., Keller A., O´Connor A. *Phikos. Mag,* **1959**, *4*, 200

Frenkel D., Mooij G., Smit B. *J. Phys.: Condens. Matter.* **1991**, *3*, 3053

Frenkel D., Smit B. *Mol. Phys.* **1992**, *75*, 983

Frenkel D., Mooij G., "*Daresbury Laboratory Information Quarterly for Computer Simulation of Condesed Phases*" **1994**, No. 41

Frisch M.J., Pople J.A., Binkley J.S. J.Chem.Phys. **1984**, *18*, 3265

Fukuda M. *J. Chem. Phys.* **2000**, *112*, 478

Gao J. *J. Am. Chem. Soc.* **1994**, *116*, 1563

García-Alvarez M., León S., Alemán C., Campos J.L., Muñoz-Guerra S. *Macromolecules* **1998**, *31*, 124

Glenis s., Benz M., LeGoff E., Schindler J.L., Kannewuf C.R., Kanatzidis M.G. *J. Am. Chem. Soc.* **1993**, *115*, 12519

Giannos A.S., Shah D., Gross R.A., Kaplan D.L., Arcindiacono S., Mayer J.M. *Proc. Polym. Mater. Sci. Eng.* **1990**, *62*, 236

González D., Fan K., Sevoian M. *J. Polym. Sci. Polym. Chem.* **1996**, *34*, 2019

Goto A., Kinouka M., *Biosci. Biotech. Biochem.* **1992**, *56*, 1031
Griffith J.H., Ranby B.G. *J. Polym Sci.* **1960**, *44*, 369

Gross R.A. *Proc. MacroAkron'94* **1994**, 464

Gross R.A., McCarthy S.P., Shah DT. **1995**, US Patent 5, 378, 807

Gusev A.A., Müller-Plate F., van Gunsteren W.F., Suter U.W. *Adv. in Polymer Scie* **1994**, *116*, 207

Hariharan P., Pople J.A. *Theor. Chim. Acta* **1973**, *28*, 213.

He L.M., Neu, M.P., Vanderberg L.A. *Env. Science and Tech.* **2000**, *34*, 1694

Holtzer A., Hawkins R.B. *J. Am. Chem. Soc.* **1996**, *118*,4220

Hohenberg P., Kohn W. *Phys. Rev. A* **1964**, *136*, 864

Ibraginova Z., Kasaikin V.A., Zezin A.B., Kabanov V.A. *Polym. Sci. USSR* **1986**, *28* 1826

Jorgensen W.L., Briggs J.M., Contreras M.L. *J. Phys. Chem.* **1990**, *94*, 1683

Keith H.D., Giannoni G., Padden F.J. *Biopolymers*, **1969**, *7*, 775

Kohn W., Sham L.J. *Phys.Rev. A* **1965**, *140*, 1133

Kollman P.A. *J. Am .Chem. Soc.* **1972**, *94*, 1838

van Krevelen "*Properties of Polymers*" **1990**, Elsevier, Amsterdam.

Kusanagi H., Takase M., Chatani Y., Tadokoro H. *J. Polym. Sci., Plum. Phys. Edn.* **1978**, *16*, 131

Kubota H., Fukuda H., Takebe H., Endo, T. **1992**, US Patent 5, 118, 784
Kubota H., Matsunobu T., Uotani K., Takebe H., Satoh A., Tanaka T., Taniguchi M. *Biosci. Biotech. Biochem.* **1993**, *57*, 1212

Lacks D.J., Rutledge G.C. *J. Phys. Chem.* **1994**, *98*, 1222

Laso M., de Pablo J.J, Suter U.W. *J. Chem. Phys.* **1992**, *97*, 2817

Lavery R, Zakrzewska K., Pullman B. *J. Biomol. Struct. & Dyn.* **1984**, *3*, 1155

Lee C., Yang W., Parr R.G. *Phys.Rev. B* **1988**, *37*, 785

León S., Navas J.J., Alemán C., Muñoz-Guerra S. *Polymer* **1999**, *40*, 7351

León S., Alemán C., Bermúdez M., Muñoz-Guerra S. *Macromolecules* **2000**, *33*, 8756 **(a)** León S., Alemán C., Muñoz-Guerra S. *Macromolecules* **2000**, *33*, 5754 **(b)** León S., Alemán C., Muñoz-Guerra S., Laso M. *J. Theor. Comput. Polym. Sci.* **2000**, *10*, 177 **(c)** Léon , "Comunicación oral", **2000 (d)**

León S., Alemán C., Muñoz-Guerra S., Escale F., Laso M. J. *J. Comput. Chem.* **2001**, 22, 162

Leontidis E., de Pablo J.J., Laso M., Suter U.W. *Adv. Polym. Sci.* **1994**, *116*, 283

Liau W.B., Boyd R. *Macromolecules* **1990**, *23*, 1531

López-Carrasquero F., Montserrat A., Martínez de Ilarduya A., Muñoz-Guerra S. *Macromolecules* **1995**, *28*, 5535

López-Carrasquero F., García-Álvarez, M., Navas, J.J., Alemán C., Muñoz-Guerra S. *Macromolecules* **1996**, *29*, 8449

Luque F.J., Negre M.J., Orozco M. *J. Phys. Chem.* **1993**, *97*, 4386

Luque F.J., Zhang Y., Alemán C., Gao J, Orozco M. *J. Phys. Chem.* **1996**, *10*, 4269 **(a)**
Luque F.J., Alemán C., Bachs M., Orozco M. *J. Comput. Chem.* **1996**, *17*, 806 **(b)**

Mao F., Tsao Y., Tirrell M., Davis T.H., Hessel V., Ringsdorf H. *Langmuir* **1993**, *9*, 3461

Marlborough D.L. *Biopolymers* **1973**, *12*, 1083

Meille S.V., Ferro D.R., Brückner, Andrew J.L., Padden F.P. *Macromolecules* **1994**, *27*, 2615.

Melis J. *Tesis Doctoral* **1999**, Universitat Politècnica de Catalunya.

Metropolis N., Rosenbluth A.W., Rosenbluth M.N., Teller A.H., Teller E. *J. Chem. Phys.* **1953**, *21*, 1087

Michaels A.S., Bixler H.J. *J. Polym. Sci.* **1961**, 50, 393

Møller C., Plesset M. *S. Phys. Rev.* **1934**, *46*, 618

Morillo M., Martínez de Ilarduya A., Muñoz-Guerra S., *en preparación* **2001**

Müller-Plathe F. *J. Chem. Phys.* **1991**, *94*, 3192

Müller-Plathe F., Rogers S.C., van Gunsteren W.F *Macromolecules* **1992**, *25*, 6722

Muñoz-Guerra S., García-Álvarez M. Pérez-Camero "*Complejos estequiométricos del ácido poli(γ-glutámico) y tensioactivos catiónicos*", patente de invención (**2000**).

Navas J.J., Alemán C., López-Carrasquero F., Muñoz-Guerra S. *Macromolecules* **1995**, *28*, 4487

Navas J.J., Alemán C., Muñoz-Guerra S. *Polymer* **1996**, *37*, 2589

Navas J.J., Alemán C., López-Carrasquero F., Muñoz-Guerra S. *Polymer* **1997**, *38*, 3477

Olander D.S., Holtzer A. *J. Am. Chem. Soc.* **1968**, *90*, 4549

Orozco M., Luque F.J. *J. Comput. Chem.* **1993**, *5*, 587

Orozco M., Luque F.J. *J. Chem. Phys.* **1994**, *182*, 237

Pérez-Camero G., Congregado F., Bou J.J., Muñoz-Guerra S. *Biothecnol. Bioeng.* **1999**, *63*, 110 **(a)** Pérez-Camero G., Martínez de Ilarduya A., García-Álvarez M., Muñoz-Guerra S. *Polym. Pre. ACS* **1999**, *nn*, 1142 **(b)**

Pérez-Camero G. *Comunicación Oral* **2000**.

Pierotti R.A. *Chem. Rev.* **1976**, *76*, 717

Platé N.A., Shibaev V.P. *Comb-like Polymers and Liquid Crystals, Chap. 1*, Plenum Press, New York **(1987)**

Ponomarenko E.A., Waddon A.J., Tirrell D.A., MacKinght W.J. *Langmuir* **1996**, *12*, 2169 **(a)** Ponomarenko E.A., Waddon A.J., Bakeev K.N., Tirrell D.A., MacKinght W.J. *Macromolecules* **1996**, *29*, 4343 **(b)** Ponomarenko E.A., Tirrell D.A., MacKinght W.J. *Macromolecules* **1996**, *29*, 8751 **(c)**

Powell M.J.D. *Comp. J.* **1965**, *7*, 308

Puiggalí J., Muñoz-Guerra S., Rodríguez-Galán A., Alegre C., Subirana, J.A. *Makromol. Chem., Macromol. Symp.* **1988**, *20/21*, 167.

Puleo A.C., Paul D.R., Wong P.K. *Polymer* **1989**, *30*, 1357.

Royappa A.T., Rubner M.F. *ACS Symp. Ser.* **1992**, *493*, 76

Ryckart J.P., Ciccotti G., Berendsen H.J. *J. Comput. Phys.* **1977**, *23*, 327

Rydon, H.N. *J. Chem. Soc.* **1964**, 1328

Sáiz E., Riande, E. *Revista de Plásticos Modernos* **1998**, *75*, 153

Sasaki S, Nakamura T., Miyamoto M., Uematsu I. *Biopolymers* **1978**, *17*, 2715

Sasaki S, Nakamura T., Uematsu I. *J. Polym. Sci., Polym. Phys. Ed.* **1979**, *17*, 825

Sasaki S., Iwanami Y. *Makromol. Chem.* **1986**, *187*, 1263

Siepmann J.I. *Mol. Phys.* **1990**, *70*, 1145

Siepmann J.I., McDonnald I.R. *Mol. Phys.* **1992**, *72*, 2395

Siepmann J.I., Frenkel D. *Mol. Phys.* **1992**, *75*, 59.

Siepmann J.I., Karaborni S., Smit B. *Nature (London)* **1993**, *365*, 330

Slater J.C. "*Quantum theroy of molecules and solids. Volum 4. The self consistent field for molecules and solids*" **1974**, MacGraw-Hill: New York.

Sok R.M., Berendsen H.J.C., van Gunsteren W.F. *J. Chem, Phys.* **1992**, *96*, 4699

Sonnenburg J., Gao J., Weiner JH *Macromolecules* **1990**, *23*, 4653

Sorensen R.L., Liau W.B., Kesner L., Boyd R.H. *Macromolecules* **1988**, *21*, 200

Sumpter B.G., Noid D.W., Wunderlich B. *Macromolecules* **1990**, *23*, 4671

Stupp S.I., Son S., Lin H.C., Li L.S. *Science* **1993**, *259*, 59

Szabo A., Ostlund, N.S "*Modern Quantum Chemistry: Introduction to Advanced Electronic Structure and Theory*" **1982** Macmillan Publishing Co., New York.

Tashiro K., Kobayashi M., Tadokoro H. *Macromolecules* **1978**, *11*, 908

Troy FA. "*Chemistry and biosynthesis of the poly(γ-D-glyamyl) capsule in Bacillus licheniformis*" **1982** Kleinkauf H. , von Döhren H. editors, New York.

Twisleton J.F., White J.W., Reynolds P.A. *Polymer* **1982**, *23*, 578

Ujiie S., Iimura K. *Macromolecules*, **1992**, *25*, 3174

Valleau J.P., Whittington S.G. "*Statistical mechanics and equilibrium techniques*" **1977** Berne BJ (ed.) Plenum Press, New York

Van Krevelen D W. "*Properties of Polymers*", **1990** Elsevier. Amsterdam

Veith W.R., Tam P.M., Michael A.S. J. *Colloid Interface Sci.* **1966**, *22*, 360

Vergelati C., Imberty S., Pérez S. *Macromolecules* **1993**, *26*, 4420

Wang H., Stubbs G. *Acta Cryst.* **1993**, *A49*, 504

Watanabe J., Sasaki S., Uematsu I. *Polym. J. (Tokyo)* **1977**, *9*, 451

Watanabe J., Ono H., Uematsu I., Abe A. *Macromolecules* **1985**, *18*, 2141

Weiner S.J., Kollman P.A, Case D.A., Singh U.C., Ghio C., Alagona G., Profeta S., Weiner P. *J. Am. Chem. Soc.* **1984**, *106*, 765

Weiner S.J., Kollman P.A., Nguyen D.T., Case D.A. *J. Comput. Chem.* **1986**, *7*, 230

Widmann A.H., Laso M., Suter U.W. *J. Chem. Phys.* **1995**, *102*, 5761

Widom, B. *J. Chem. Phys.* **1963**, *39*, 2808

Widom, B. *J. Chem. Phys.* **1982**, *86*, 869

Whitesides G., Mathias J., Seto C. *Science* **1991**, *254*, 1312

Zoller P. *J. Appl. Polym. Sci.* **1977**, *21*, 3129